

Coulomb excitation of ^{12}C as a test of nuclear structure theory

Juan Saiz Lomas

Doctor of Philosophy

University of York

Physics

March 2021

Abstract

This thesis presents the measurement of the quadrupole moment of the 2_1^+ in ^{12}C as a way of benchmarking state-of-the-art nuclear structure theories. Electromagnetic diagonal matrix elements are sensitive to the details of the nuclear interaction and can constrain NN+3N Hamiltonians derived from chiral Effective Field Theories (EFT) used in *ab initio* calculations. The large experimental uncertainty of the quadrupole moment of the 2_1^+ state of ^{12}C when compared to the most recent large-scale No Core Shell Model calculations encouraged the remeasurement of this electromagnetic property.

A Coulomb-excitation experiment was performed at the JYFL facility in Jyväskylä using a ^{12}C ion beam and a ^{208}Pb target. The JURROGAMII array was used to measure the 2_1^+ state de-exciting γ -rays in coincidence with backward-scattered ^{12}C ions, measured with a CD Si detector. From the Coulomb-excitation cross-section, the $Q(2_1^+)$ was extracted by using the least-squares search code GOSIA. The analysis using a nuclear polarizability constant of $k=1.435(27)$ yielded a final value of the $Q(2_1^+) = 8.4_{-3.9}^{+3.6} \text{ efm}^2$ for the currently evaluated value of the $B(E2) = 39.7(2.0) \text{ e}^2\text{fm}^4$. Using a more recent measurement of the $B(E2) = 38.15(0.95) \text{ e}^2\text{fm}^4$, the extracted quadrupole moment was $Q(2_1^+) = 9.3_{-3.8}^{+3.5} \text{ efm}^2$.

The measured value of $Q(2_1^+)$ is in excellent agreement with previous experimental data. The weighted average of the presented experimental result with the literature value yielded $Q(2_1^+) = 8.1(2.3) \text{ efm}^2$ and $Q(2_1^+) = 9.5(1.8) \text{ efm}^2$ when using $B(E2) = 39.7(2.0) \text{ e}^2\text{fm}^4$ or $B(E2) = 38.15(0.95) \text{ e}^2\text{fm}^4$, respectively. The results are compared with the predictions of modern *ab initio* calculations.

Acknowledgements

First of all, I would like to thank my supervisor Dr. Marina Petri for giving me the opportunity to work on such an interesting project. I thank her for the long discussions, and for her guidance and supervision during my PhD.

I would also like to express my gratitude to all of my collaborators for their assistance and help at all of the different stages in my research project. I-Yang, Kasia, Mitch, Janne, Ryo, thank you very much for everything.

A big thanks are reserved for Dr. Liam Gaffney. Thank you for the reading and comments in this thesis, and for the countless hours you spent helping me with my analysis.

A special thanks is reserved for my colleagues and friends in York. Particularly, I would like to thank James for the physics discussions and the countless drinks he has handed over to me throughout the last years.

I thank Prof. José Manuel Quesada, Dr. Carlos Guerrero and my former colleagues at the University of Seville for introducing me to Nuclear Physics and the helpful discussions on optical potentials.

My appreciation also goes to Ina and Sebastian for all of their help and guidance, especially during the very first weeks of my PhD.

Finally, I would like to give my huge appreciation to Lizzie for her unconditional support and for visiting me wherever I was around the world. The biggest thanks also go to my mum and dad, and to Jesús, for their unwavering confidence and support throughout all these years. I would also like to thank Ann and Steve for proofreading this manuscript.

I declare that this thesis is a presentation of original work and I am the sole author. This work has not previously been presented for an award at this, or any other, University. All sources are acknowledged as References.

Contents

List of Figures	xv
List of Tables	xviii
1 Introduction	1
1.1 The nuclear many-body problem	1
1.2 Chiral Effective Field Theory	5
1.3 <i>Ab initio</i>	7
1.3.1 The No-Core Shell Model	8
1.3.2 The Similarity Renormalization Group	10
1.4 Electromagnetic properties in nuclei	12
1.4.1 Nuclear shapes: quadrupole deformation	14
1.5 Electromagnetic properties of ^{12}C	15
1.5.1 Theoretical calculations of quadrupole observables	16
1.5.2 NCSM calculations: the $B(E2)$ and $Q(2_1^+)$ correlation	16
1.5.3 Previous measurements of the $Q(2_1^+)$	20
2 Coulomb excitation	23
2.1 Introduction	23
2.2 The Semi-Classical Approximation	24
2.2.1 First-order Perturbation theory	26
2.2.2 Higher-order perturbation theory	30

2.2.3	Second-order perturbation theory	31
2.2.4	The Reorientation effect	33
2.2.5	The GDR effect	34
2.3	GOSIA	39
2.3.1	Introduction	40
2.3.2	The minimisation process	40
2.3.3	Systematic uncertainties and limitations	43
3	Experimental set-up	45
3.1	The experiment: beam and targets	45
3.2	JUROGAMII	47
3.2.1	Add-back	50
3.2.2	Energy and efficiency calibrations: the ^{66}Ga source	53
3.2.3	Neutron damage	57
3.3	SiCD	59
3.3.1	Energy calibration	60
3.4	Data Acquisition	62
4	Data Analysis and Results	65
4.1	Sorting of the raw data	65
4.1.1	Doppler correction	66
4.1.2	Time gate	69
4.1.3	Particle-energy gates	72
4.2	Gamma-ray spectra	78
4.3	Nuclear interference	86
4.3.1	Minimum distance between nuclear surfaces	86
4.3.2	DWBA calculations	91
4.4	GOSIA analysis	98
4.4.1	GOSIA2 input	98

4.4.2	Nuclear polarizability	100
4.4.3	Fitting procedure	102
4.4.4	χ^2 map	103
4.4.5	Other systematic uncertainties	107
4.5	Results	111
5	Discussion and Conclusions	115
5.1	Revision of previous experimental results	115
5.2	Comparison with previous experiments	120
5.3	Comparison with theory	123
5.4	Conclusion	127
5.5	Future work	129
	Bibliography	130

List of Figures

1.1	Single-particle energies for a Woods-Saxon potential (left) and a Woods-Saxon with spin-orbit coupling potential (right) [Cas90].	3
1.2	Hierarchy of nuclear forces in chiral EFT based on power counting. Solid and dashed lines denote nucleons and pions, respectively. Solid dots, filled circles and filled squares refer, respectively, to the leading, subleading and sub-subleading vertices in the effective Lagrangian. The crossed square denotes 2N contact interactions with 4 derivatives. Figure from [KN11].	6
1.3	Representation of the different types of quadrupole deformation for the different signs and values of the intrinsic $Q_{s,0}$ and spectroscopic $Q(I)$ quadrupole moments.	15

1.4 IT-NCSM calculations showing the correlation of the reduced quadrupole transition strength $B(E2; 0_1^+ \rightarrow 2_1^+)$ with the quadrupole moment $Q(2_1^+)$ obtained with different chiral NN (open symbols) and NN+3N interactions (solid symbols): EM (box), N^2LO_{opt} (circle), and EGM with cutoffs $(\Lambda_\chi/\tilde{\Lambda}_\chi) = \{(450/500), (600/500), (550/600), (450/700), (600/700)\}$ MeV/c (diamond, triangle up, triangle down, hexagon, cross). The calculations are performed at $\hbar\Omega = 16$ MeV and $\alpha = 0.08$ fm⁴ using a model space of $N_{max} = 2$ (blue), 4 (green), 6 (violet), and 8 (red symbols). The error bars indicating the uncertainties of the threshold extrapolations are not included in the plot. The dashed curve is fitted to theoretical data points. The figure has been adapted from Ref. [Cal16], where all details of the calculations can be found. The shaded area in the figure corresponds to the currently adopted value of the $B(E2; 0_1^+ \rightarrow 2_1^+) = 39.7(2.0) e^2\text{fm}^4$ and the predicted value of the $Q(2_1^+)$ by the correlation. 18

1.5 IM-NCSM calculation showing the correlation of the reduced quadrupole transition strength $B(E2; 0_1^+ \rightarrow 2_1^+)$ with the quadrupole moment $Q(2_1^+)$ obtained with N^2LO (open symbols) and N^3LO (full symbols) interactions for three different cutoffs 450 MeV/c (green), 500 MeV/c (blue) and 550 MeV/c (purple). The calculations are performed with $N_{max}^{ref} = 4$ and the error bars indicate the combined many-body and interaction uncertainties. The dotted curve is the correlation curve fitted to theoretical data points. The figure has been adapted from Ref. [D'A20], where all details of the calculations can be found. The hatched area in the figure corresponds to the new experimental value of the $B(E2; 0_1^+ \rightarrow 2_1^+) = 38.15(95) e^2\text{fm}^4$ presented in the same publication, which predicts a value of $Q(2_1^+) = 5.97(30) e\text{fm}^2$ using the dotted correlation line. 19

1.6	Different theoretical and experimental values for the $Q(2_1^+)$ in ^{12}C . From the left to the right: IM-NCSM and IT-NCSM using chiral NN+3N interactions [D'A20, Cal16], Nuclear Lattice EFT at LO [Epe12], Global EDFs [Mac19], adopted value (experimental) [Ver83] and recent measurement result [Raj18].	21
2.1	Schematic representation of the inelastic-scattering process (Coulomb excitation) of two colliding nuclei in the centre of mass frame.	25
2.2	Schematic representation of the first-order contribution to the Coulomb excitation process or single-step excitation.	30
2.3	Schematic representation of the interaction strength (or excitation probability) terms of order χ^2 and χ^3 . The blue arrows represent the single-step first-order excitation interfering with the second-order multi-step terms in red, which include different modes of multi-step excitations and reorientation effects.	32
2.4	Schematic representation of the 2_1^+ excitation process of an even-even nucleus through: multi-step excitation (left), single-step and reorientation (middle) and through the GDR resonance (right).	33
2.5	Coulomb excitation differential cross section for the excitation of the 2_1^+ in ^{12}C for different values of the $Q(2_1^+)$. The calculations were performed with GOSIA [Czo83].	35
2.6	GOSIA dataflow scheme	41
3.1	Sketch of the experimental set-up outside (left) and inside (right) the vacuum chamber. On the left side, the (1) $^{12}\text{C}^{4+}$ beam, (2) SiCD (S2-type) detector, (3) target, (4) scattering chamber, a (5) Clover detector and a (6) Phase1 detector are indicated.	46

3.2	Photos of the experimental set-up taken during the experiment: outside view of the vacuum chamber and half of the JUROGAMII HPGe detectors (left) and view of the interior of the vacuum chamber (right).	47
3.3	3D representation of the JUROGAMII array (left) and transverse view of the inside (right) [Sic13].	48
3.4	Technical and schematic drawing of a Phase1 Eurogam detector module [No194, Pak05].	50
3.5	Sketch of the four crystals inside a Clover detector in the JUROGAMII array. As an example, the events were there is one (a), two (b) or three (c) hits of the incident γ ray is shown.	51
3.6	Energy calibrated ^{66}Ga γ -ray spectrum obtained with the JUROGAMII Clovers with and without the add-back mode. As an example, a zoomed-in photopeak of ^{66}Ga source is displayed.	52
3.7	Add-back factor measured for the different γ -ray transitions in the ^{152}Eu and ^{66}Ga source measurements.	52
3.8	Total γ -ray energy spectra of the produced ^{66}Ga calibration source measured with the whole JUROGAMII array using add-back.	55
3.9	Experimental total efficiencies for each of the used γ -ray transitions in the EuBa and ^{66}Ga source, and curve fit (equation 3.4) for the whole JUROGAMII array (Phase1 and Clover detectors using add-back) relative to the 1039 keV transition in ^{66}Ga .	57
3.10	Comparison of low-energy tail arising from neutron damage observed for the 2751 keV γ -ray transition in ^{66}Ga for different Phase1 detectors.	58
3.11	3D design of the SiCD (S2 type) detector manufactured by Micron Semiconductor Ltd.	59

3.12	Second-order polynomial fit performed for the calibration of sector 3 in the SiCD detector. The calibration points from the triple alpha source as well as the ^{12}C elastic-scattering energies are indicated. Plot changed	60
3.13	Calibrated particle energy spectra of the detected ^{12}C measured by one ring (ring 20), when a second hit has taken place in a certain sector (sector 5), and one sector (sector 5), when a first hit took place at a certain ring (ring 20).	61
3.14	Schematic diagram of the DAQ system and electronics (TDR technique), adapted from [Laz01].	63
4.1	Scheme of the inelastic-scattering process where the angle between the emitted γ ray and each nuclei can be expressed as a function of the JUROGAMII and the S2 SiCD detector angles, see Eq. (4.2.) . . .	67
4.2	Results of the inelastic-scattering calculation of the recoil velocity (β) of the projectile after the decay. The results for before and after passing through the target are shown together with their relative change.	68
4.3	Total γ -ray energy measured with JUROGAMII Doppler-corrected and non-Doppler-corrected for the ^{208}Pb (3_1^-) target excitation.	69
4.4	Time difference, ΔT , between the coincident JUROGAMII γ -ray time and the time stamp, $\Delta T = t_{\text{Juro}} - t_{\text{s}}$, vs. the JUROGAMII energy.	70
4.5	Prompt and background time gates for the data sorting, where $\Delta T = t_{\text{Juro}} - t_{\text{s}}$	71
4.6	Measured JUROGAMII γ -ray Doppler-corrected energy spectrum with a prompt and background (scaled) time gate.	71
4.7	SiCD rings particle-energy spectra with and without a γ -ray energy gate around the 2614 keV 3_1^- ^{208}Pb photopeak.	73

4.8	JUROGAMII γ -ray energy Doppler-corrected for ^{208}Pb vs the SiCD total ring energy spectrum. The auxiliary γ -ray-energy gate used to produce Figure 4.9 is shown with horizontal dashed lines and the final particle-energy gate for the 3_1^- transition in ^{208}Pb is shown with vertical lines.	74
4.9	SiCD total rings particle-energy spectrum gated at the 3_1^- 2614 keV γ -ray-energy transition in ^{208}Pb	75
4.10	JUROGAMII γ -ray energy Doppler-corrected for ^{208}Pb vs the SiCD total ring energy spectrum. The auxiliary γ -ray-energy gate used to produce Figure 4.11 is shown with horizontal dashed lines and the final particle-energy gate for the 2_1^+ transition in ^{208}Pb is shown with vertical lines.	75
4.11	SiCD total rings particle-energy spectrum gated at the 2_1^+ 4085 keV γ -ray-energy transition in ^{208}Pb	76
4.12	JUROGAMII γ -ray energy Doppler-corrected for ^{12}C vs the SiCD total ring energy spectrum. The final particle-energy gate for the 2_1^+ transition in ^{208}Pb is shown with vertical lines.	76
4.13	Particle-energy-gated prompt γ -ray spectra Doppler corrected for the 2_1^+ in ^{12}C measured with R1, R2, R3 and R4 of the JUROGAMII array. The shaded region shows where the $2_1^+ \rightarrow 0^+$ γ ray in ^{12}C is situated.	78
4.14	a) Sketch of the prompt γ -ray spectra (solid black line) with highlighted normalisation regions N1 and N2, net background under peak (netBUP) and the number of estimated counts in the photopeak or γ -ray yield ($Y_\gamma = C_{\text{PK}}$). The position where the normalised background would sit is also indicated (dashed dark red line). (b) Sketch of the background γ -ray spectra (solid dark red line) with highlighted normalisation regions N1, N2, and PK. See the text for more details.	80

4.15	Background subtracted and Doppler-corrected γ -ray energy spectra with inelastic particle-energy gates for the 3_1^- (up) and 2_1^+ (down) excitations in ^{208}Pb . The inset in the upper plot shows the results of the fit of the photopeak to a Gaussian with two exponential tails. The inset in the lower plot shows an example of the peak (blue) and normalisation regions (red) at the left and right hand side of the peak are displayed for the 2_1^+ in ^{208}Pb	83
4.16	Background subtracted and Doppler-corrected γ -ray energy spectra with inelastic particle-energy gates for 2_1^+ excitation in ^{12}C . An example of the peak (blue) and normalisation regions (red) at the left and right hand side of the peak are displayed.	85
4.17	Experimental values of the minimum distance between nuclear surfaces s (fm) vs. the sum of the radii of the interacting nuclei, $C_1 + C_2$ (fm), necessary to ensure a pure electromagnetic interaction and therefore a “safe” Coulomb excitation experiment, for different projectile and target combinations [Wol92].	88
4.18	Minimum distance between nuclear surfaces as a function of the center-of-mass scattering angle using $1.25 \cdot (A_1^{1/3} + A_2^{1/3})$ (red line) and equations 4.16 and 4.15 (green line) as the sum of the nuclear radii respectively. The center-of-mass angles covered in the present experiment are shown as dotted black lines.	89
4.19	Hyperbolic elastic-scattering trajectory of ^{12}C into ^{208}Pb computed in the target frame of reference. The projectile and target nuclei are represented as circumferences of radii equal to C_i placed at distance of closest approach for a scattering angle of $\theta_{\text{CM}} = 160^\circ$ for ^{12}C , and in the origin for ^{208}Pb . The nuclear interaction limit of $s = 6.7(8)$ fm shown as a circumference of radius $C_2 + 6.7(8)$ fm.	90

4.20	Coulomb excitation differential cross section of the 2_1^+ in ^{12}C with (dashed line) and without (solid line) Coulomb-nuclear interference computed with the DWBA code PTOLEMY and the optical-potential parameters from [Rob93]. The angles in the center-of-mass covered by the SiCD detector in the present experiment are indicated by the red shaded area and the obtained interference factor for those angles are displayed in the top left both as a factor and equivalently as a percentage.	94
4.21	Coulomb excitation cross section of the 3_1^- (top) and 2_1^+ (bottom) in ^{208}Pb with (dashed line) and without (solid line) Coulomb-nuclear interference computed with the DWBA code PTOLEMY and the optical-potential parameters from [Rob93]. The angles in the center-of-mass covered by the SiCD detector in the present experiment are indicated by the red shaded area and the obtained interference factor for those angles are displayed in the top left both as a factor and equivalently as a percentage.	95
4.22	Ratio between the Coulomb excitation plus nuclear interference ($d\sigma_{\text{CN}}/d\theta$) and the pure Coulomb excitation ($d\sigma_{\text{C}}/d\theta$) differential cross sections $d\sigma_{\text{CN}}/d\sigma_{\text{C}}$. The calculations were performed with PTOLEMY using a beam energy of 47.486 MeV (center of the target) and the parameters from [Rob93] (top) and the fit to the elastic-scattering cross section at 59 MeV from [San01] (bottom).	97
4.23	Level schemes of ^{12}C and ^{208}Pb as implemented in GOSIA2. The solid lines denote experimentally observed transitions, whilst the dashed lines are “virtual” or unobserved.	99

4.24	Two-dimensional total χ^2 surface obtained with GOSIA2 with respect to the diagonal $\langle 2_1^+ E2 2_1^+ \rangle$ and transitional $\langle 2_1^+ E2 0_1^+ \rangle$ matrix elements in ^{12}C (top) and its 1σ contour (bottom). The solid and dashed lines correspond to the 1σ contours of the Coulomb excitation and lifetime data [Pri16], respectively.	104
4.25	Two-dimensional total χ^2 surface obtained with GOSIA2 with respect to the diagonal $\langle 2_1^+ E2 2_1^+ \rangle$ and transitional $\langle 2_1^+ E2 0_1^+ \rangle$ matrix elements in ^{12}C (top) and its 1σ contour (bottom). The solid and dashed lines correspond to the 1σ contours of the Coulomb excitation and lifetime data [D'A20], respectively.	106
4.26	Relative γ -ray angular distribution of the 3_1^- state in ^{208}Pb normalised to the yield of the JUROGAMII ring 2 ($\theta = 133.57^\circ$) for different values of the g -factor.	109
4.27	Extracted $Q(2_1^+)$ (dark green line) from the GOSIA2 fit to the experimental γ -ray yields from table 4.2 as a function of the nuclear polarizability constant k (total photo-absorption cross section σ_{-2}) using the evaluated value of the $B(E2)$ from [Pri16]. The uncertainties on the final result are represented as the shaded grey area in the figure. The values of the nuclear polarizability constant $k = 1$ and $k = 1.435(27)$ are also indicated.	112
4.28	Extracted $Q(2_1^+)$ (dark green line) from the GOSIA2 fit to the experimental γ -ray yields from table 4.2 as a function of the nuclear polarizability constant k (total photo-absorption cross section σ_{-2}) using the new high precision value of the $B(E2)$ from [D'A20]. The uncertainties on the final result are represented as the shaded grey area in the figure. The values of the nuclear polarizability constant $k = 1$ and $k = 1.435(27)$ are also indicated.	113

5.1	Coulomb excitation curves extracted from [Ver83] for different values of the nuclear polarizability constant k (solid black lines) and interpolated for $k = 1.435, 1.51$ (solid red lines). The dashed black lines represent the statistical uncertainty of 1σ obtained for $k = 1$. The $B(E2)$ value used to extract the final result and its uncertainty are displayed as a solid horizontal pink line and shaded pink area. Finally, the currently adopted and most recent higher-precision $B(E2)$ values, [Pri16] and [D'A20] respectively, are displayed as dashed horizontal lines.	116
5.2	Coulomb excitation curves extracted from [Raj18] for different values of the nuclear polarizability constant k (solid black lines) and interpolated for $k = 1.435$ (solid red line). The dashed black lines represent the statistical uncertainty of 1σ obtained for $k = 1.51$. The currently adopted value of the $B(E2)$ [Pri16] used to extract the final result and its uncertainty are displayed as a solid horizontal blue line and shaded blue area. The most recent higher-precision $B(E2)$ value from [D'A20] is also displayed as a dashed horizontal line.	117
5.3	Comparison of the obtained $Q(2_1^+)$ in ^{12}C in this work together with the previous measurements of [Ver83] and [Raj18] for different values of the $B(E2; 0_1^+ \rightarrow 2_1^+)$ and nuclear polarizability constant k (table 5.1). The dashed and dotted curves represent the IT-NCSM and IM-NCSM correlation lines from Figures 1.4 and 1.5, respectively.	121
5.4	Absolute value of the derivative of the $B(E2)$ with respect to the $Q(2_1^+)$ for the different experiments by [Ver83] and [Raj18], and this work in the range of 5 to 13 efm^2	122

5.5	Weighted average of the $Q(2_1^+)$ measured by [Ver83] with the result extracted from this work for the two different available $B(E2)$ values. The <i>ab initio</i> IT-NCSM and IM-NCSM predictions for both quadrupole observables (Figures 1.4 and 1.5) are also shown.	125
5.6	Different theoretical values (blue squares) for the $Q(2_1^+)$ in ^{12}C . From left to right: IM-NCSM and IT-NCSM using chiral NN+3N interactions [D'A20, Cal16], Nuclear Lattice EFT at LO [Epe12] and Global EDFs [Mac19]. The experimental results of this work averaged with the measurement from [Ver83] are also displayed (red symbols) for the evaluated value of the $B(E2)$ (triangle) and most recent measurement of the $B(E2)$ (circle).	126

List of Tables

3.1	Targets sizes and thicknesses used for the experiment.	47
3.2	JUROGAMII array specifications. (a) T is Phase1 detector and Q is Clover detector. (b) θ is the polar angle, defined with respect to the beam direction. (c) ϕ is the azimuthal angle, defined as vertically upwards and increases in a clockwise direction when the array is viewed from a position upstream. All angles are midpoint angles.	49
3.3	^{66}Ga decay recommended relative γ intensities [Bag02].	54
3.4	Emitted alpha particle energies for the triple α source, ^{239}Pu , ^{241}Am and ^{244}Cm	61
4.1	Particle-energy gates used to produced the “cleaned” final γ -ray spectra.	77
4.2	Final γ -ray yields measured with the JUROGAMII array for the 2_1^+ in ^{12}C and 3_1^- and 2_1^+ in ^{208}Pb	85
4.3	Optical model parameters from [Rob93] and [San01] used to estimate the Coulomb-nuclear interference effect.	93
4.4	Additional spectroscopic data of ^{12}C and ^{208}Pb used in the GOSIA analysis.	100
4.5	Obtained result for the $Q(2_1^+)$ in ^{12}C for the different available $B(E2)$ values, nuclear polarizability constants of $k = 1$ and $k = 1.435(27)$, and with and without Coulomb-nuclear interference. The Coulomb-nuclear interference was estimated using the parameters from [Rob93].	111

5.1	Obtained result for the $Q(2_1^+)$ in ^{12}C using the data from [Ver83] and [Raj18], and the present work for values of the nuclear polarizability constant of $k = 1, 1.435, 1.51$ and $B(E2) = 39.7(2.0), 38.15(95) e^2\text{fm}^4$.	119
-----	---	-----

Chapter 1

Introduction

This chapter will begin with an introduction to the nuclear many-body problem and will put the recently developed NN+3N interactions derived from chiral Effective Field Theory into context. Subsequently, it gives a brief overview of the main *ab initio* approaches of interest for this thesis, and it concludes by highlighting the importance of the measurement of electromagnetic properties in light nuclei with an emphasis on the $Q(2_1^+)$ in ^{12}C .

1.1 The nuclear many-body problem

The atomic nucleus is a quantum many-body system consisting of two types of fermions, protons and neutrons, collectively known as nucleons, which are bound by the strong nuclear force. To understand the structure and dynamics of this system has been the main goal of Nuclear Physics since the discovery of the nucleus by E. Rutherford in 1911. Since then, many different models have been developed throughout the years in order to describe the different observed phenomena at the nuclear scale.

Although many of these models provide a partial description of the nuclear landscape, the microscopic understanding of the strong interaction between the nucleons remains a challenge. The main difficulty lies in the complex nature of the strong nu-

clear force, which emerges from the underlying theory of Quantum Chromodynamics (QCD). At the low energies of relevance to Nuclear Physics, QCD is non-perturbative and very difficult to solve. The relevant degrees of freedom for nuclei are nucleons and pions, which are not fundamental particles but rather complex objects made of quarks, antiquarks and gluons. As a consequence, the strong interaction between nucleons is only an “effective” interaction emerging non-perturbatively from QCD in a similar way to how Van der Waals forces emerge between atoms or molecules [Mac11].

However, despite the intricacy of the nucleon-nucleon (NN) interaction, some much simpler models are able to describe certain features and properties of nuclei. For instance, Weizsäcker’s description of the atomic nucleus as a liquid drop [Wei35] attempted to explain the nuclear binding energies. His semi-empirical mass formula relied on a series of fitted coefficients that accounted for the attractive character of the strong nuclear force, the repulsive nature of the Coulomb interaction between protons, the balance between the number of protons and neutrons in the nucleus (asymmetry term) and the overlap of wavefunctions for pairs of nuclei in various states — also known as pairing.

Another of the first and most successful attempts to describe the structure of the nucleus was accomplished by the widely known shell model, which describes the motion of each nucleon in an average attractive field created by all the other nucleons. Solving Schrödinger’s equation on such a mean field results in a set of orbits or “shells” that, analogously to the ones in the atomic shell model, provide greater stability to the nucleus when filled. In this way, when adding nucleons to a nucleus, there are certain points where the binding energy of the next nucleon is significantly less than the last one.

The experimentally observed number of nucleons corresponding to full shells, known as “magic” numbers, for stable nuclei, were explained within the framework of the shell model by parametrising the assumed nuclear average field as a Woods-

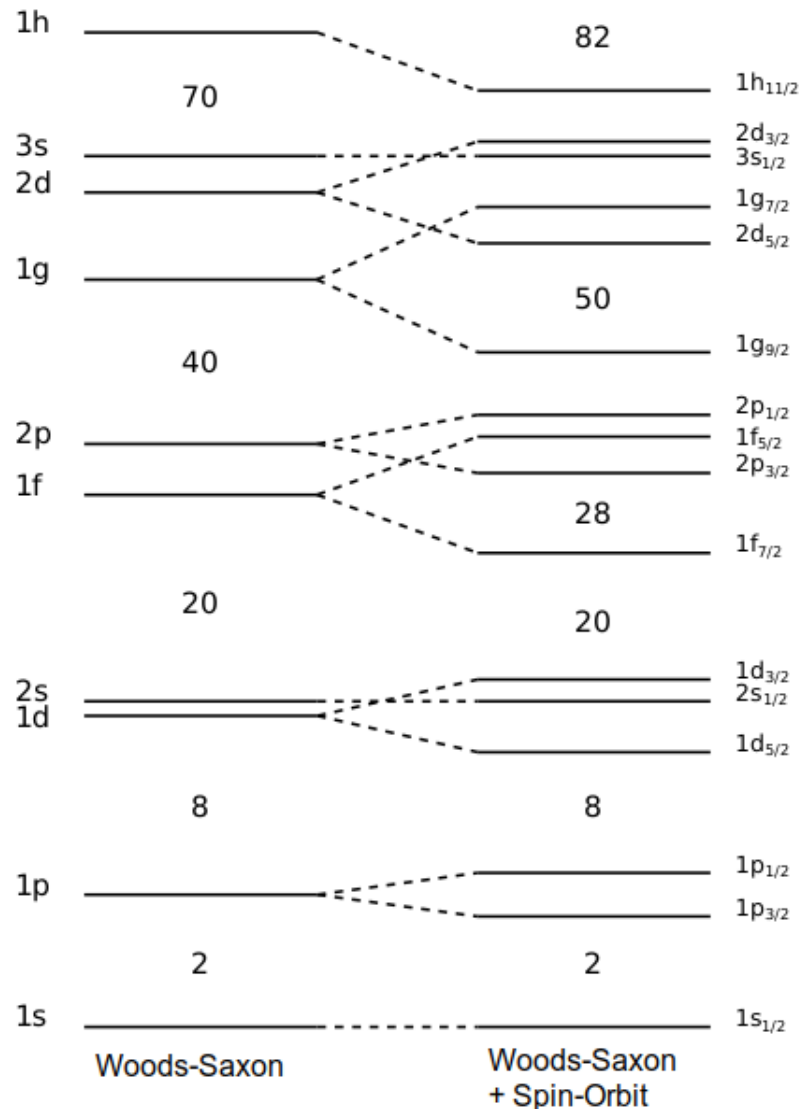


Figure 1.1: Single-particle energies for a Woods-Saxon potential (left) and a Woods-Saxon with spin-orbit coupling potential (right) [Cas90].

Saxon potential [Woo54] with a spin-orbit coupling [May49, Hax49] (Figure 1.1). For their contribution to the development of the shell model, M. G. Mayer and J. H. D. Jensen, shared with E. P. Wigner the 1963 Nobel Prize in Physics. As a result of this success, “shell-model-based” methodology became one of the main approaches to the nuclear many-body problem until now. The most recent shell-model-based models are more refined and extend towards other observables and more exotic nuclei.

As a diametric opposite, another successful model developed during the decade of the 1960s was the macroscopic model proposed by Bohr and Mottelson [Boh69],

which explained the nuclear excitation spectrum from the dynamics of a rotating or vibrating sphere.

More recently, and following a much more complex formalism, self-consistent mean-field methods (SCMF) based on Density Functional Theory (DFT) [Ben03], employ energy-density functionals that are primarily constrained by global nuclear properties, such as binding energies or radii, to compute nuclear structure observables across the nuclear chart, primarily in the heavier regions. Often, these methods would use a phenomenological interaction which in principle remains disconnected to the underlying details of the strong force.

Ab initio methods, on the other hand, seek to describe the atomic nucleus from first principles by solving the non-relativistic Schrödinger equation among all constituent nucleons and the interactions between them. Due to the difficulties that a direct use of QCD would imply, our knowledge on how nuclear observables emerge from the NN interaction is limited to models at present, the most advanced and fundamental of which are based on chiral Effective Field Theory (EFT or ChEFT) [Mac11]. Testing *ab initio* methods using state-of-the-art interactions based on chiral EFT is the goal of the present dissertation and the latter will be discussed in more detail in sections 1.2 and 1.3 .

In general, the efforts of describing the structure of the atomic nucleus have been extensive, and the large variety of modelling initiatives can be grouped fundamentally into shell-model theories, macroscopic models, SCMF and *ab initio* methods. Until now, the different models used different nuclear interactions in their calculations based on phenomenology or experimental data, which had a direct impact in the applicability and accuracy of the different models to the various regions of the nuclear landscape. The recent developments in the *ab initio* many-body methods have allowed the calculations of nuclear observables using state-of-the-art chiral EFT interactions. These interactions can now be tested giving a better insight into the connection of the strong interaction to the underlying QCD, perhaps providing a

more consistent approach to describe the NN interaction when using any many-body solver to compute nuclear properties.

1.2 Chiral Effective Field Theory

In the 1990s an effective field theory (EFT) was introduced and applied to low-energy QCD. In this EFT, at low energy, the effective degrees of freedom are pions and nucleons rather than quarks and gluons, which could resemble previous theories of the NN interaction such as Yukawa's [Yuk55]. However, in the case of these effective theories, it will be the broken chiral symmetry that will become a crucial constraint that generates and controls the dynamics and establishes a clear connection with the underlying theory, QCD.

Chiral EFT starts with the most general Lagrangian consistent with the (broken) symmetries of QCD. The interactions of pions must vanish at zero momentum transfer and in the chiral limit ($m_\pi \rightarrow 0$). The low-energy expansion of the Lagrangian is arranged in powers of derivatives and pion masses. Chiral perturbation theory (ChPT) refers to the expansion of the Lagrangian in terms of powers of ν as $(Q/\Lambda_\chi)^\nu$ and the chiral breakdown scale $\Lambda_\chi \approx 1\text{GeV}$. The effective Lagrangian can then be formally written as

$$\mathcal{L}_{\text{eff}} = \mathcal{L}_{\pi\pi} + \mathcal{L}_{\pi N} + \dots, \quad (1.1)$$

where $\mathcal{L}_{\pi\pi}$ deals with the dynamics among pions, $\mathcal{L}_{\pi N}$ describes the interaction between pions and nucleons, and higher order terms describe interactions involving pions and two or more nucleons. Each of these Lagrangians can be expressed as

$$\mathcal{L}_{\pi\pi} = \mathcal{L}_{\pi\pi}^{(2)} + \mathcal{L}_{\pi\pi}^{(4)} + \dots \quad (1.2)$$

$$\mathcal{L}_{\pi N} = \mathcal{L}_{\pi N}^{(1)} + \mathcal{L}_{\pi N}^{(2)} + \mathcal{L}_{\pi N}^{(3)} + \dots \quad (1.3)$$

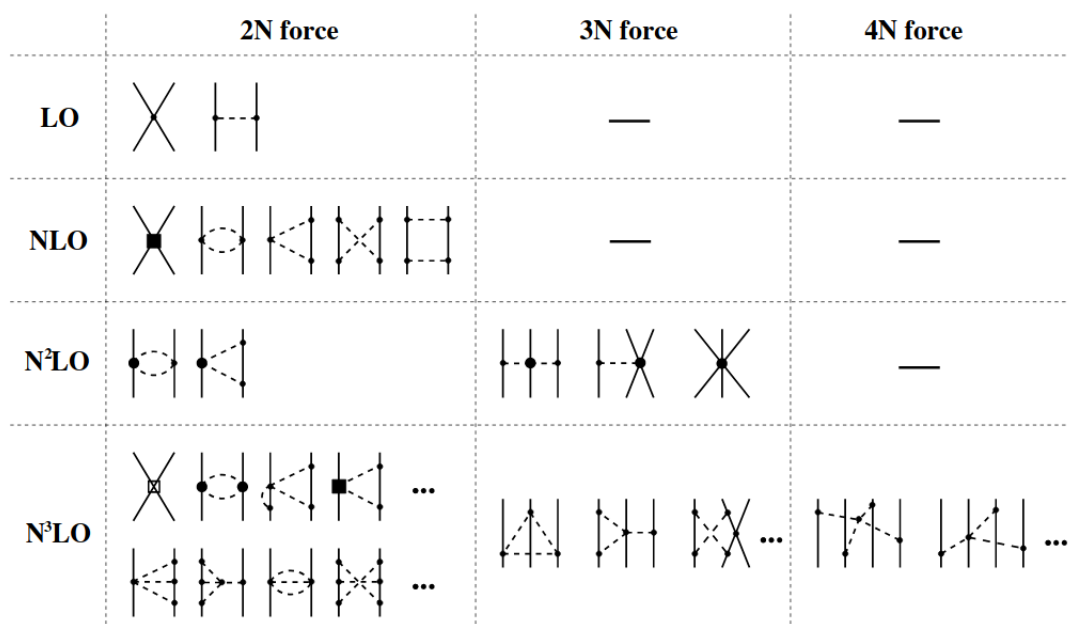


Figure 1.2: Hierarchy of nuclear forces in chiral EFT based on power counting. Solid and dashed lines denote nucleons and pions, respectively. Solid dots, filled circles and filled squares refer, respectively, to the leading, subleading and sub-subleading vertices in the effective Lagrangian. The crossed square denotes 2N contact interactions with 4 derivatives. Figure from [KN11].

where the superscript refers to the number of derivatives or pion-mass insertions (chiral dimension).

Chiral perturbation theory implies that nuclear forces emerge as a hierarchy controlled by the power ν , which gives the finite set of terms that will contribute to the effective Lagrangian and will also provide the relative size of the different contributions. This power counting hierarchy of nuclear forces is displayed in Figure 1.2. At leading order (LO, $\nu = 0$) the two contributions are the nucleon contact term and the one-pion exchange. At next-to-leading order (NLO, $\nu = 1$), the higher order contact term is accompanied by multiple two-pion exchanges. From (N2LO, $\nu = 2$) onwards, sets of 3N forces arise, with 4N forces starting to appear at (N3LO, $\nu = 3$).

1.3 *Ab initio*

Ab initio many-body methods in nuclear physics start from the fundamental forces among nucleons, typically chiral EFT interactions, and attempt to predict properties of nuclei from first principles. The strategy is then to solve the non-relativistic Schrödinger equation with the inter-nucleon interaction as the only input. Despite an exact solution only being achievable for light nuclei ($A = 3, 4$) [Fri93, Nog97, Bar01, Kam01], new *ab initio* methods using well-controlled approximations have made tremendous progress and have been able to compute much heavier nuclei. There are many *ab initio* methods that are able to use chiral EFT interactions, ranging from the No-Core Shell Model (NCSM), Coupled Cluster (CCM), Self-Consistent Green's Function (SCGF), In-Medium Similarity Renormalization Group (IM-SRG) to Monte Carlo methods such as the Green's Function Monte Carlo Method (GFMC), Nuclear Lattice EFT or the Auxiliary-Field Monte Carlo (AFDMC) method. However, the focus of the present thesis will be towards the *ab initio* No-Core Shell Model (NCSM).

The initial problem is then to solve the Schrödinger equation

$$\hat{H} |\Psi\rangle = (\hat{T}_{\text{int}} + \hat{V}) |\Psi\rangle = E |\Psi\rangle \quad (1.4)$$

on the A -body hamiltonian \hat{H} , which is composed of the intrinsic kinetic energy \hat{T}_{int} and the nuclear interaction \hat{V} as

$$\hat{H} = \frac{1}{A} \sum_{i < j = 1}^A \frac{(\hat{p}_i - \hat{p}_j)^2}{2m} + \sum_{i < j = 1}^A \hat{V}_{ij}^{NN} + \sum_{i < j < k = 1}^A \hat{V}_{ijk}^{3N} + \dots, \quad (1.5)$$

where m is the nucleon mass, \vec{p}_i is the momentum of the i th nucleon and the nuclear interaction \hat{V} describes the strong and electromagnetic interaction among nucleons. This interaction has to be treated in a perturbative manner, splitting the potential into different many-body terms $\hat{V}^{NN} + \hat{V}^{3N} + \dots$. The electromagnetic interaction

is typically described by the Coulomb force, while the determination of the strong interaction remains the biggest challenge.

Due to the non-perturbative character of QCD in the low-energy regime of interest for nuclear physics, different phenomenological approaches to describe the NN interaction have taken place. For instance, basic symmetries of the Hamiltonian and Yukawa’s meson-exchange theory [Yuk55] have inspired the development of phenomenological high-precision NN interactions, namely the Argonne V18 [Wir95] and CD-Bonn [Mac01] potentials. These interactions have been able to accurately describe NN systems but have failed to be extended to heavier systems [Cau02, Nav02, Pie02]. This suggests the importance of many-nucleon interactions beyond the two-body level and reveals the necessity for a consistent scheme to construct the nuclear interactions [Nav16].

1.3.1 The No-Core Shell Model

The following section aims to give a brief introduction to *ab initio* No-Core Shell Model (NCSM) calculations. A complete description of the method and formalism can be found in [Bar13].

In the *ab initio* NCSM, a system of A point-like non-relativistic nucleons are all considered to interact with each other by a realistic two- or two- plus three-nucleon interaction as per equation 1.5, which means there is no inert core of the nucleus as in standard shell model calculations. The term “realistic two-nucleon interactions” refers to NN potentials that fit nucleon-nucleon phase shifts with high precision up to a certain energy, typically up to 350 MeV. Realistic 3N interactions include two-pion exchanges with an intermediate Delta excitation [Bar13].

In order to solve equation 1.5, in NCSM, the individual single-particle wave-functions are expanded in the Harmonic Oscillator (HO) basis as

$$|\phi\rangle = |n_1 l_1 m_1\rangle \otimes |s_1 m_s\rangle \otimes |t_1 m_t\rangle, \quad (1.6)$$

where n is the principal quantum number and l, s and t are the angular momentum, spin and isospin with respective projections m_l, m_s and m_t . The A-body wavefunction can then be expressed as

$$|\Psi\rangle = \sum_{\phi_1 < \phi_2 < \dots < \phi_A}^{N_{\text{totmax}}} C_{\phi_1 \phi_2 \dots \phi_A} |\phi_1 \phi_2 \dots \phi_A\rangle, \quad (1.7)$$

where $|\phi_1 \phi_2 \dots \phi_A\rangle$ are Slater determinants defined as

$$|\phi_1 \phi_2 \dots \phi_A\rangle = \frac{1}{\sqrt{A!}} \sum_{\pi} \text{sgn}(\pi) \hat{P}_{\pi} (|\phi_1\rangle \otimes |\phi_2\rangle \otimes \dots \otimes |\phi_A\rangle), \quad (1.8)$$

since the basis needs to be antisymmetric due to the fermionic character of protons and neutrons. Here N_{totmax} denotes the chosen maximum of the sum of all HO excitations, i.e. the model space truncation, which follows the condition

$$N_{\text{totmax}} \geq \sum_{i=1}^A (2n_i + l_i). \quad (1.9)$$

Often, the parameter N_{max} is introduced instead, which measures the maximum allowed HO excitation energy above the unperturbed ground state. The N_{max} truncation is the only possible one that allows an exact factorisation of the c.m. motion for the eigenstates, even when working with single-particle coordinates and Slater determinants [Nav16]. The use of the HO basis allows preservation of translational symmetry of the nuclear self-bound system, even if single-nucleon coordinates are utilised.

The solution to equation 1.5 is finally obtained by diagonalising the respective matrix or using a variational principle. The accuracy of the solution will nevertheless depend on the size of the model space after the truncation, which needs to be very large. In fact, the computational cost of the calculation increases with N_{max} . A way to improve this truncation is through the use of an iterative importance truncation scheme and reducing the dimension of the model space of configuration

by an *a priori* selection of the physically most relevant basis states [Rot09]. The method uses an importance measure derived from multiconfigurational perturbation theory in combination with an importance threshold and it constructs a model space optimised for the description of individual eigenstates of a given Hamiltonian. As a result, NCSM calculations with an importance truncated model space for nuclei such as ^{12}C or ^{16}O can be performed up to a $N_{\text{max}} = 22$ [Rot09]. This approach is also known as Importance Truncated No-Core Shell Model (IT-NCSM).

1.3.2 The Similarity Renormalization Group

However, in general, it is still difficult to converge NCSM-type calculations beyond the lightest nuclei. Also the inclusion of the relevant 3N contributions can be problematic for *ab initio* methods when a bare chiral interaction is used [Cal16]. As a solution, the nuclear interaction can be softened by applying a unitary transformation or similarity renormalisation group [Bog07], which can be applied consistently in the two- and three-body space. This approach is used in several nuclear structure applications and calculations to soften the chiral NN+3N interactions used.

The basic concept of SRG is the continuous unitary transformation of the Hamiltonian

$$\hat{H}_s = \hat{U}_s^\dagger \hat{H} \hat{U}_s, \quad (1.10)$$

defined by the first-order differential operator equation

$$\frac{d}{ds} \hat{U}_s = \left[\hat{\eta}_s, \hat{H}_s \right], \quad (1.11)$$

where \hat{U}_s is a unitary operator depending on the continuous flow-parameter s and \hat{H}_s is the SRG evolved Hamiltonian depending on the flow parameter s and the anti-Hermitian dynamic generator

$$\hat{\eta}_s = -\hat{U}_s^\dagger \frac{d}{ds} \hat{U}_s = -\hat{\eta}_s^\dagger. \quad (1.12)$$

The canonical generator, used in the majority of nuclear structure and reaction applications, is the commutator of the kinetic energy with the Hamiltonian, which reads

$$\hat{\eta}_s = (2\mu)^2 \left[T_{\text{int}}, \hat{H}_s \right], \quad (1.13)$$

where μ is the reduced nucleon mass and T_{int} is the intrinsic kinetic-energy operator. For this generator, the flow parameter s is associated with a momentum scale $\Lambda = s^{-1/4}$. The use of this generator makes the Hamiltonian drive towards a diagonal in the momentum eigenbasis of the kinetic energy operator. This diagonalisation makes the low and high momentum parts of the Hamiltonian become decoupled, allowing a significantly improved convergence.

As shown, the SRG can be used as a tool to “pre-process” the nuclear interactions that are used as inputs for other many-body methods. However, SRG-like flow equations can be used to decouple physics at different excitation energy scales of the nucleus, and render the Hamiltonian matrix in configuration space block or band diagonal. In other words, the many-body expansion can be re-organised in a way in which correlations that are described explicitly by the configuration space are absorbed into an RG-improved Hamiltonian. The extraction of eigenvalues and eigenstates then becomes possible with the appropriate choice of decoupling strategy giving rise to an *ab initio* method known as In Medium Similarity Renormalization Group (IMSRG) [Her16b, Her16a, Tsu11]. An extension of this method, designed for calculations of the ground-state properties of closed- and open-shell nuclei, is the multi-reference IMSRG (MR-IMSRG) [Her16a].

The combination of the multireference IMSRG with the NCSM gives rise to a new *ab initio* method which includes the advantages of the two methods: the decoupling at the many-body level in the IM-SRG and the access to arbitrary nuclei, eigenstates and observables in the NCSM. This new In-Medium NCSM (IM-NCSM) [Geb17] enables fully converged no-core calculations for an unprecedented range of nuclei allowing the study of the full-range of medium-mass nuclei.

1.4 Electromagnetic properties in nuclei

As discussed above, *Ab initio* nuclear structure theories using NN+3N Hamiltonians derived from chiral EFT connect to the underlying physics of the strong interaction and provide a unique opportunity to understand the nuclear structure and its emergence from first principles [Epe09]. Although calculations of excitation energies with chiral NN+3N interactions in light and medium-mass (mainly closed-shell) nuclei have been successful, their extension to other observables such as electromagnetic properties remains a challenge.

Electromagnetic transitional and diagonal matrix elements constitute a sensitive probe to the details of the nuclear interaction and can constrain NN+3N Hamiltonians derived from chiral EFT in *ab initio* calculations. Electric-quadrupole ($E2$) matrix elements are therefore important quantities in probing nuclear structure. For instance, they are very sensitive to nuclear deformation, the decoupling of proton and neutron degrees of freedom, and they are often affected by small components of the nuclear wave functions [For13].

The reduced transition probability associated with the radiative transition of multipole order λ can be expressed as a function of the transitional matrix element of the electromagnetic operator $E\lambda$, as

$$B(E\lambda, I_i \rightarrow I_f) = \frac{1}{2I_i + 1} |\langle I_f | \mathcal{M}(E\lambda) | I_i \rangle|^2. \quad (1.14)$$

The spectroscopic quadrupole moment (Q), i.e. quadrupole moment observed in the laboratory frame, can also be expressed in terms of the diagonal matrix element by calculating the expectation value of the quadrupole operator $(16\pi/5)^{1/2} r^2 Y_{20}$ in the

laboratory system as

$$\begin{aligned}
 Q(I) &= \left(\frac{16\pi}{5}\right)^{\frac{1}{2}} \langle I, M = I | r^2 Y_{20} | I, M = I \rangle = \left(\frac{16\pi}{5}\right)^{\frac{1}{2}} \begin{pmatrix} I & 2 & I \\ -I & 0 & I \end{pmatrix} \langle I || r^2 Y_{20} || I \rangle = \\
 &= \left(\frac{16\pi}{5} \cdot \frac{I(2I-1)}{(I+1)(2I+1)(2I+3)}\right)^{\frac{1}{2}} \langle I || \mathcal{M}(E2) || I \rangle. \quad (1.15)
 \end{aligned}$$

Connected to the spectroscopic quadrupole moment, the intrinsic “static” quadrupole moment $Q_{0,s}$ is the value of Q that would be observed in the reference frame of the nucleus if such measurement were possible. Within the framework of the rotational model by Bohr and Mottelson [Boh69], it can be shown that for an axially symmetric shape, the spectroscopic quadrupole moment $Q(I)$ is connected to the intrinsic quadrupole moment $Q_{0,s}$ via the formula

$$Q(I) = \frac{3K^2 - I(I+1)}{(I+1)(2I+3)} Q_{0,s}, \quad (1.16)$$

where K is the projection of the total angular momentum on the symmetry axis of the intrinsically deformed nucleus.

Similarly, the reduced transition probability of order $\lambda = 2$ is connected to the intrinsic “transitional” quadrupole moment $Q_{0,t}$ by

$$B(E2, I_i \rightarrow I_f) = \frac{5}{16\pi} \begin{pmatrix} I_i & 2 & I_f \\ K & 0 & K \end{pmatrix}^2 Q_{0,t}^2. \quad (1.17)$$

The combination of equations 1.16 and 1.17 gives a correlation between both quadrupole observables, $B(E2)$ and spectroscopic quadrupole moment $Q(I)$, parametrised only by the ratio $Q_{0,t}/Q_{0,s}$, i.e.

$$B(E2, I_i \rightarrow I_f) = \frac{5}{16\pi} \left(\frac{(I+1)(2I+3)}{3K^2 - I(I+1)}\right)^2 \begin{pmatrix} I_i & 2 & I_f \\ K & 0 & K \end{pmatrix}^2 \left(\frac{Q_{0,t}}{Q_{0,s}}\right)^2 Q(I)^2, \quad (1.18)$$

where the intrinsic transitional $Q_{0,t}$ and static $Q_{0,s}$ quadrupole moments are expected to be equal within the rigid rotor model, $Q_{0,t} = Q_{0,s} = Q_0$ [Cal16].

1.4.1 Nuclear shapes: quadrupole deformation

The electric-quadrupole moment can be interpreted as the measurement of the extent to which the nuclear charge distribution deviates from spherical symmetry [Boh69]. When a nucleus deviates from sphericity, its surface can be parametrised by the length of the radius vector pointing from the origin to the surface

$$R = R(\theta, \phi) = R_0 \left(1 + \sum_{\lambda=0}^{\infty} \sum_{\mu=-\lambda}^{\lambda} \alpha_{\lambda\mu}^* Y_{\lambda\mu}(\theta, \phi) \right), \quad (1.19)$$

where R_0 is the radius of the sphere with the same volume, $\alpha_{\lambda\mu}$ are deformation parameters and $Y_{\lambda\mu}(\theta, \phi)$ are the spherical harmonics. The terms corresponding to $\lambda = 0$ in the sum, $\alpha_{0,0}$, describe changes in the nuclear volume while, for small deformations, the terms $\lambda = 1$ describe mainly translations of the whole system, thus the information of the nuclear shape is contained in the terms for $\lambda \geq 2$.

For an axially symmetric deformation, choosing the z-axis as the symmetry axis, all $\alpha_{\lambda\mu}$ vanish except when $\mu = 0$ and equation 1.19 can be rewritten as

$$R(\theta) = R_0 \left(1 + \sum_{\lambda=2}^{\infty} \sqrt{\frac{2\lambda+1}{4\pi}} \beta_{\lambda} P_{\lambda 0}(\cos \theta) \right), \quad (1.20)$$

where the deformation parameters $\alpha_{\lambda 0}$ are defined as β_{λ} .

For the case of quadrupole deformations ($\lambda = 2$), the deformation parameters β_2 are linked to the intrinsic static quadrupole moment, $Q_{0,s}$ in equation 1.16, by

$$Q_{0,s} = \frac{3}{\sqrt{5\pi}} Z R_0^2 \bar{\beta}_2, \quad (1.21)$$

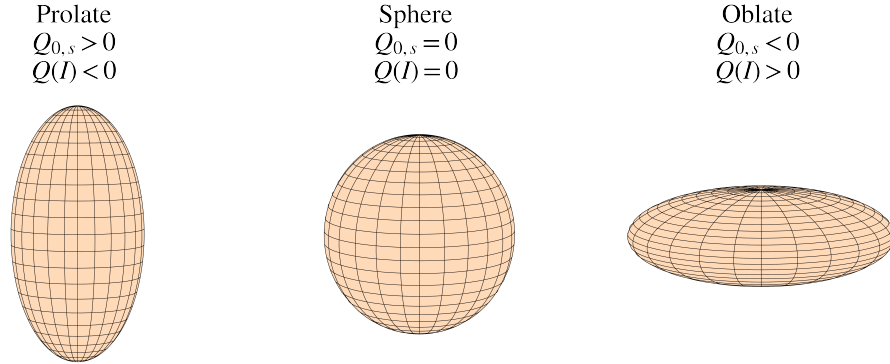


Figure 1.3: Representation of the different types of quadrupole deformation for the different signs and values of the intrinsic $Q_{s,0}$ and spectroscopic $Q(I)$ quadrupole moments.

where $\bar{\beta}_2$ is given by the intrinsic relation [Lea88],

$$\bar{\beta}_2 = \beta_2 + \sqrt{\frac{5}{\pi}} \left(\frac{2}{7}\beta_2^2 + \frac{4}{15}\beta_3^2 + \frac{20}{77}\beta_4^2 + \frac{10}{39}\beta_5^2 + \frac{98}{386}\beta_6 + \frac{12}{7\sqrt{5}}\beta_2\beta_4 + \frac{20}{21}\sqrt{\frac{7}{11}}\beta_3\beta_5 + \frac{30}{11}\frac{1}{\sqrt{13}}\beta_4\beta_6 \right). \quad (1.22)$$

Assuming axial symmetry, the positive values of the intrinsic quadrupole moment $Q_{0,s}$, negative values of the spectroscopic quadrupole moment $Q(I)$ measured in the laboratory, will correspond to prolate deformations, while the negative values of $Q_{0,s}$ and positive values of $Q(I)$ will correspond to oblate shapes. Null values of both intrinsic and spectroscopic quadrupole moments will represent a spherical shape, i.e. without any deformation. A graphical representation of this is displayed in Figure 1.3.

1.5 Electromagnetic properties of ^{12}C

Within the nuclear chart, the Carbon $Z=6$ isotopes are excellent candidates to put nuclear models under stringent tests; these isotopes are experimentally accessible up to the neutron dripline and critical spectroscopic information can be extracted from them.

1.5.1 Theoretical calculations of quadrupole observables

Large-scale NCSM calculations have been performed for low-lying states of even-even Carbon isotopes with $A=10-20$ [For13] using a CDB2k potential [Mac01] to describe the NN interaction. Further IT-NCSM/SRG calculations using two- and three-nucleon interactions from chiral EFT for the quadrupole moment of the first 2_1^+ state in ^{12}C have been performed, showing a drastically improved accuracy [Cal16]. Additionally, the recently developed IM-NCSM with improved convergence using chiral NN+3N interactions have also aimed at calculating electromagnetic observables in ^{12}C [D'A20]. Furthermore, spectroscopic properties of low-lying states and cluster structures in ^{12}C have been analyzed in a beyond mean-field framework based on global energy-density functionals (EDFs) [Mac19]. Testing the latest IT- and IM-NCSM calculations is one of the main goals of this thesis and the latter calculations will be discussed in more detail in section 1.5.2.

The astrophysical implications of ^{12}C and its Hoyle state have attracted significant theoretical attention with several nuclear models trying to reproduce the spectroscopy of this nucleus. Recent examples are NCSM calculations using NN and 3N interactions from chiral EFT [Mar14] and Nuclear Lattice EFT calculations [Epe12].

1.5.2 NCSM calculations: the $B(E2)$ and $Q(2_1^+)$ correlation

Importance-Truncated No-Core Shell Model (IT-NCSM) calculations using a set of different two- and three-nucleon interactions from chiral effective field theory have been performed to compute excitation energies as well as electric-quadrupole ($E2$) and magnetic dipole ($M1$) moments and transition strengths for ^{12}C [Cal16]. Figure 1.4 is an adaptation of FIG. 4 in Ref. [Cal16], illustrating the obtained

reduced quadrupole transition strength $B(E2; 0_1^+ \rightarrow 2_1^+)$ and $Q(2_1^+)$ for the 2_1^+ in ^{12}C using a set of chiral NN and NN+3N interactions (EM [Ent03] and EGM [Epe04]) for different model-space truncations from $N_{\text{max}} = 2$ to 8. The calculations point towards a strong and robust correlation between both $E2$ observables. Individually, both observables show a strong dependence on the underlying interaction and truncation of the model space. The authors in Ref. [Cal16] interpreted this correlation in terms of the rotational model by Bohr and Mottelson [Boh69] by fitting equation 1.18 to the different theoretical calculations and yielding a ratio between the intrinsic quadrupole moments of $Q_{0,t}/Q_{0,s} = 0.964$ (dashed black line). Using this correlation between both quadrupole observables and the adopted value of the $B(E2) = 39.7(2.0) e^2\text{fm}^4$, (shaded area in Figure 1.4), the IT-NCSM calculations predict a value of $Q(2_1^+) = 5.91(15) e\text{fm}^2$.

Similarly, and very recently, state-of-the-art In-Medium NCSM (IM-NCSM) calculations have also targeted the calculation of the reduced quadrupole transition strength $B(E2; 0_1^+ \rightarrow 2_1^+)$ and $Q(2_1^+)$ for the 2_1^+ in ^{12}C [D'A20]. These calculations use a new family of chiral two- plus three-nucleon interaction presented in Ref. [Hut19]. Figure 1.5 shows the results obtained for both observables from FIG. 6. in Ref. [D'A20], where a similar correlation to that shown in Figure 1.4 was observed and the calculations were once more fitted using equation 1.18 and yielded $Q_{0,t}/Q_{0,s} = 0.967$ (dotted line). The hatched area corresponds to the new experimental value of the $B(E2; 0_1^+ \rightarrow 2_1^+) = 38.15(95) e^2\text{fm}^4$ presented in the same publication, which predicts a value of the $Q(2_1^+) = 5.97(30) e\text{fm}^2$ using the IM-NCSM correlation line.

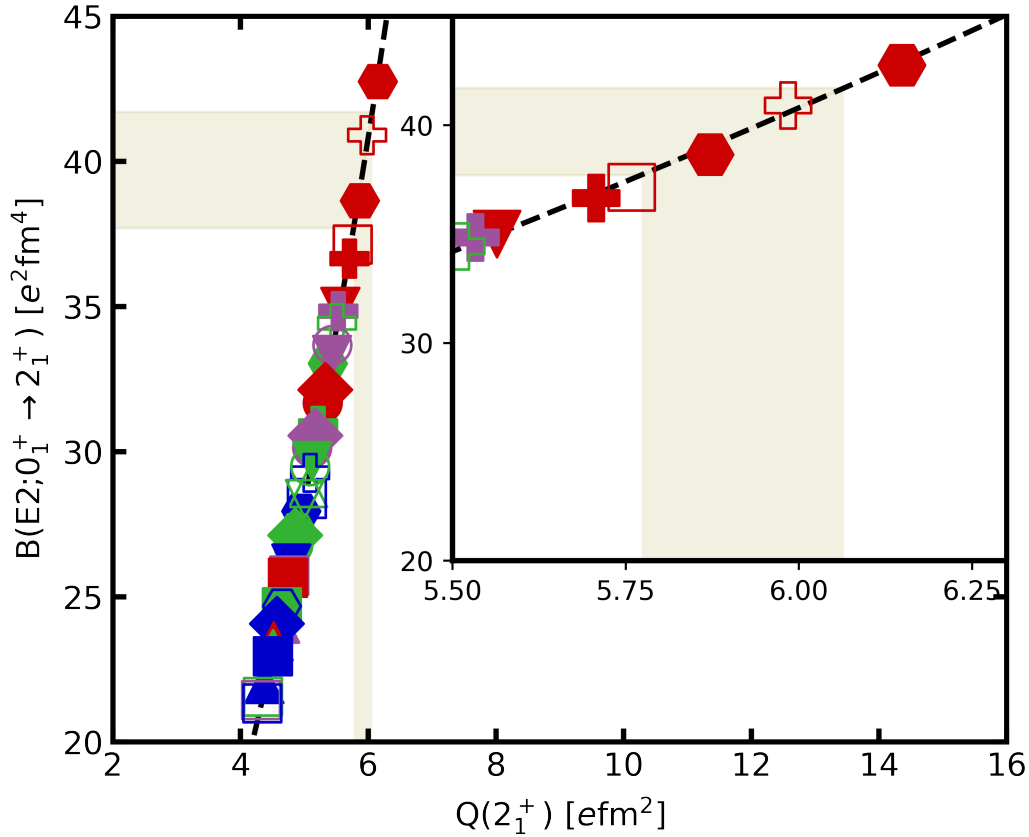


Figure 1.4: IT-NCSM calculations showing the correlation of the reduced quadrupole transition strength $B(E2; 0_1^+ \rightarrow 2_1^+)$ with the quadrupole moment $Q(2_1^+)$ obtained with different chiral NN (open symbols) and NN+3N interactions (solid symbols): EM (box), N^2LO_{opt} (circle), and EGM with cutoffs $(\Lambda_\chi/\tilde{\Lambda}_\chi) = \{(450/500), (600/500), (550/600), (450/700), (600/700)\}$ MeV/c (diamond, triangle up, triangle down, hexagon, cross). The calculations are performed at $\hbar\Omega = 16$ MeV and $\alpha = 0.08$ fm⁴ using a model space of $N_{max} = 2$ (blue), 4 (green), 6 (violet), and 8 (red symbols). The error bars indicating the uncertainties of the threshold extrapolations are not included in the plot. The dashed curve is fitted to theoretical data points. The figure has been adapted from Ref. [Cal16], where all details of the calculations can be found. The shaded area in the figure corresponds to the currently adopted value of the $B(E2; 0_1^+ \rightarrow 2_1^+) = 39.7(2.0)$ e²fm⁴ and the predicted value of the $Q(2_1^+)$ by the correlation.

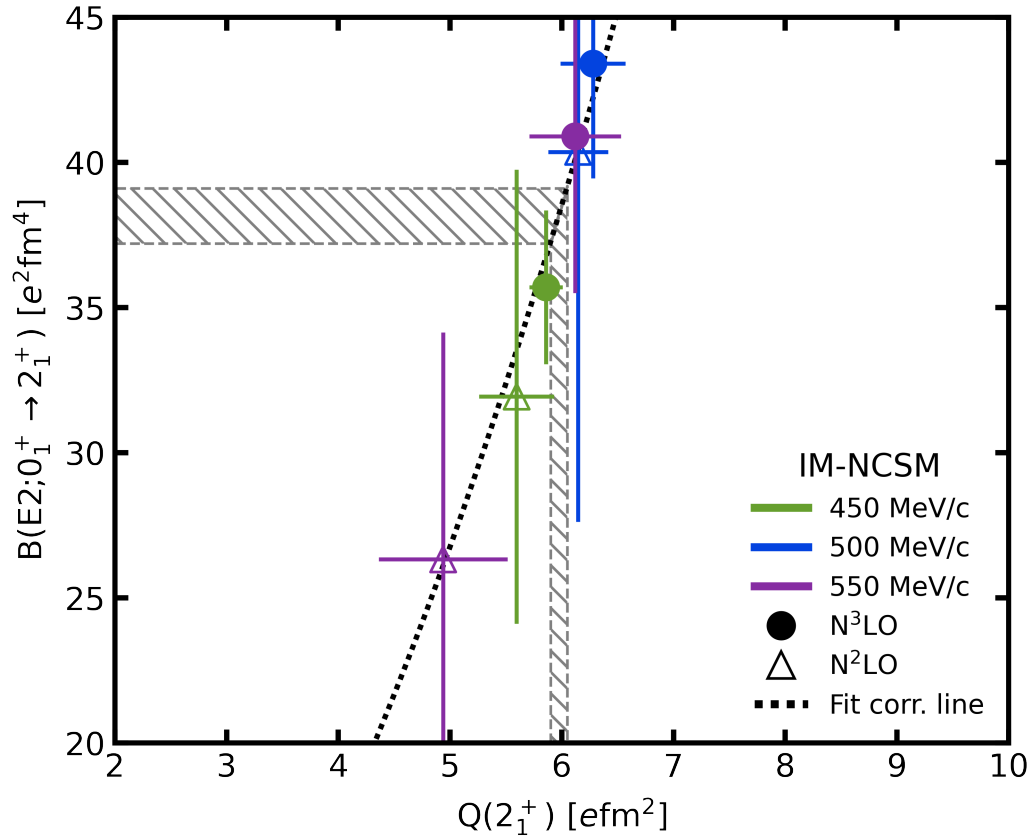


Figure 1.5: IM-NCSM calculation showing the correlation of the reduced quadrupole transition strength $B(E2; 0_1^+ \rightarrow 2_1^+)$ with the quadrupole moment $Q(2_1^+)$ obtained with N^2LO (open symbols) and N^3LO (full symbols) interactions for three different cutoffs 450 MeV/c (green), 500 MeV/c (blue) and 550 MeV/c (purple). The calculations are performed with $N_{\max}^{\text{ref}} = 4$ and the error bars indicate the combined many-body and interaction uncertainties. The dotted curve is the correlation curve fitted to theoretical data points. The figure has been adapted from Ref. [D'A20], where all details of the calculations can be found. The hatched area in the figure corresponds to the new experimental value of the $B(E2; 0_1^+ \rightarrow 2_1^+) = 38.15(95) e^2 fm^4$ presented in the same publication, which predicts a value of $Q(2_1^+) = 5.97(30) efm^2$ using the dotted correlation line.

1.5.3 Previous measurements of the $Q(2_1^+)$

Irrespective of the above, constraining these different theoretical approaches by comparing their results for the $Q(2_1^+)$ in ^{12}C with the available experimental data is very challenging. The difficulties arise from the fact that the experimental uncertainty is much larger than most of the theoretical calculations (see Figure 1.6), the currently adopted value having an uncertainty of $6 \pm 3 \text{ efm}^2$ [Ver83]. In addition, there has been a recent measurement of this property but the uncertainty in the result was estimated to be greater than the only previous experiment $5.3 \pm 4.4 \text{ efm}^2$ [Raj18]. The different theoretical calculations and experimental values available for the $Q(2_1^+)$ in ^{12}C are shown in Figure 1.6.

The large experimental uncertainty of this electromagnetic property calls for a more precise measurement of the $Q(2_1^+)$ in ^{12}C as an opportunity to benchmark and help fine-tune state-of-the-art *ab initio* calculations using chiral EFT interactions. The measurement of this electromagnetic property with the aim of achieving an improved accuracy is the work described in the present dissertation.

The details of the Coulomb excitation reorientation-effect experiment performed at the JYFL in Jyväskylä will be described in detail in section 3. The experiment consisted of the Coulomb excitation of both a ^{12}C beam and a ^{208}Pb target. By measuring the de-exciting γ -rays from both the projectile and target, the $Q(2_1^+)$ in ^{12}C can be extracted using the modern Coulomb excitation code GOSIA [Czo83]. The details about the analysis as well as the results and their interpretation will be discussed in chapters 4 and 5.

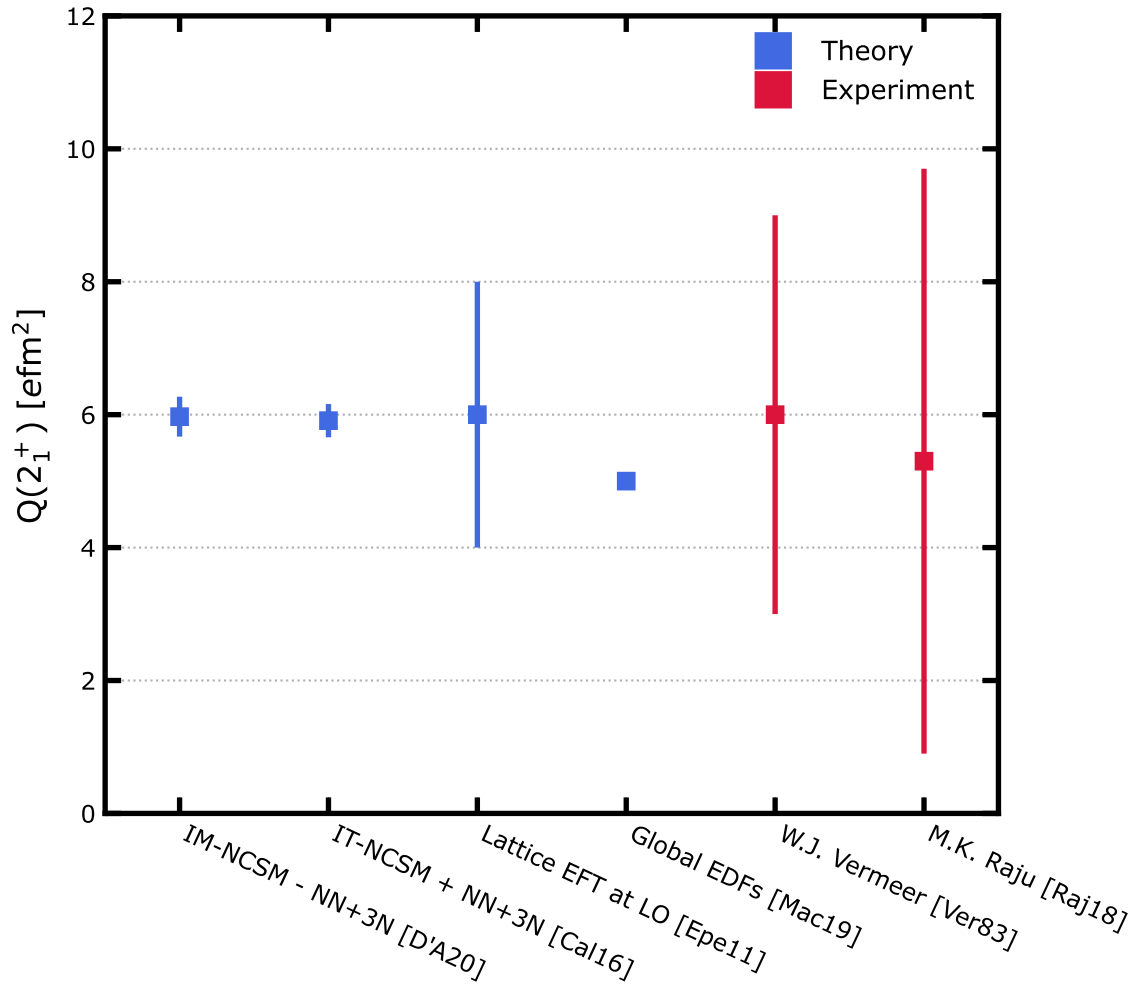


Figure 1.6: Different theoretical and experimental values for the $Q(2_1^+)$ in ^{12}C . From the left to the right: IM-NCSM and IT-NCSM using chiral NN+3N interactions [D'A20, Cal16], Nuclear Lattice EFT at LO [Epe11], Global EDFs [Mac19], adopted value (experimental) [Ver83] and recent measurement result [Raj18].

Chapter 2

Coulomb excitation

This chapter aims to give a brief summary of the main aspects of the semi-classical theory of Coulomb excitation relevant to the present dissertation. This will include first and higher-order perturbation theories, with an emphasis on the second-order terms, such as the GDR effect, the reorientation effect, and the effect of the quadrupole moment on measured Coulomb excitation cross section. Finally, an overview of the Coulomb excitation code GOSIA [Czo83] will be given. The detailed derivations and more rigorous formalism can be found in [Ald75].

2.1 Introduction

The excitation of nuclear states by means of the electromagnetic field of impinging nuclei, i.e. Coulomb excitation, is a powerful technique to probe nuclear collectivity. Through Coulomb excitation, collective states are selectively populated with cross sections that are a direct measure of the electromagnetic matrix elements [Czo83, Ald75].

It has been proven that a semi-classical treatment is valid in almost all situations studied in Coulomb excitations at energies well below the Coulomb barrier [Ald75]. The term “semi-classical” arises from the classical treatment of the particle trajectories and the quantum-mechanical treatment of the electromagnetic excitation

process. For higher energy collisions, a full quantum treatment might be necessary for the computation of some observables, since the nuclear interaction distorts the scattering waves appreciably [Ber09]. However, the use of full quantal codes in current computers is impractical when handling the large number of coupled channels in some, mostly heavy-ion, Coulomb excitation calculations. These calculations would need to handle the long range of the Coulomb interaction, coupled with the small integration step size required by the short wavelength, and the large number of partial waves that make significant contributions, resulting in very high computation times [Czo83].

2.2 The Semi-Classical Approximation

The great simplification of the semi-classical treatment exploits the fact that only the Coulomb field (the monopole-monopole interaction, $Z_1 Z_2 e^2 / r$) can ensure that the projectile does not penetrate into the nucleus, and determines the relative motion of the two colliding nuclei. This means that the wavelength λ of the incident projectile wave-packet must be small when compared to the dimensions of the classical hyperbolic trajectory, i.e. the half-distance of closest approach b in a head-on collision. If this is fulfilled, the projectile wave-packet will follow the classical hyperbolic orbit quite accurately. This condition of applicability of classical physics for the description of the relative motion of the nuclei can be expressed in terms of the dimensionless Sommerfeld parameter,

$$\eta = \frac{b}{2\lambda} = \frac{Z_1 Z_2 e^2}{\hbar v} \gg 1, \quad (2.1)$$

where Z_1 and Z_2 are the atomic numbers of the projectile and the target, and v is the relative velocity between projectile and target at large distances.

The basic assumption of Coulomb excitation, and therefore another condition for the validity of the semi-classical approximation, is that the interaction between

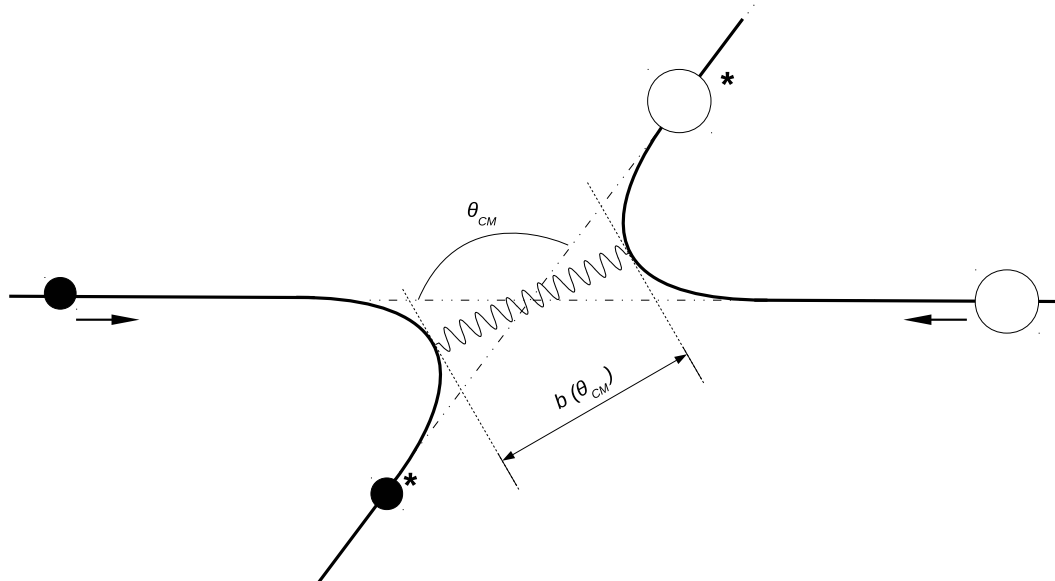


Figure 2.1: Schematic representation of the inelastic-scattering process (Coulomb excitation) of two colliding nuclei in the centre of mass frame.

both colliding nuclei is purely electromagnetic. The usual way to ensure this is by defining a minimum “safe” separation distance between the surfaces of the two collision partners, above which the contribution of the nuclear force is negligible. This “safe” distance has been experimentally determined to be of approximately 5 fm [Cli86], giving a “safe” energy criterion for Coulomb excitation experiments involving heavy-ions. Conversely, for the case of lighter nuclei ($Z \leq 6$), a more detailed analysis is required to estimate reliably the importance of both Coulomb-nuclear interference effects and quantal effects on Coulomb excitation at near-barrier bombarding energies. A complete analysis on the latter using different fully quantal codes is included in section 4.3.

Furthermore, for the applicability of the classical picture, it is essential that the energy loss by the projectile to the target nucleus due to electromagnetic excitation, ΔE , is small when compared to the incident projectile energy $\Delta E/E \ll 1$. This condition arises from the fact that the point of the trajectory at which the energy is transferred is unknown, and therefore cannot be included in any accurate way. The

semi-classical picture makes the assumption of the energy ΔE being exchanged at the point of closest approach.

The Coulomb excitation experiment of ^{12}C on ^{208}Pb at an energy of 47.65 MeV (see section 3.1 for further experimental details) yields a value of $\eta \approx 38.9 \gg 1$, and a maximum relative energy loss due to projectile excitation for the high-lying 2_1^+ of $\Delta E/E \approx 0.09 \ll 1$. This makes the present Coulomb excitation study fulfil the requirements for the use of the semi-classical approximation. As a result, the Coulomb excitation cross section, can be expressed as the product of the ‘‘Rutherford’’ cross section (σ_R) and the probability (P_n) of exciting a given state, $|n\rangle$,

$$\frac{d\sigma_n}{d\Omega} = P_n \cdot \frac{d\sigma_R}{d\Omega}, \quad (2.2)$$

where the classical Rutherford cross section is given by

$$\frac{d\sigma_R}{d\Omega} = \frac{a^2}{\sin^4 \frac{\theta}{2}}, \quad (2.3)$$

where θ is the scattering angle in the center of mass frame and a is the half distance of closest approach in a head-on collision, b (equation 2.1).

2.2.1 First-order Perturbation theory

When an incident projectile nucleus collides with a target nucleus, the resulting inelastic-scattering process can be expressed in terms of the time-dependent Schrödinger equation

$$i\hbar \frac{\delta}{\delta t} |\Psi_{1,2}(t)\rangle = H_{1,2} |\Psi_{1,2}(t)\rangle, \quad (2.4)$$

where the numbers 1 and 2 denote the projectile or target excitation, respectively. The excitation process can be described by the time-dependent Hamiltonian in terms

of a multipole expansion [Boh69],

$$i\hbar \frac{\delta}{\delta t} |\Psi_{1,2}(t)\rangle = [H_{1,2}^0 + V_{1,2}(\vec{r}(t))] |\Psi_{1,2}(t)\rangle, \quad (2.5)$$

where $H_{1,2}^0 = Z_1 Z_2 e^2 / r$ corresponds to the monopole-monopole term, which treats the elastic ‘‘Rutherford’’ cross section, and $V_{1,2}(\vec{r}(t))$ is the monopole-multipole term, which accounts for the inelastic excitation of either the projectile or target. The missing higher-order multipole-multipole terms accounting for the mutual excitation of both projectile and target are small when compared to the individual excitation of either partner and can thus be neglected. The indices 1 and 2 referring to either projectile or target are interchangeable and can therefore be omitted from this point onwards.

The wave function of the scattered nucleus (projectile or target) after the collision can be expressed as

$$\Psi(t) = \sum_{n=0} a_n(t) \Phi_n(t) = \sum_{n=0} a_n(t) |n\rangle, \quad (2.6)$$

where n denotes the sum over all final states ($n = 0$ represents the elastic-scattering case). The probability of exciting the atomic nucleus from its ground state to a state $|n\rangle$ is given by

$$P_{0 \rightarrow n} = |a_n|^2, \quad (2.7)$$

or in general, for the case of a multi-level system, the probability of exciting any final state $|f\rangle$ from an initial state $|i\rangle$ with angular momentum I_i [Ald75],

$$P_{i \rightarrow f} = \frac{1}{2I_i + 1} \sum_{M_i, M_f} |a_{if}|^2, \quad (2.8)$$

where M_i and M_f denote the magnetic substates of the initial and final states, respectively.

The excitation amplitude a_{if} can only be evaluated by first-order perturbation theory if the interaction between projectile and target is weak, and if the excitation amplitudes of all possible transitions from the ground state as well as from the final state are also weak [Ald75]. Given this scenario, the excitation amplitude a_{if} of the final state $|I_f M_f\rangle$ from an initial state $|I_i M_i\rangle$ is given by

$$a_{if} = \frac{1}{i\hbar} \int_{-\infty}^{+\infty} \langle I_f M_f | V(\vec{r}(t)) | I_i M_i \rangle \exp\left\{ \frac{i}{\hbar} (E_f - E_i) t \right\} dt. \quad (2.9)$$

Considering the case of an electric excitation (instead of magnetic excitation), the monopole-multipole interaction, $V(\vec{r}(t))$, is given by

$$V(\vec{r}(t)) = \sum_{\lambda=1}^{\infty} \sum_{\mu=-\lambda}^{\mu=\lambda} \frac{4\pi e Z'}{2\lambda+1} (-1)^\mu \frac{Y_{\lambda\mu}(\theta(t), \phi(t))}{r(t)^{\lambda+1}} \mathcal{M}(E\lambda, -\mu), \quad (2.10)$$

where Z' is the atomic number of the opposite collision partner and $Y_{\lambda\mu}(\theta(t), \phi(t))$ denotes standard normalised spherical harmonics. The symbol $\mathcal{M}(E\lambda, \mu)$ stands for electric multipole moments of the excited nucleus and is given by [Boh69]

$$\mathcal{M}(E\lambda, \mu) = \int \rho(\vec{r}) r^\lambda Y_{\lambda\mu} d^3\vec{r}. \quad (2.11)$$

Here $\rho(\vec{r})$ being the spatial charge distribution of a free nucleus.

By introducing equation 2.10 into 2.9, the excitation amplitude yields

$$a_{if} = \frac{4\pi Z' e}{i\hbar} \sum_{\lambda, \mu} \frac{1}{2\lambda+1} \langle I_f M_f | \mathcal{M}(E\lambda, \mu) | I_i M_i \rangle S_{E\lambda, \mu}(\theta, \xi) \quad (2.12)$$

Note that $(-1)^\mu \mathcal{M}(E\lambda, -\mu) = \mathcal{M}(E\lambda, \mu)$ and that notation to describe the orbital integrals ($S_{E\lambda, \mu}(\theta, \xi)$) has been introduced,

$$S_{E\lambda, \mu}(\theta, \xi) = \int_{-\infty}^{+\infty} e^{\frac{i}{\hbar}(E_f - E_i)t} \bar{S}_{E\lambda, \mu}(\theta, \xi) dt = \int_{-\infty}^{+\infty} e^{\frac{i}{\hbar}(E_f - E_i)t} \frac{Y_{\lambda\mu}(\theta(t), \phi(t))}{r(t)^{\lambda+1}} dt, \quad (2.13)$$

where θ is the scattering angle and ξ represents the adiabacity parameter.

The Wigner-Eckart theorem can now be used to express equation 2.12 in terms of the reduced matrix element

$$a_{if} = \frac{4\pi Z'e}{i\hbar} \sum_{\lambda,\mu} \frac{1}{2\lambda+1} (-1)^{I_f-M_f} \begin{pmatrix} I_f & \lambda & I_i \\ -M_f & \mu & M_i \end{pmatrix} \langle I_f || \mathcal{M}(E\lambda) || I_i \rangle S_{E\lambda,\mu}(\theta, \xi) \quad (2.14)$$

Analogously, we can re-write equation 2.14 in terms of the dimensionless integral $R_{\lambda,\mu}(\theta, \xi)$ in order to separate the complicated dependence of the orbital integrals $S_{\lambda,\mu}(\theta, \xi)$ on the kinematics of the hyperbolic motion, from the dependence on the scattering angle θ and adiabacity parameter ξ , which depend on the incident particle energy and nuclear excitation energy

$$a_{if} = \frac{4\pi Z'e}{i\hbar v} \sum_{\lambda,\mu} \frac{1}{a^\lambda} \frac{(\lambda-1)!}{(2\lambda+1)!!} \sqrt{\frac{2\lambda+1}{\pi}} (-1)^{I_f-M_f} \begin{pmatrix} I_f & \lambda & I_i \\ -M_f & \mu & M_i \end{pmatrix} \times \\ \times \langle I_f || \mathcal{M}(E\lambda) || I_i \rangle R_{\lambda,\mu}(\theta, \xi). \quad (2.15)$$

Using the orthogonality properties of the 3-j symbols, we can obtain a more compact expression for the excitation probability of the state of spin I_f by using equations 2.8 and 2.15

$$P_{i \rightarrow f} = \sum_{\lambda} \left| \chi_{i \rightarrow f}^{(\lambda)} \right|^2 R_{\lambda}^2(\theta, \xi) \quad (2.16)$$

where the dependence on θ and ξ has been separated through [Ald75]

$$R_{\lambda}^2(\theta, \xi) = \sum_{\mu} |R_{\lambda,\mu}(\theta, \xi)|^2. \quad (2.17)$$

The dimensionless quantity $\chi_{i \rightarrow f}^{(\lambda)}$ is an indicator of the interaction strength for a transfer of angular momentum $\lambda\hbar$ and z-component $-\mu\hbar$, and is defined as

$$\chi_{i \rightarrow f}^{(\lambda)} = \frac{\sqrt{16\pi}(\lambda-1)!}{(2\lambda+1)!!} \frac{Z'e}{\hbar v} \frac{\langle I_f || \mathcal{M}(E\lambda) || I_i \rangle}{a^\lambda \sqrt{2I_i+1}}, \quad (2.18)$$

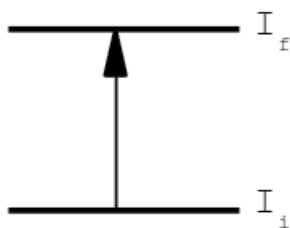


Figure 2.2: Schematic representation of the first-order contribution to the Coulomb excitation process or single-step excitation.

and is subject to selection rules

$$|I_i - I_f| < \lambda < |I_i + I_f| \quad (2.19)$$

$$-M_i + M_f = -\mu. \quad (2.20)$$

The differential cross section for each electric multipole excitations can be written in the form

$$d\sigma = \sum_{\lambda} d\sigma_{E\lambda}, \quad (2.21)$$

and we can use equations 2.2 and 2.3 yielding

$$d\sigma_{E\lambda} = \frac{a^2}{\sin^4 \frac{\theta}{2}} \cdot P_{i \rightarrow f} d\Omega. \quad (2.22)$$

Finally, we can use equations 1.14, 2.16 and 2.18 to obtain an expression for the differential Coulomb excitation cross section for each electric multipole:

$$\frac{d\sigma_{E\lambda}}{d\Omega} = \left(\frac{Z'e}{\hbar v} \right)^2 a^{-2\lambda+2} B(E\lambda, I_i \rightarrow I_f) 4\pi \left[\frac{(\lambda-1)!}{(2\lambda+1)!!} \right]^2 \frac{R_{\lambda}^2(\theta, \xi)}{\sin^4 \frac{\theta}{2}} \quad (2.23)$$

2.2.2 Higher-order perturbation theory

The Coulomb excitation probabilities, as well as the cross sections, are quadratic expressions in the amplitudes and can therefore be expanded in a power series of

the interaction strength χ ,

$$P_f = a_2\chi^2 + a_3\chi^3 + a_4\chi^4 + \dots \quad (2.24)$$

These χ parameters connect the initial and final states through all possible excitation paths, and the coefficients a_λ are functions of θ and ξ . The $a_2\chi^2$ term in equation 2.24 corresponds to the first-order or one-step excitation. The second term represents the interference of the first-order amplitude with the amplitude for a two-step excitation. The third term corresponds to interference between first-order and three-step amplitudes plus combinations of two-step amplitudes [Ver84a].

Alternatively, the excitation probability can be represented as a set of coupled differential equations on the excitation amplitudes a_{if} , which will now depend on the couplings to all states z . Therefore, the amplitude for exciting a certain state f from an initial state i , will depend on couplings to all other states as [Czo83]

$$\frac{da_{if}}{dt} = -i\frac{4\pi Z'e}{\hbar} \sum_z a_z(t) \exp\left\{\frac{it}{\hbar}(E_f - E_z)\right\} \sum_{\lambda\mu} (-1)^\mu \cdot \bar{S}_{E\lambda,\mu}(t) \langle \Phi_f | \mathcal{M}(\lambda, \mu) | \Phi_z \rangle. \quad (2.25)$$

This set of coupled differential equations requires to be solved numerically, and codes such as GOSIA have been developed to perform this task. The code GOSIA will be introduced in section 2.3 and a detailed description of the different numerical methods employed by this code can be found in [Czo83].

2.2.3 Second-order perturbation theory

It is of special interest to the present work to discuss in further detail the excitation probabilities to a second-order, since some of the terms of order χ^3 are particularly relevant to the Coulomb excitation experiment of ^{12}C in ^{208}Pb . These χ^3 terms include the reorientation effect and the Giant Dipole Resonance (GDR) effect. A schematic representation of the terms of order χ^2 and χ^3 are shown in Figure 2.3.

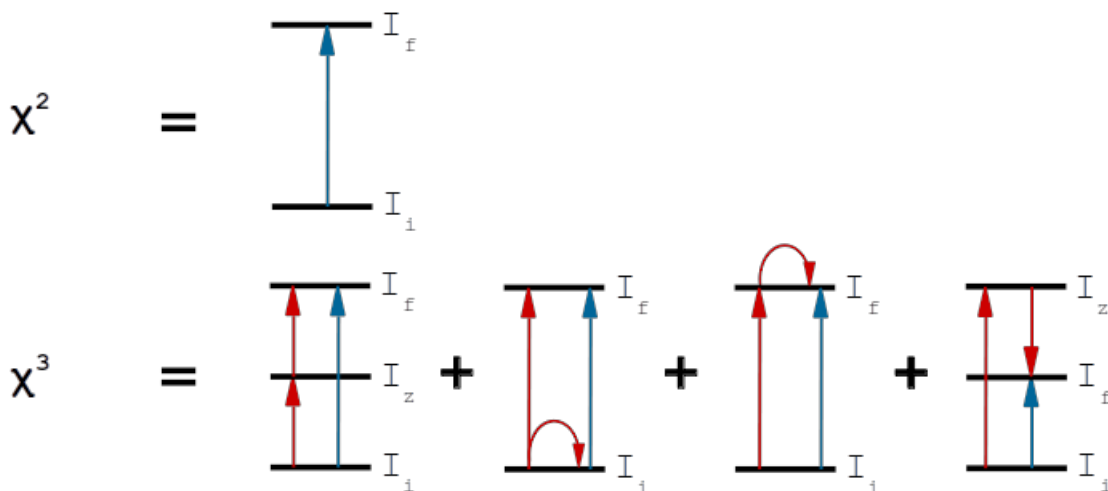


Figure 2.3: Schematic representation of the interaction strength (or excitation probability) terms of order χ^2 and χ^3 . The blue arrows represent the single-step first-order excitation interfering with the second-order multi-step terms in red, which include different modes of multi-step excitations and reorientation effects.

In relation to an even-even nucleus, the first-excited state is the 2_1^+ which is populated via one-step Coulomb excitation from the ground state and also through a double-step excitation (see Figure 2.4 left). The probability of populating this 2_1^+ state is, to a second-order, [Ald75]

$$P_{2^+} = \left| \chi_{0^+ \rightarrow 2^+}^{(E2)} \right|^2 R_2^2(\theta, \xi) (1 + y c(\theta, s, \xi)), \quad (2.26)$$

where

$$y = \frac{\chi_{0^+ \rightarrow I_f} \chi_{I_f \rightarrow 2^+}}{\chi_{0^+ \rightarrow 2^+}} = \chi_{0^+ \rightarrow I_f} \frac{1}{\sqrt{2I_f + 1}} \frac{\langle 2^+ || \mathcal{M}(E2) || I_f \rangle}{\langle 2^+ || \mathcal{M}(E2) || 0^+ \rangle} \quad (2.27)$$

and $c(\theta, s, \xi)$ and $R_2^2(\theta, \xi)$ are functions that isolate the dependence on scattering angle and adiabacity parameter, and $s = \frac{E_z - E_0}{E_{2^+} - E_0}$ is the ratio of the excitation energies between the 2_1^+ state and the intermediate state I_f . Here it is assumed that the multi-step excitation is the main relevant second-order effect contributing to the excitation probability.

As it is stated in equation 2.26, the probability of exciting this 2_1^+ to a second-order is given by the total probability of populating this state through a single-

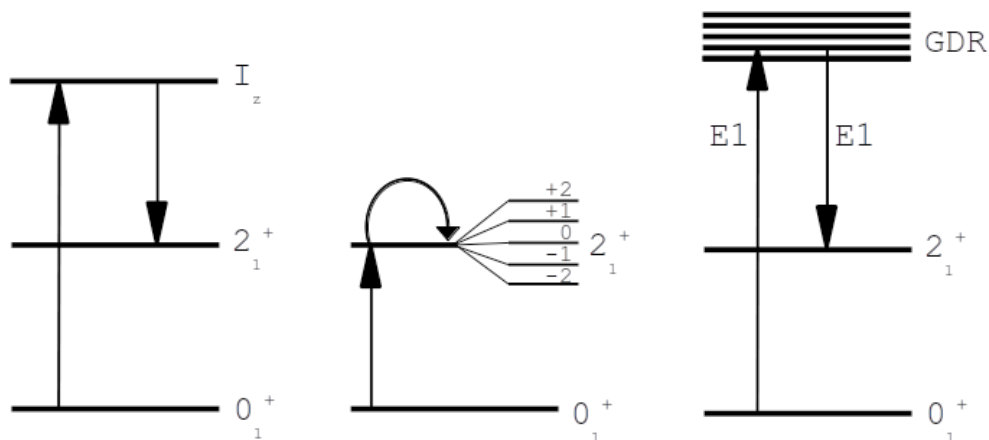


Figure 2.4: Schematic representation of the 2_1^+ excitation process of an even-even nucleus through: multi-step excitation (left), single-step and reorientation (middle) and through the GDR resonance (right).

step process, plus the interference between the latter and the multi-step excitation process. This interference will be either constructive or destructive depending on the sign of the matrix elements in equation 2.27.

2.2.4 The Reorientation effect

The authors Breit and Lazarus (1955) were the first to suggest the possibility of measuring a static quadrupole moment by Coulomb excitation, and they also introduced the term “reorientation effect” for the first time [Bre55].

Although the term “reorientation effect” is used in general to refer to the effects of the static quadrupole moment in Coulomb excitation, it strictly describes virtual transitions responsible for the redistribution of the final populations of the magnetic substates of the final state. The term arises from the “reorientation” of the nuclear spin of the final state. This change in the nuclear spin has an effect on, for example, the distribution of the de-excitation γ rays and, as it will be shown shortly, in the excitation probability, i.e. the Coulomb excitation cross section.

If we assume that the nuclear reorientation is the main second-order effect contributing to the excitation of the 2_1^+ state of an even-even nucleus, we can apply equations 2.26 and 2.27 for the case where the final state I_f is a different magnetic

substate of the same 2_1^+ state (see Figure 2.4 middle). As a result, the excitation probability will be given by

$$P_{2^+} = \left| \chi_{0^+ \rightarrow 2^+}^{(E2)} \right|^2 R_2^2(\theta, \xi) \left(1 + \chi_{2^+ \rightarrow 2^+}^{(E2)} c(\theta, s = 1, \xi) \right), \quad (2.28)$$

where

$$\chi_{2^+ \rightarrow 2^+}^{(E2)} = \frac{4}{15} \sqrt{\frac{\pi}{5}} \frac{Ze}{\hbar v a^2} \langle 2^+ || E2 || 2^+ \rangle, \quad (2.29)$$

and using equation 1.15,

$$\chi_{2^+ \rightarrow 2^+}^{(E2)} = \sqrt{\frac{7}{90}} \frac{Ze}{\hbar v} Q_{2^+}. \quad (2.30)$$

As a result, through the accurate measurement of the excitation probability (i.e. the cross section) to the 2_1^+ state, one can extract a value for the quadrupole moment of that 2_1^+ . Figure 2.5 shows the Coulomb excitation differential cross section for the 2_1^+ in ^{12}C calculated with GOSIA for different values of the $Q(2_1^+)$. As it has been shown, the sensitivity to the $Q(2_1^+)$ increases with the laboratory scattering angle, which is the property that has been exploited in the present work by covering the expected backward scattering angles with the particle detector in the planned experiment (see Chapter 3 for the experimental details).

2.2.5 The GDR effect

A detailed theoretical description of the GDR effect can be found in [Ald75]. In this section, a brief description of this effect together with the most relevant equations for the present dissertation will be discussed.

The virtual excitations via the Giant Dipole Resonance are another second-order effect accompanying the nuclear reorientation that may be measurable. To second-order, this effect can be quantified by the interference between the direct Coulomb excitation amplitude of a certain state and the amplitude for the two-step excitation of that state, where the intermediate step consists of the virtual excitation of states

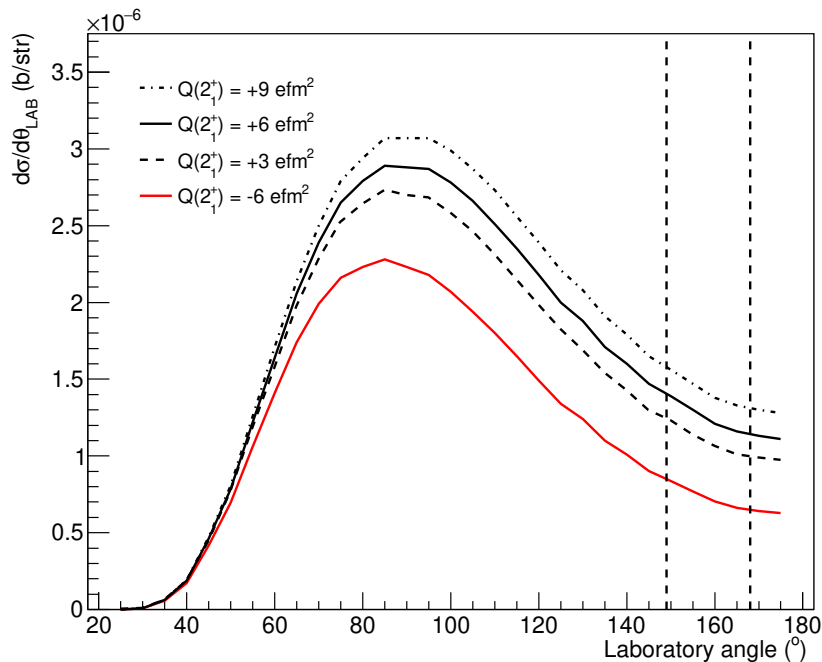


Figure 2.5: Coulomb excitation differential cross section for the excitation of the 2_1^+ in ^{12}C for different values of the $Q(2_1^+)$. The calculations were performed with GOSIA [Czo83].

within the GDR (see Figure 2.4 right). This GDR effect is also referred to as nuclear polarization, which is an alternative picture where the electric field of the impinging nucleus induces a transitory electric-dipole moment in the nucleus undergoing Coulomb excitation.

The set of coupled differential equations introduced in 2.25 may be used as a starting point for the description of the GDR effect. This set of equations can be rewritten in a more compact form without expanding the interaction potential in electric multipoles as [Ald75]

$$i\hbar \frac{da_n}{dt} = \sum_m a_m(t) \langle n|V(t)|m\rangle \exp\left\{\frac{it}{\hbar}(E_n - E_m)\right\}, \quad (2.31)$$

where a_n denotes the excitation amplitude of the final state $|n\rangle$, ($a_{if} = a_n$), and the intermediate states coupled to the state $|n\rangle$ are denoted as $|m\rangle$, ($a_z = a_m$).

We can now denote the group of high-lying states within the GDR by $|z\rangle$ and

$|z'\rangle$, which are strongly coupled to the low-lying $|n\rangle$ and $|m\rangle$ states, that are also mutually strongly coupled. Then, equation 2.31 yields

$$i\hbar \frac{da_n}{dt} = \sum_m a_m \langle n|V(t)|m\rangle \exp\left\{\frac{it}{\hbar}(E_n - E_m)\right\} + \sum_z a_z \langle n|V(t)|z\rangle \exp\left\{\frac{it}{\hbar}(E_n - E_z)\right\} \quad (2.32)$$

and

$$i\hbar \frac{da_z}{dt} = \sum_{z'} a_{z'} \langle z|V(t)|z'\rangle \exp\left\{\frac{it}{\hbar}(E_z - E_{z'})\right\} + \sum_m a_m \langle z|V(t)|m\rangle \exp\left\{\frac{it}{\hbar}(E_z - E_m)\right\} \quad (2.33)$$

If we now assume that $|E_z - E_n| \gg |E_z - E_{z'}|$ and that $|E_z - E_n| \gg |E_n - E_m|$, it can be shown that the interaction potential in equation 2.33, $V(t)$, can be modified by the addition of a polarization potential $V_{\text{pol}}(t)$ [Ald75],

$$i\hbar \frac{da_n}{dt} = \sum_m a_m \langle n|V(t) + V_{\text{pol}}(t)|m\rangle \exp\left\{\frac{it}{\hbar}(E_n - E_m)\right\}, \quad (2.34)$$

where, to the first-order,

$$\langle n|V_{\text{pol}}(t)|m\rangle = - \sum_z \frac{\langle n|V(t)|z\rangle \langle z|V(t)|m\rangle}{E_z - E_m}. \quad (2.35)$$

Here higher order terms such as $(E_z - E_m)^{-2}$ involving, for example, transitions within the $z \rightarrow z'$ states are neglected.

The potential $V(t)$ in equation 2.35 can be expanded using a multipole expansion and, eventually, a set of coupled differential equations for arbitrary spins and multiplicities is reached (see reference [Few78] for the full derivation of the complete set of differential equations). However, many of the matrix elements involved in these equations are unknown, most noticeably the ones connecting the GDR states with

the low-lying excited states. This has led to the use of nuclear models, such as the hydrodynamic model, to describe the previously mentioned polarization potential.

For nuclear states which are described by nuclear quadrupole deformation, the nuclear surface can be parametrised in terms of spherical harmonics of the type $Y_{2\mu}^*(\theta, \phi)$ as

$$R(\theta, \phi) = R_0 \left[1 + \sum_{\mu} \alpha_{2\mu} Y_{2\mu}^*(\theta, \phi) \right], \quad (2.36)$$

where R_0 denotes the equilibrium radius of the nucleus and $\alpha_{2\mu}$ are the deformation parameters that describe the nuclear surface. As shown in [Ald75], within the framework of the hydrodynamic model, the induced dipole moment on a deformed nucleus of this type gives rise to a polarization potential V_{pol} of the form

$$V_{\text{pol}} = -P_0 \vec{E}^2 \left[1 + 2 \sum_{\mu} \alpha_{2\mu} Y_{2\mu}^*(\theta, \phi) \right], \quad (2.37)$$

where the electric field strength at the nucleus is

$$|\vec{E}| = Z_1 \frac{e}{r^2}, \quad (2.38)$$

and P_0 is the nuclear polarizability as defined by Levinger [Lev57]. This nuclear polarizability can be estimated from the (-2) moment of the total photo-nuclear absorption cross section, σ_{-2} , as

$$P_0 = \frac{\hbar c}{4\pi^2} \sigma_{-2}. \quad (2.39)$$

Hydrodynamic-model estimates for the total photo-nuclear absorption cross section [Mig44], yield values for the σ_{-2} of the type

$$\sigma_{-2} = \int \sigma(E) E^{-2} dE = k_0 A^{5/3}. \quad (2.40)$$

Moreover, values of the σ_{-2} have been measured experimentally and were fitted by

Levinger [Lev57] concluding that $k_0 = 3.5 \mu\text{b}/\text{MeV}$ gave a fairly accurate fit to the experimental data for heavy nuclei, whilst the same fit was not as good for the lighter nuclei. Recently, other authors [Orc15] found the best fit for $k_0 = 2.4 \mu\text{b}/\text{MeV}$ by using new experimental data available for the σ_{-2} . The deviation of the σ_{-2} from the hydrodynamic model estimates are typically accounted for by introducing a parameter k , known as nuclear polarizability constant. The expression for the σ_{-2} then is

$$\sigma_{-2} = 3.5kA^{5/3} \mu\text{b}/\text{MeV}, \quad (2.41)$$

using Levinger's fit and corresponding $k = 1$ to the hydrodynamic-model estimate.

Assuming that vibrational and rotational models hold, we can express the deformation parameters $\alpha_{2\mu}$ as

$$\mathcal{M}(E2, \mu) = \frac{3}{4\pi} Z_2 e R_0^2 \alpha_{2\mu}, \quad (2.42)$$

and by using equations 2.41 and 2.39, and substituting 2.38 and 2.42 into 2.37, the polarization potential results in

$$V_{\text{pol}} = -\frac{e^2 Z_1^2 \hbar c}{4\pi^2} \frac{\sigma_{-2}}{r^4} \left[1 + \frac{8\pi}{3e Z_2 R_0^2} \sum_{\mu} \mathcal{M}(E2, \mu) Y_{2\mu}^*(\theta, \phi) \right]. \quad (2.43)$$

The total effective interaction potential will then be an addition of the $E2$ interaction with the above mentioned polarization potential,

$$V_{\text{eff}}(E2) = V_{\text{EE}}(\lambda = 2) + V_{\text{pol}}, \quad (2.44)$$

and using equations 2.10 (for $\lambda = 2$) and 2.43, the effective potential results in

$$\begin{aligned}
 V_{\text{eff}}(E2) &= \frac{4\pi eZ_1}{5r^3} \left[1 - \frac{5Z_1\hbar c\sigma_{-2}}{6\pi^2 Z_2 R_0^2} \cdot \frac{1}{r} \right] \sum_{\mu} \mathcal{M}(E2, \mu) Y_{2\mu}^*(\theta, \phi) = \\
 &= V_{\text{EE}}(\lambda = 2) \left[1 - \frac{5Z_1\hbar c\sigma_{-2}}{6\pi^2 Z_2 R_0^2} \cdot \frac{1}{r} \right]. \quad (2.45)
 \end{aligned}$$

If we now substitute once more equation 2.41 into 2.45, and we consider $R_0 = 1.2A^{1/3}$,

$$V_{\text{eff}}(E2) \approx V_{\text{EE}}(\lambda = 2) \left[1 - 0.0056k \frac{A_2 E_{\text{MeV}} a}{Z_2^2 (1 + A_1/A_2) r} \right], \quad (2.46)$$

where E_{MeV} is the energy in MeV and a is the half-distance of closest approach in a head-on collision. Equation 2.46 is implemented in the Coulomb excitation code used for the analysis of the experimental data, GOSIA, and the value of the nuclear polarizability constant k can be modified to account for the couplings to the GDR. A description of the main features of the code will be presented in the following section and the analysis of the nuclear polarizability (or GDR effect) for the present experiment will be discussed in section 4.4.2.

2.3 GOSIA

The development of a code to analyse data extracted from Coulomb excitation experiments was first accomplished by Winther and deBoer in 1965 [Win66]. The code COULEX used the semi-classical theory of Coulomb excitation developed by [Ald75] to calculate, for the first time, multi-step Coulomb excitation amplitudes using an assumed set of the reduced electromagnetic matrix elements. However, the extraction of nuclear-structure properties in a model-independent way is still limited by the large number of reduced matrix elements with a significant contribution to the Coulomb excitation process in experiments involving heavy-ions.

The GOSIA code was developed for this purpose at the Nuclear Structure Re-

search Laboratory of the University of Rochester in 1980 by Tomasz Czosnyka, Douglas Cline and Ching-Yen Wu. GOSIA can calculate excitation cross sections following multiple Coulomb excitation in a model-independent way treating higher-order multipolarities which, amongst other limitations, was not possible with the original Winther and deBoer code.

2.3.1 Introduction

GOSIA is a suite of Coulomb excitation codes that was designed to handle heavy-ion induced Coulomb excitation where the population of many excited states is measured using coincident detection of the scattered ions and the de-excitation γ -ray. Although providing the possibility of running theoretical calculations, GOSIA is an experiment-oriented program designed to fit matrix elements to best reproduce large experimental data sets. These matrix elements are not only fitted to the measured de-excitation γ -ray yields but also to other available spectroscopic information such as branching ratios, $E2/M1$ mixing ratios, lifetimes and previously measured $E1 - E6$ and $M1$ matrix elements.

The population of the different nuclear states is calculated by integrating the coupled differential equations 2.25 numerically, making use of the fast approximation method (see GOSIA manual [Czo83]). The subsequent decay is then treated by computing the γ -ray's angular distribution. The calculated γ -ray yields are used in a least-squares minimisation process where a χ^2 -type least-squares statistic is normalised to the total number of data points.

2.3.2 The minimisation process

GOSIA starts with a set of matrix elements, or initial guess, given by the user. It also receives information on the experimental conditions (detectors' position and sizes, beam energy, target thickness, etc.) and spectroscopic information (level scheme of the collision partners, matrix elements, lifetimes, etc.) as an input. Then it cal-

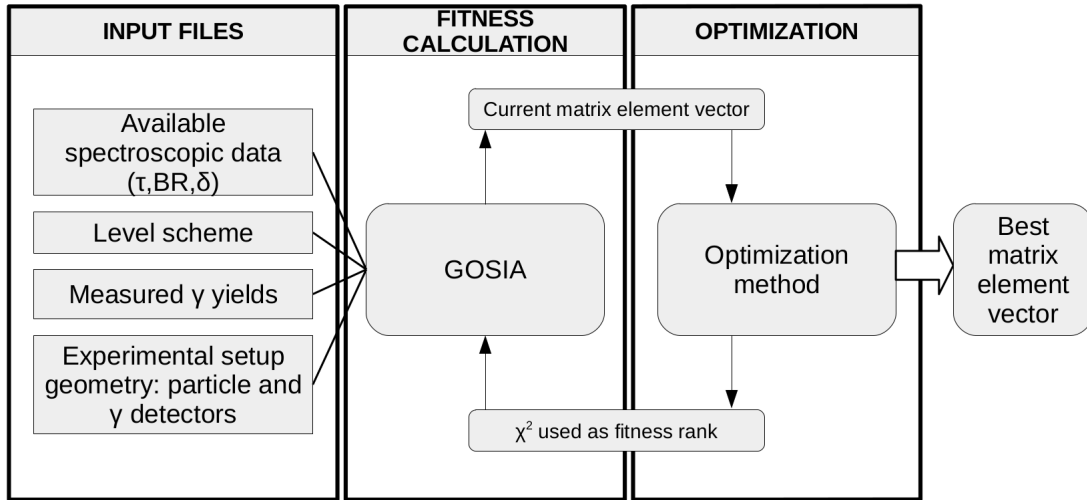


Figure 2.6: GOSIA dataflow scheme

calculates the corresponding γ -ray yields and subsequently constructs a least-squares statistic, $S(\bar{M})$, built on the observed and calculated γ -ray yields. For this last step, it takes into account known spectroscopic data related to the matrix elements, experimental γ -ray yields are integrated over the scattering angle and energy range of the incident projectile, and includes effects influencing the γ -ray yields (such as internal conversion, size of the Ge detectors, deorientation effect, γ -ray angular distribution, etc). The process is then repeated until reaching a minimum value which corresponds to the set of matrix elements that better reproduces the experimental γ -ray yields. Figure 2.6 shows a scheme of the dataflow in GOSIA.

As described in the manual [Czo83], $S(\bar{M})$ is χ^2 -type function normalised to the number of data points rather than the number of degrees of freedom, i.e.

$$S(\bar{M}) = \frac{1}{N} \chi^2 = \frac{1}{N} \left(S_y + S_1 + \sum_i w_i S_i \right), \quad (2.47)$$

where the total number of data points, N , includes the measured γ -ray yields and known spectroscopic information. The symbols S_y , S_I and S_i denote different contributions to the χ^2 function arising from various subsets of the data:

- S_y is defined as

$$S_y = \sum_{i',j} w_{i'j} \sum_{k(i',j)} \frac{1}{\sigma_k^2} (C_{i'j} Y_k^C - Y_k^E)^2 \quad (2.48)$$

and accounts for the contribution of the measured γ -ray yields. The summations extend over all experiments (i'), γ -detectors (j) and observed γ -ray transitions (k). The weights (w_{ij}) can be chosen for each experiment and γ -detector independently, and give control to the user during the minimisation. Y_k^C denote the calculated yields for the set of matrix elements at this point of the minimisation, and Y_k^E represent the measured γ -ray yields with uncertainty σ_k . The coefficients C_{ij} are normalisation factors, connecting calculated and experimental yields.

- The quantity S_1 is used to avoid finding physically unreasonable solutions by preventing the minimisation procedure from producing γ -ray transitions which were expected, but had not been observed.
- S_i term is defined as:

$$S_i = \sum_{n_i} (d_{n_i}^C - d_{n_i}^E)^2 \frac{1}{\sigma_{n_i}^2} \quad (2.49)$$

where n_i stands for all the spectroscopic data included in the input to GOSIA, $d_{n_i}^C$ and $d_{n_i}^E$ represent the calculated (i.e. resulting from the fit) and experimental (introduced in the input) spectroscopic data points respectively, and σ_{n_i} its associated uncertainty.

For the present analysis, GOSIA2, a special version of GOSIA designed to handle both the projectile and target excitation was used. GOSIA2 allows the performance of the simultaneous χ^2 minimisation of the matrix elements for both collision partners by normalising to a reference known reduced matrix element in one of them. As it will be shown in Chapters 3 and 4, the $B(E3; 0_1^+ \rightarrow 3_1^-)$ in ^{208}Pb was chosen as the normalisation transition due to its reduced uncertainty.

2.3.3 Systematic uncertainties and limitations

One of the main sources of systematic error to consider when using GOSIA arises from the accuracy of the semi-classical approximation. The difference between fully quantal and the semi-classical calculations is largely corrected by the symmetrisation of the orbit; the remaining quantal correction to the calculated cross sections is of the order of $1/\eta$ [Ald69, Ald72]. Nonetheless, quantal effects tend to cancel each other out, as it is usually the ratios of γ -ray yields that are measured, as opposed to absolute cross sections, and the relative corrections for states which lie close in energy are of similar magnitude [Kav95]. Another difference between semi-classical calculations and fully quantal are the already mentioned Coulomb-nuclear interference effects, which are of particular relevance in Coulomb excitation experiments involving light nuclei. These two sources of systematic uncertainty in the GOSIA analysis are relevant to the present experiment and have been investigated. The outcome of this analysis can be found in Chapter 4, sections 4.3 and 4.4.

Other potential sources of systematic error include, but are not limited to, virtual excitation of unobserved states, mutual excitation of projectile and target, and uncertainties derived from the experiment, such as energy loss of ions in the target (i.e. target thickness), beam energy, detector efficiency, etc. These will all be considered and investigated as part of Chapter 4.

Finally, the angular distribution of the de-excitation γ rays can be attenuated by the hyperfine interaction between the nucleus and the atomic magnetic field, this is known as the de-orientation effect. This attenuation is estimated by means of phenomenological models for the hyperfine interaction, where attenuation coefficients G_k are introduced to correct the angular distribution of the de-excitation γ rays. This is implemented in GOSIA by using the two-state model of Brenn and Spehl [Bre77], which was tested by performing a model-independent analysis of available data on the attenuation coefficients [Kav89]. This study resulted in both the coeffi-

cients G_2 and G_4 being well reproduced, and the uncertainties in the model having a negligible influence in the extracted $E2$ matrix elements [Kav95]. In addition, γ -ray detector arrays covering a large fraction of the solid angle will make this effect average over the γ -ray angular distribution, further reducing its impact on the measured cross sections [Czo83].

Chapter 3

Experimental set-up

A Coulomb excitation experiment was performed in order to measure the quadrupole moment $Q(2_1^+)$ via the reorientation technique. In this chapter, a description of the set-up used during the experiment will be presented. The beam, targets, detection systems, calibrations, and the DAQ system and electronics used in the J22 experiment will be discussed.

3.1 The experiment: beam and targets

The experiment was conducted at the Accelerator Laboratory of the University of Jyväskylä, Finland, in Spring 2017. The JYFL accelerator laboratory is equipped with three large-scale accelerators: the K130 cyclotron, MCC30/15 cyclotron and the 1.7 MV Pelletron. The K130 is an isochronous cyclotron equipped with three external electron cyclotron resonance (ECR) ion sources and a multicusp light-ion source, which can deliver a large variety of heavy- and light-ion beams up to the energy of $130 \text{ Q}^2/\text{A MeV}$ for use in research and applications [Liu89, Hei01].

The K130 cyclotron was used to accelerate the ions produced by the ECR source, and a $^{12}\text{C}^{4+}$ ion beam at an energy of 47.65 MeV and intensities ranging between 40 - 320 enA was produced. The energy of the beam was measured with a precision of 0.1% and the spread in the beam energy distribution was of 1%.

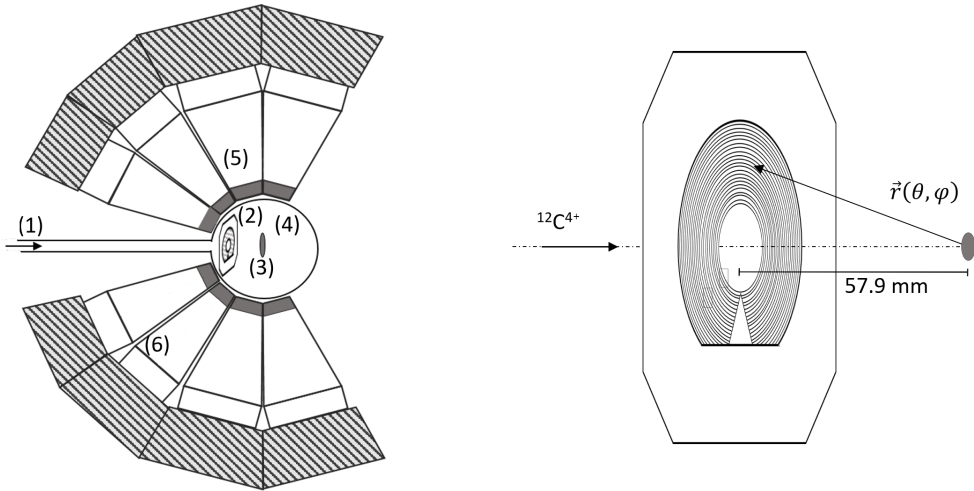


Figure 3.1: Sketch of the experimental set-up outside (left) and inside (right) the vacuum chamber. On the left side, the (1) $^{12}\text{C}^{4+}$ beam, (2) SiCD (S2-type) detector, (3) target, (4) scattering chamber, a (5) Clover detector and a (6) Phase1 detector are indicated.

The 47.65 MeV $^{12}\text{C}^{4+}$ ion beam delivered by the K130 cyclotron was used to bombard a ^{208}Pb target Coulomb-exciting both of projectile and target. The subsequent de-exciting γ -rays following the population of excited states in the ^{12}C projectile and in the ^{208}Pb target were measured using the JUROGAMII array. A double-sided silicon CD-type detector (Micron S2), was used to detect backward-scattered ^{12}C particles in coincidence with the γ -rays (see Figure 3.1).

A set of 7 different ^{208}Pb targets (99.0% enriched) were used throughout the experiment. All targets included a $40 \mu\text{g}/\text{cm}^2$ ^{12}C backing, and their thicknesses ranged from 294 to $314 \mu\text{g}/\text{cm}^2$ (Table 3.1). The thickness of the target was chosen so that the systematic uncertainty arising from the energy straggling of the accelerated ^{12}C inside the ^{208}Pb target was minimised since the uncertainty in the beam energy has a direct impact on the final precision with which the $Q(2_1^+)$ is extracted.

Figure 3.2 shows a photo of the experimental set-up; on the left side the target chamber with half of the JUROGAMII detectors surrounding it, and on the right side, the inside of the target chamber containing the SiCD detector and target. A protecting mask was placed in front of the SiCD detector in order to avoid it being damaged by the beam. The target chamber was custom designed to fit the SiCD

Table 3.1: Targets sizes and thicknesses used for the experiment.

Diameter (mm)	^{12}C thickness ($\mu\text{g}/\text{cm}^2$)	^{208}Pb thickness ($\mu\text{g}/\text{cm}^2$)
15	38	297
15	39	289
15	40	291
15	41	297
20	39	307
20	40	311
20	39	314

detector and target holder for this experiment.

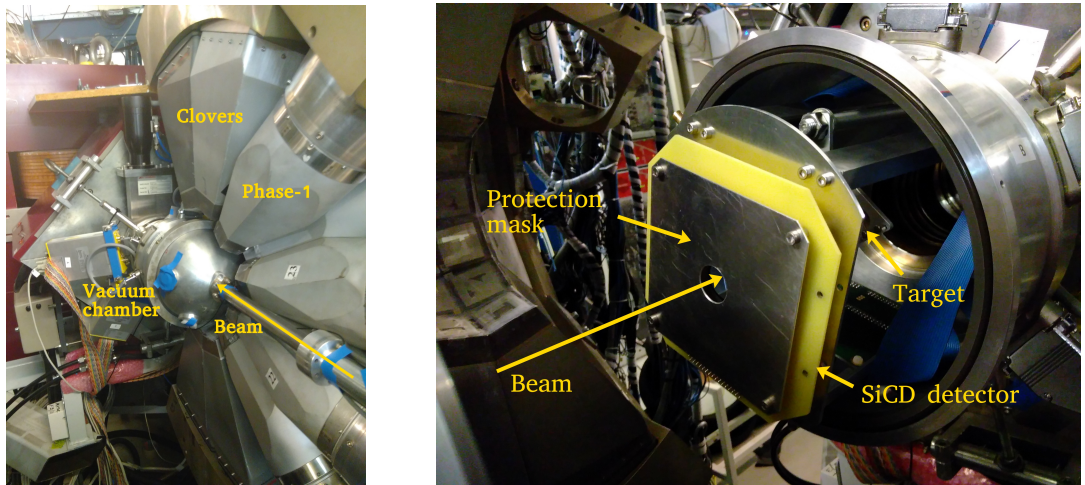


Figure 3.2: Photos of the experimental set-up taken during the experiment: outside view of the vacuum chamber and half of the JUROGAMII HPGe detectors (left) and view of the interior of the vacuum chamber (right).

3.2 JurogamII

JUROGAMII is a γ -ray spectrometer consisting of an array of 39 detector modules, each of which consists of a high-purity Germanium detector (HPGe) and a Compton-suppression Bismuth Germinate shield (BGO). Technical details of the array can be found in the recent review paper of its successor JUROGAM3 [Pak20].

Of the 39 detectors in the JUROGAMII array, 15 are Eurogam Phase1 detectors and 24 are Clover detectors. The Eurogam Phase1 (Figure 3.4) are large coaxial n-

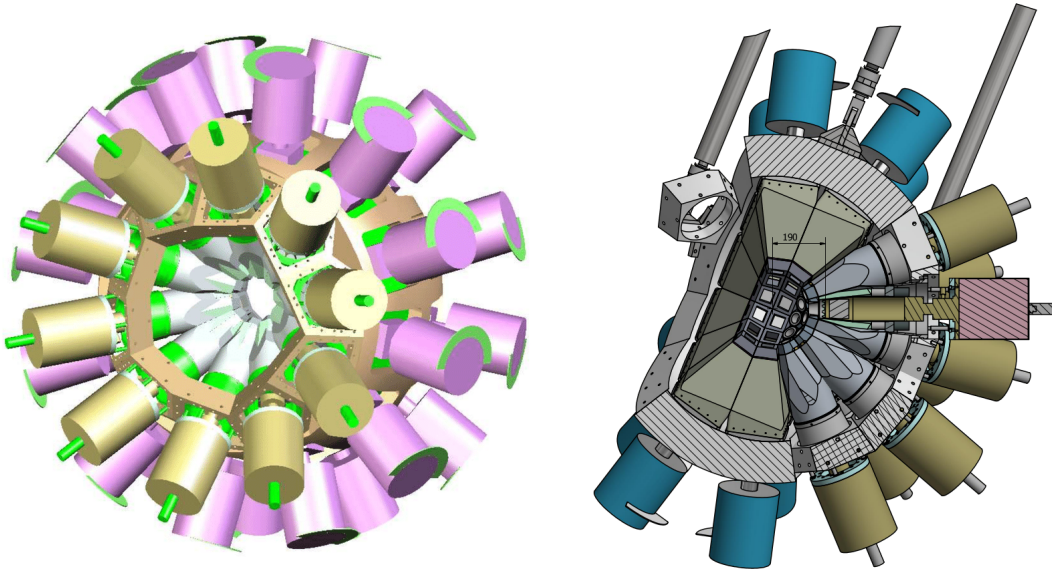


Figure 3.3: 3D representation of the JUROGAMII array (left) and transverse view of the inside (right) [Sic13].

type HPGe detectors [Bea92]. The Clover detectors consist of four smaller coaxial n-type HPGe crystals [Duc99]. The measured γ -ray energy in the Clovers can be added up (add-back mode) on an event by event basis in order to maximise photopeak efficiency and improve the peak-to-background ratio, especially for high energy γ rays. The different angles covered by JUROGAMII are included in Table 3.2 and a 3D representation of the detectors is shown in Figure 3.3.

In addition, each module is equipped with a heavy-metal collimator to prevent γ rays from the target hitting the BGO shields directly. The BGOs act as anti-coincidence detectors and they are used to improve the peak-to-background ratio of the γ -ray spectrum. As such, if there is a signal in the detector in coincidence with a BGO signal, the event will be discarded since it would be coming from a Compton scattered γ -ray and not a full energy deposition in the crystal.

All of the detector crystals need to be operated at very low temperatures. Typically, the crystal is cooled down to approximately 90 K by using liquid Nitrogen (LN_2) [Pak05]. This low temperature is maintained by means of a cold finger providing a heat contact with the LN_2 , which is stored in a thermally isolated dewar. Figure 3.4 shows a schematic of all the different parts inside a Phase1 module,

Table 3.2: JUROGAMII array specifications. (a) T is Phase1 detector and Q is Clover detector. (b) θ is the polar angle, defined with respect to the beam direction. (c) ϕ is the azimuthal angle, defined as vertically upwards and increases in a clockwise direction when the array is viewed from a position upstream. All angles are midpoint angles.

Ring #	Array position ^(a)	θ° ^(b)	ϕ° ^(c)
1	T1	157.6	0
1	T2	157.6	72
1	T3	157.6	144
1	T4	157.6	216
1	T5	157.6	288
2	T6	133.57	18
2	T7	133.57	54
2	T8	133.57	90
2	T9	133.57	126
2	T10	133.57	162
2	T11	133.57	198
2	T12	133.57	234
2	T13	133.57	270
2	T14	133.57	306
2	T15	133.57	342
3	Q1	104.5	15
3	Q2	104.5	45
3	Q3	104.5	75
3	Q4	104.5	105
3	Q5	104.5	135
3	Q6	104.5	165
3	Q7	104.5	195
3	Q8	104.5	225
3	Q9	104.5	255
3	Q10	104.5	285
3	Q11	104.5	315
3	Q12	104.5	345
4	Q13	75.5	15
4	Q14	75.5	45
4	Q15	75.5	75
4	Q16	75.5	105
4	Q17	75.5	135
4	Q18	75.5	165
4	Q19	75.5	195
4	Q20	75.5	225
4	Q21	75.5	255
4	Q22	75.5	285
4	Q23	75.5	315
4	Q24	75.5	345

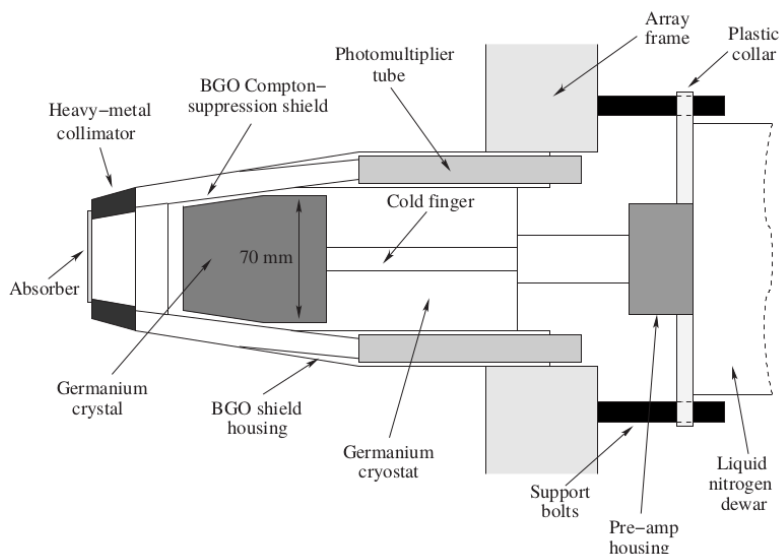


Figure 3.4: Technical and schematic drawing of a Phase1 Eurogam detector module [Nol94, Pak05].

including the collimator, crystal, BGO shielding, cold finger and dewar.

3.2.1 Add-back

As it was previously mentioned, each of the JUROGAMII Clovers consists of 4 smaller crystals. Through Compton scattering, a γ ray may interact with two or more crystals within a Clover, resulting in the energy deposited by the γ ray being shared by the crystals. These type of events can be “added-back”, and the energy in each of the crystals added together to determine the energy of the incident γ ray. By way of example, Figure 3.5 illustrates how an incident photon may hit one, two or three crystals before being absorbed.

The add-back is carried out at a later stage through software analysis, where the sorting code adds up the deposited energy in simultaneous events within the different crystals of a certain Clover. The add-back results in an improvement of the peak-to-background ratio of the γ -ray spectra, since it reduces the number of events from the Compton part of the spectrum and adds them to the photopeak. Figure 3.6 shows a γ -ray spectra for the ^{66}Ga calibration source (see section 3.2.2)

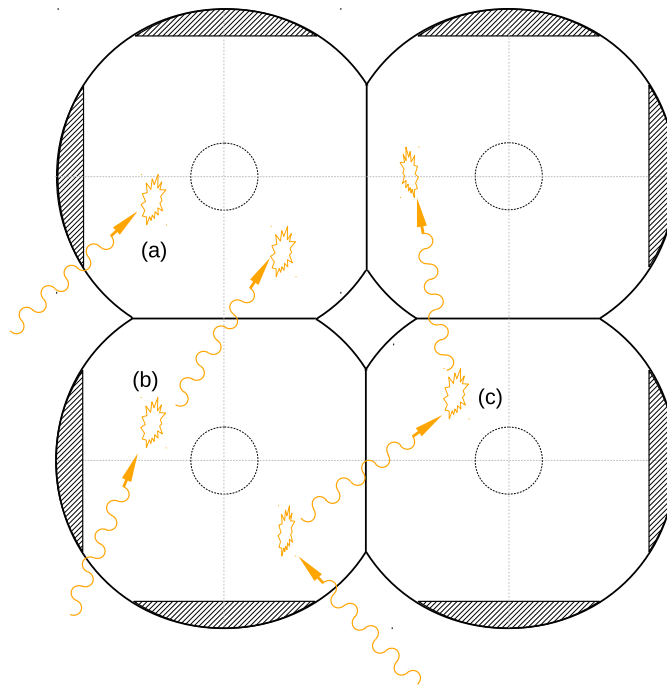


Figure 3.5: Sketch of the four crystals inside a Clover detector in the JUROGAMII array. As an example, the events were there is one (a), two (b) or three (c) hits of the incident γ ray is shown.

obtained with the JUROGAMII Clovers with and without this add-back feature.

The improvement in the peak-to-background ratio is more pronounced as the probability of photoabsorption decreases and the probability of Compton scattering increases with the incident photon energy, meaning that the effect of the add-back is more noticeable for higher energy γ rays. Figure 3.7 shows the ratio between the photopeak efficiency of the JUROGAMII Clovers (rings 3 and 4) with and without add-back. The γ rays measured in the present work range from 2.6 MeV to 4.4 MeV, for which the add-back provides an improvement in the photopeak efficiency in the Clovers of a factor (add-back factor in Figure 3.6) of ~ 1.7 and ~ 1.85 respectively. This shows how the add-back is a very useful tool to improve the statistics in the photopeaks of the Clover detectors, especially when measuring high-energy γ rays, as is the case in the present experiment.

In general, the Phase1 detectors are larger than the Clovers. The Clover detectors provide a better energy resolution since the smaller crystals within each detector

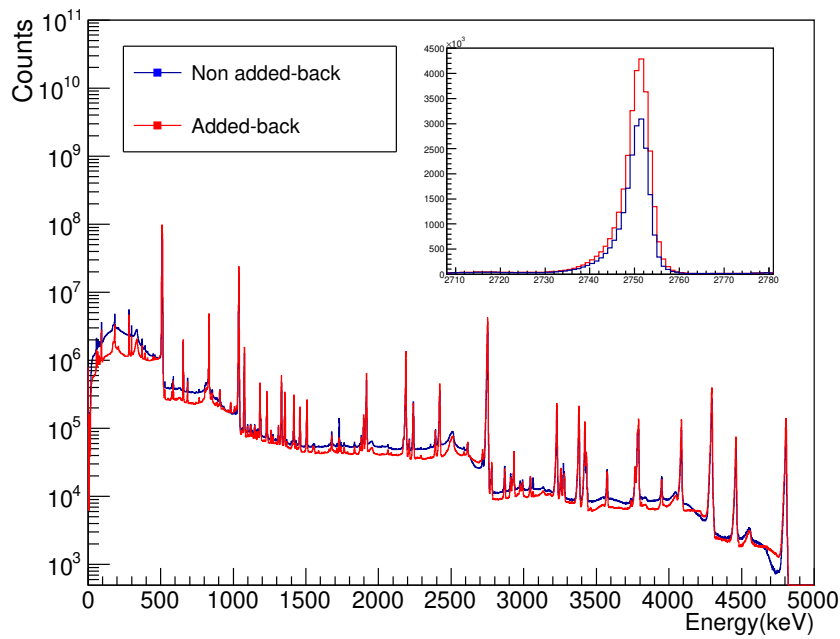


Figure 3.6: Energy calibrated ^{66}Ga γ -ray spectrum obtained with the JURAMII Clovers with and without the add-back mode. As an example, a zoomed-in photopeak of ^{66}Ga source is displayed.

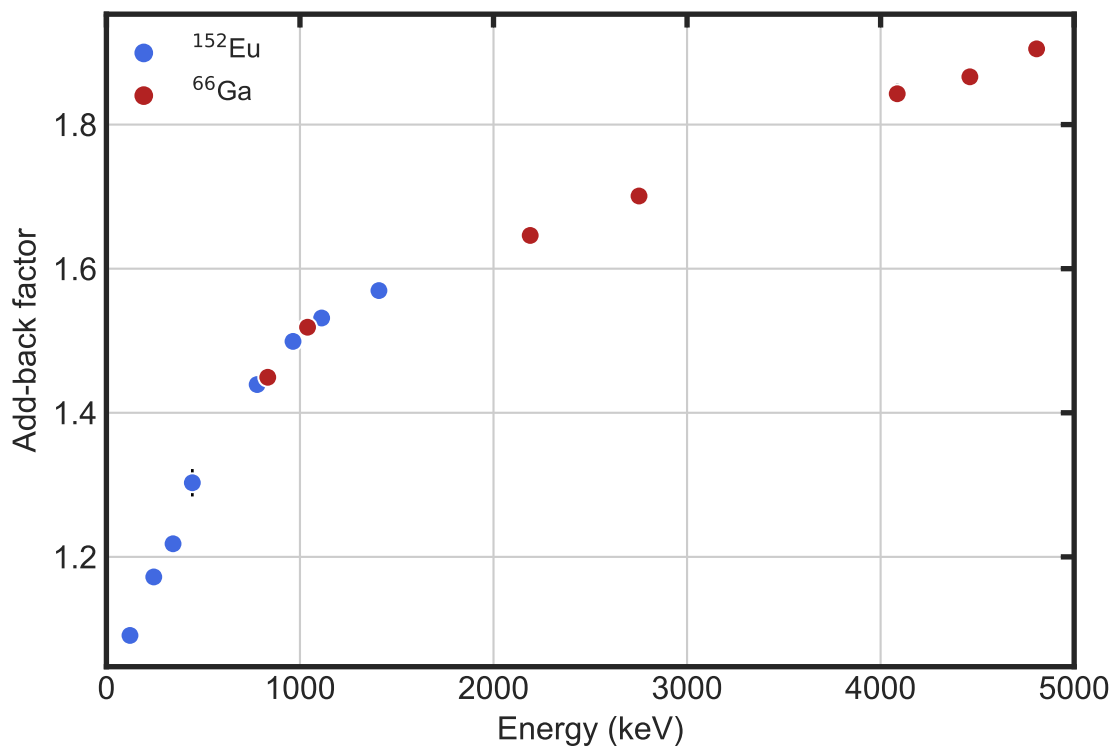


Figure 3.7: Add-back factor measured for the different γ -ray transitions in the ^{152}Eu and ^{66}Ga source measurements.

module give a more accurate position of interaction of the γ -ray with respect to the emitting source, which translates into a smaller Doppler broadening. For the case of added-back events, due to the small time resolution that would be required, it is not possible to determine in which crystal of the Clover the γ -ray deposited energy first — which is the position to be used for the Doppler correction. However, high-energy γ rays have a higher probability of Compton scattering at angles of $\sim 90^\circ$ [Kle29], which corresponds to an energy deposition of half the incident energy of the photon according to the Compton scattering formula [Com23]. Therefore, the crystal with the highest energy deposition was considered as the first interaction point for the Doppler correction. In section 4.1.1, the Doppler correction used for the analysis will be discussed in further detail.

3.2.2 Energy and efficiency calibrations: the ^{66}Ga source

The energy and efficiency calibrations were performed using EuBa and ^{66}Ga sources. The EuBa is a standard calibration source for γ -ray detectors. ^{133}Ba emits γ rays ranging from 80 keV to 384 keV [Rab95] and ^{152}Eu covers the range from 122 keV to 1408 keV [AC96]. However, for experiments where high-energy γ rays are measured (>2 MeV), the use of traditional calibration sources like these becomes insufficient, as they only cover up to ~ 2 MeV, and result in inaccurate extrapolations in the energy and relative efficiency calibration curves, leading to larger systematic uncertainties.

As such, ^{66}Ga becomes an excellent source for high-energy γ -ray calibration, since the emission probabilities for up to 18 strong lines, from 834 to 4806 keV, are known to better than 1% accuracy for this radionuclide (Table 3.3) [Bag02]. The ^{66}Ga source was produced with a 11 MeV proton beam on a $^{\text{nat}}\text{Zn}$ target via the $^{\text{nat}}\text{Zn}(p,xn)^{66}\text{Ga}$ channels. As previously mentioned, using this radioisotope avoided using an inappropriate efficiency curve extrapolation, which is necessary with conventional radioactive sources for calibration at high γ -ray energies. The energy calibration as well as the efficiency calibration was performed for each Phase1

Table 3.3: ^{66}Ga decay recommended relative γ intensities [Bag02].

E_γ (keV)	I_γ
833.5324(21)	15.930(50)
1039.220(3)	100.0(3)
1333.112(5)	3.175(12)
1418.754(5)	1.657(8)
1508.158(7)	1.497(7)
1898.823(8)	1.051(8)
1918.329(5)	5.368(21)
2189.616(6)	14.420(50)
2422.525(7)	5.085(22)
2751.835(5)	61.35(23)
3228.800(6)	4.082(19)
3380.850(6)	3.960(19)
3422.040(8)	2.314(14)
3791.036(8)	2.941(19)
4085.853(9)	3.445(18)
4295.224(10)	10.300(80)
4461.202(9)	2.260(30)
4806.007(9)	5.030(30)

detector and each Clover crystal separately, making use of the add-back mode for the Clover detectors.

The output signals of each Phase1 and Clover are proportional to the deposited energy by the detected γ ray. Equation 3.1 was used to relate the channel number of the ADC (see section 3.4 for an explanation of the data acquisition system) into the energy (E) of the known emitted γ -ray of each of the calibration sources in units of keV,

$$E = p_0 + p_1 \cdot x + p_2 \cdot x^2, \quad (3.1)$$

where p_0 , p_1 , and p_2 are the fitting parameters and x is the channel number. Figure 3.8 shows the total calibrated γ -ray energy spectra of the produced ^{66}Ga calibration source measured with the whole JUROGAMII array. The γ -ray transitions used for the energy and efficiency calibration are labelled in the figure.

Furthermore, the experiment presented in this work involves the relative measurement of the Coulomb excitation cross section of the first 2_1^+ state in ^{12}C , at 4439

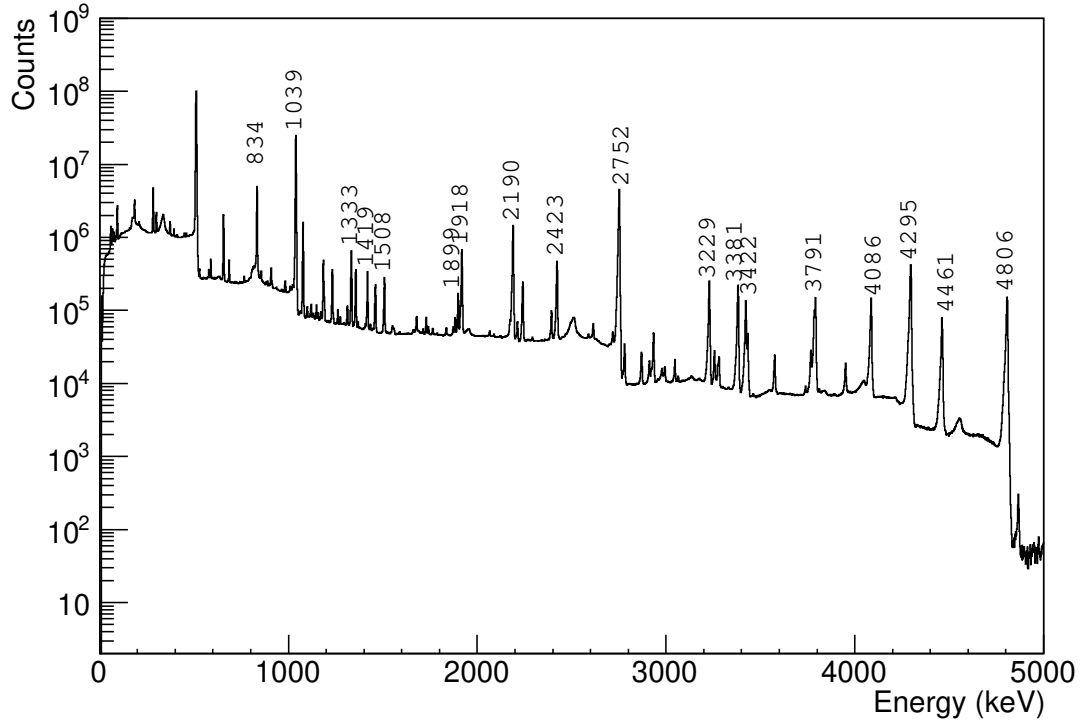


Figure 3.8: Total γ -ray energy spectra of the produced ^{66}Ga calibration source measured with the whole JUROGAMII array using add-back.

keV, with respect to the excitation cross section of the 3_1^- state, at 2614 keV in ^{208}Pb . This requires a relative efficiency calibration between both γ -ray transitions. As shown in Table 3.3, the ^{66}Ga source provides calibration points next to each γ -ray transition energy of interest. The relative efficiency for each of the detectors at each energy ε_{rel} was obtained by fitting the γ -ray peaks of the spectra to a Gaussian distribution and integrating it. The obtained number of counts was then corrected by their relative intensity

$$\#\text{corrected counts} = \frac{\text{counts}}{I_\gamma/100}, \quad (3.2)$$

and arbitrarily normalising it to one of the transitions, the 1039 keV in this case,

$$\varepsilon_{\text{rel}} = \frac{\#\text{ corrected counts}}{\#\text{corrected counts at 1039 keV}} = \frac{\#\text{ counts}}{\#\text{ counts at 1039 keV}} \cdot \frac{I_\gamma^{1039 \text{ keV}}}{I_\gamma}. \quad (3.3)$$

For wide energy ranges like this case, one commonly used formula to fit the experimental relative efficiencies is a polynomial function relating the logarithm of the efficiency to the logarithm of the energy [Kno89],

$$\log \varepsilon(E) = \sum_{i=1}^5 a_i \left(\log \frac{E}{E_0} \right)^{i-1} \quad (3.4)$$

where E_0 is a fixed reference energy and the values of a_i are the fitted parameters to the efficiencies. The obtention of the experimental efficiencies and the fit to equation 3.4 was performed independently for each one of the 15 Phase1 and 24 Clover detectors obtaining 39 set of parameters, each of which define the efficiency curve for each of the detector modules. These sets of parameters will be used as part of the GOSIA input for the extraction of the matrix elements in a later stage of the analysis (see section 4.4). Figure 3.9 shows the obtained total experimental relative efficiencies for the used γ -ray transitions in the EuBa and ^{66}Ga source, together with the curve fit using equation 3.4 for the entire of the JUROGAMII array. The displayed experimental data points include the uncertainty in the number of counts, statistical uncertainty and the error arising from the fit, and the propagated uncertainty for each γ -ray transition intensity.

During the experiment, γ -ray transitions coming from the 2_1^+ in ^{12}C at 4439 keV and, 3_1^- and 2_1^+ in ^{208}Pb at 2614 and 4085 keV respectively were observed. The ^{66}Ga calibration source used provided calibration points at 2752, 4086 and 4461 keV. It can be noted from Figure 3.9, the high-statistics in the ^{66}Ga γ -ray spectra recorded with the whole JUROGAMII array translated into highly accurate calibration points at these energies. For instance, the fitted total efficiency at 4439 keV relative to the 1039 keV transition in ^{66}Ga was found to be $\varepsilon_{rel} = 0.3124(18)$. As shown, the systematic uncertainty to be propagated to the extracted γ -ray yields (see section 4.2) was below 1% and thus considered negligible.

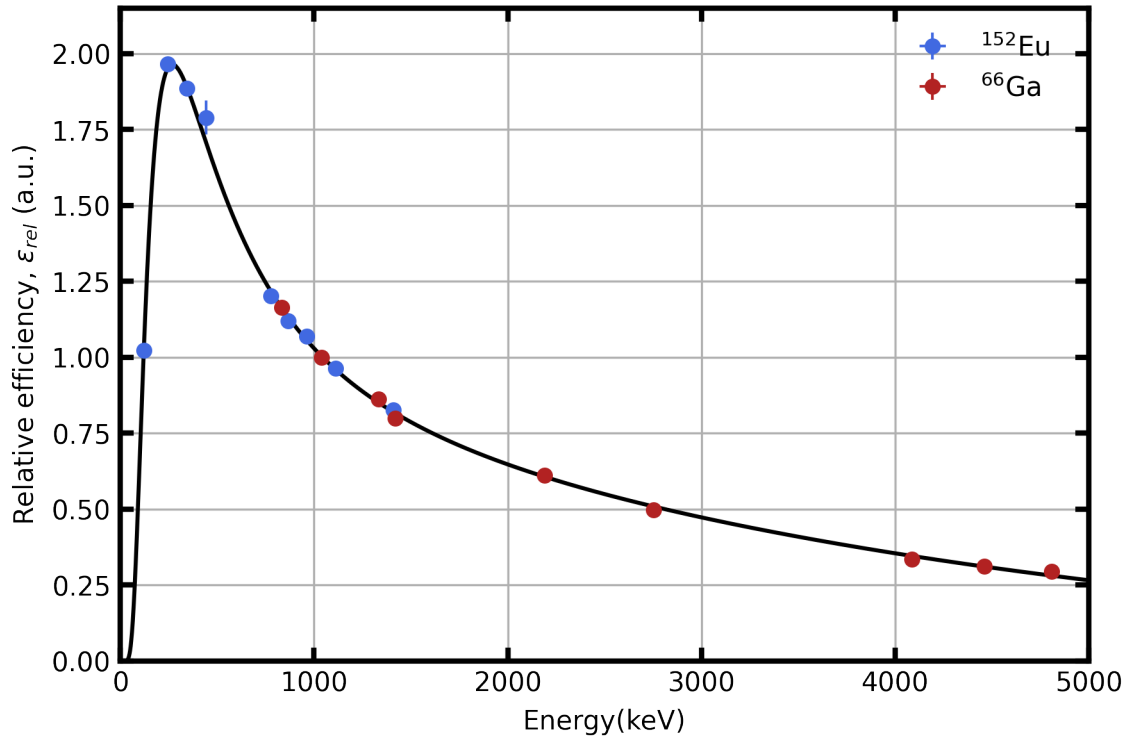


Figure 3.9: Experimental total efficiencies for each of the used γ -ray transitions in the EuBa and ^{66}Ga source, and curve fit (equation 3.4) for the whole JUROGAMII array (Phase1 and Clover detectors using add-back) relative to the 1039 keV transition in ^{66}Ga .

3.2.3 Neutron damage

The near perfection of the crystalline lattice is the key factor for the correct performance of any semiconductor detector. Defects in this lattice induced by any sort of radiation damage can lead to the trapping of charge carriers and incomplete charge collection. HPGGe semiconductor detectors used for γ -ray spectroscopy are sensitive to radiation damage due to their large volume and long charge collection paths [Kno89]. Radiation damage on HPGGe detectors can often be caused by the exposure to neutrons coming from the different reaction mechanisms taking place during an experiment. This was the case for the JUROGAMII array, where the HPGGe detectors suffered from neutron damage caused in experiments using this array at the Accelerator Laboratory of the University of Jyväskylä prior to the experiment described in this work.

Fast neutrons can produce the so called Frenkel defects, which are displacements of atoms of the lattice from their normal lattice site. The displaced atoms, now at an interstitial position, together with the vacancy ('hole') that they left behind become a trapping site for normal charge carriers. In addition, more complex 'clusters' of crystalline damage produced along the track of a primarily displaced atom with sufficient energy are also produced.

These types of defects caused by neutron damage increase the amount of hole trapping within the active volume of a detector. As a result, some of the pulses produced by the active material will be subjected to a partial charge loss which will vary from one to another. The measured peaks in the pulse height spectrum, i.e. the energy spectrum, will then show a tailing towards the low-energy side [Kno89]. This effect was observed in the measured γ -ray spectra during the experiment and the low-energy tail observed was included in the fitting and integrating procedures performed during the analysis of the spectra. Figure 3.10 shows an example of the 2751 keV peak in ^{66}Ga presenting different low-energy tails arising from neutron damage for different Phase1 detectors. The observed neutron damage varied for each detector and for each peak.

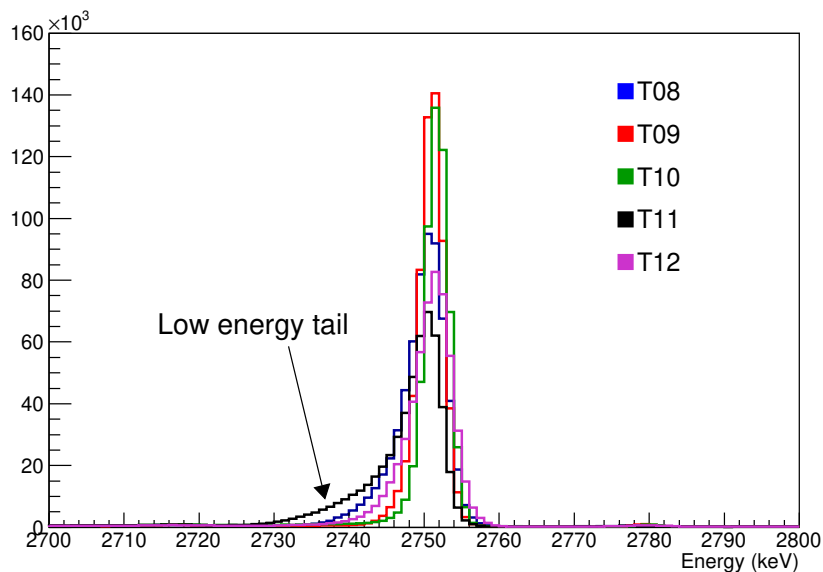


Figure 3.10: Comparison of low-energy tail arising from neutron damage observed for the 2751 keV γ -ray transition in ^{66}Ga for different Phase1 detectors.

3.3 SiCD

The double-sided CD-type silicon detector (S2 type) is a position sensitive particle detector made of n-type based Silicon and segmented into 48 rings on one side, giving the θ coordinate of the detected particle, and 16 sectors providing the ϕ coordinate. The detector contains a hole of inner radius equal to 11.52 mm and outer radius of 35.00 mm, which gives the detector a total sensitive area of approximately 3.43 cm². Each concentric ring is 0.39 mm wide and therefore provides a good position resolution for superior Doppler corrections. As illustrated in Figure 3.11, the S2-type detector is not perfectly axially symmetrical, as it has a non-sensitive area in some of the rings and sectors.

The detector was placed at backward-scattering angles at a distance of 57.9 mm which provides an angular coverage of 149.0° to 168.6°, with a position resolution of 0.4° in the θ coordinate of the scattered particle. The exact angle θ for each corresponding ring can be calculated using the SiCD position, the inner radius of the SiCD, the width of each ring, and simple trigonometry.

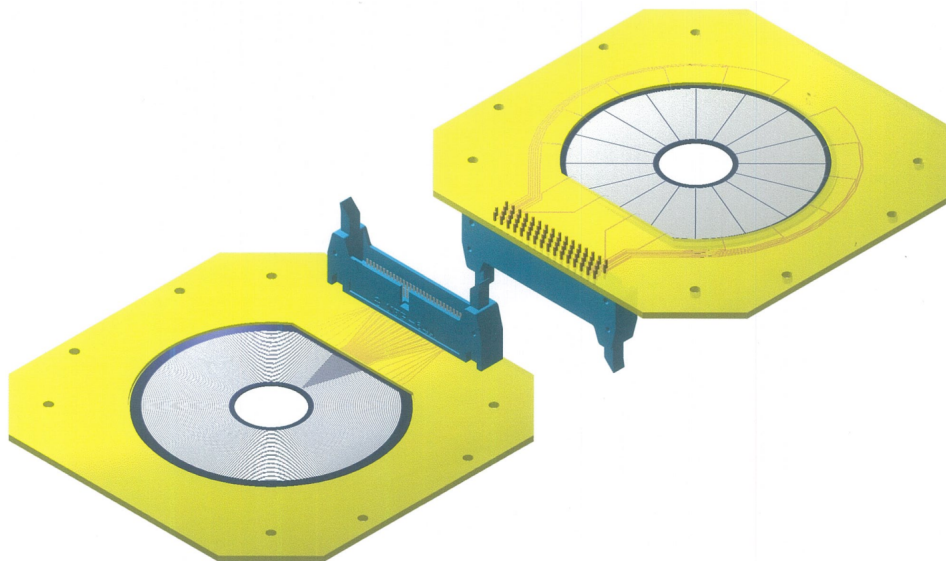


Figure 3.11: 3D design of the SiCD (S2 type) detector manufactured by Micron Semiconductor Ltd.

3.3.1 Energy calibration

The SiCD detector was calibrated using a triple α source containing ^{239}Pu , ^{241}Am and ^{244}Cm , together with higher-energy calibration points provided by the elastically scattered ^{12}C particles. The triple α source emits α particles at energies of around 5 MeV. Table 3.4 shows the emitted α particle energies for each of the isotopes. The energy of the elastically scattered ^{12}C was measured for each scattering angle, i.e. each ring, with the SiCD detector. A polynomial fit was used to obtain the energy-channel relation between known α particle energies and the calculated scattering energies of the ^{12}C ions, and the measured α particles and the detected elastically scattered ^{12}C channel numbers. Figure 3.12 illustrates the second-order polynomial fit performed for sector 3 as an example of the above.

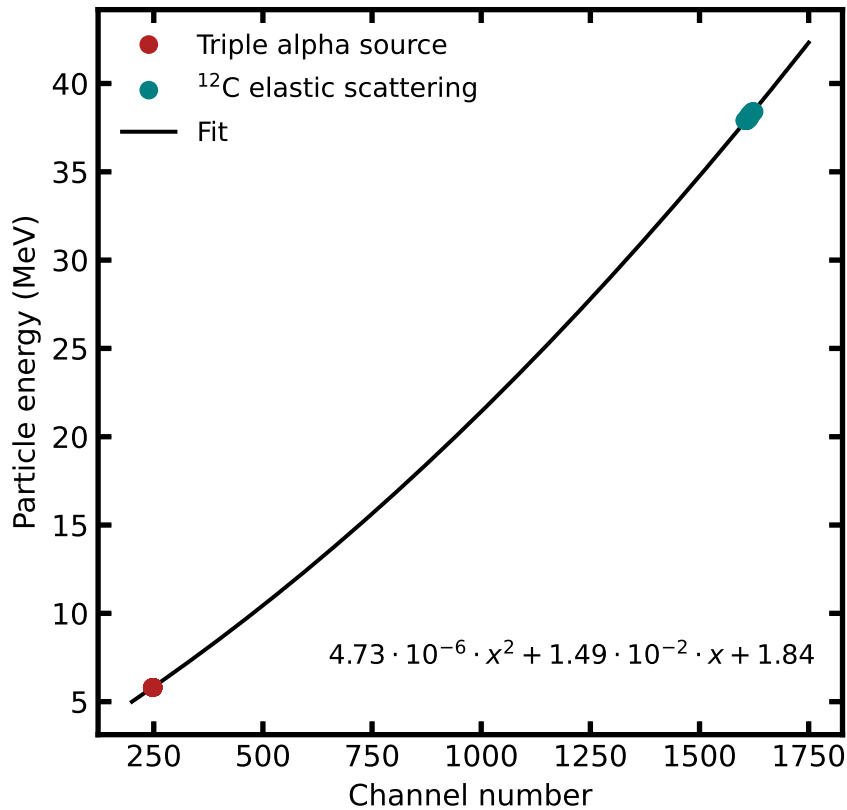


Figure 3.12: Second-order polynomial fit performed for the calibration of sector 3 in the SiCD detector. The calibration points from the triple alpha source as well as the ^{12}C elastic-scattering energies are indicated. Plot changed

Figure 3.13 shows an example of the calibrated particle energy spectra of the detected ^{12}C measured by one ring (ring 20), when a second hit has taken place in a certain sector (sector 5), and one sector (sector 5), when a first hit took place in a certain ring (ring 20). The largest peak shown in the spectra corresponds to the detected elastically scattered ^{12}C particles. If the detector is properly calibrated, the energy measured by a certain ring should be the same as the one measured by the sector for the same scattering angle. As demonstrated, the energy calibration between rings and sectors is consistent.

Table 3.4: Emitted alpha particle energies for the triple α source, ^{239}Pu , ^{241}Am and ^{244}Cm .

^{239}Pu (MeV)	^{241}Am (MeV)	^{244}Cm (MeV)
5.105	5.388	5.763
5.143	5.443	5.805

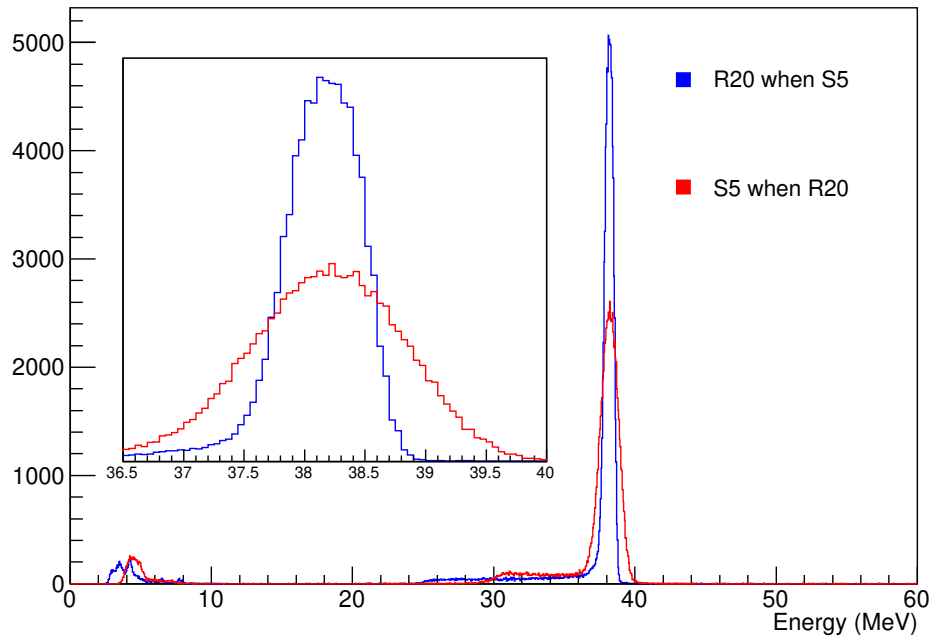


Figure 3.13: Calibrated particle energy spectra of the detected ^{12}C measured by one ring (ring 20), when a second hit has taken place in a certain sector (sector 5), and one sector (sector 5), when a first hit took place at a certain ring (ring 20).

3.4 Data Acquisition

More conventional data acquisition systems (DAQ) experience a common dead-time where a trigger condition and a time gate are defined. Experiments which use such DAQ systems are often limited by dead-time. Conversely, in this setup, we used a Total Data Readout (TDR) technique which eliminates the need for a common dead-time condition by recording all data from the individual channels at an accuracy of 10 ns [Laz01]. The TDR technique is triggerless and minimises the dead-time of the system, since this dead-time is now limited to individual detector components.

The signal from all the detectors are converted and time stamped using shaping amplifiers (NIM/CAMAC units) and constant fraction discriminators (CFDs). The conversion and readout of the signals is performed by an ADC card (VXI-D format) offering 32 independent channels (14 bits with sliding-scale correction and zero suppression) [Laz01]. The timestamping requires the distribution and synchronisation of a 100-MHz clock. A Metronome (VME module) controls the clock distribution and maintains synchronisation of all the ADCs. An additional VME module provides a method to include hit patterns in the data stream along with a timestamp.

The data items from all ADCs and pattern cards are then sent to buffering and becomes ready for use by the event builder. Subsequently the data is then sent to tape. Figure 3.14 is a schematic diagram of the described DAQ system and electronics.

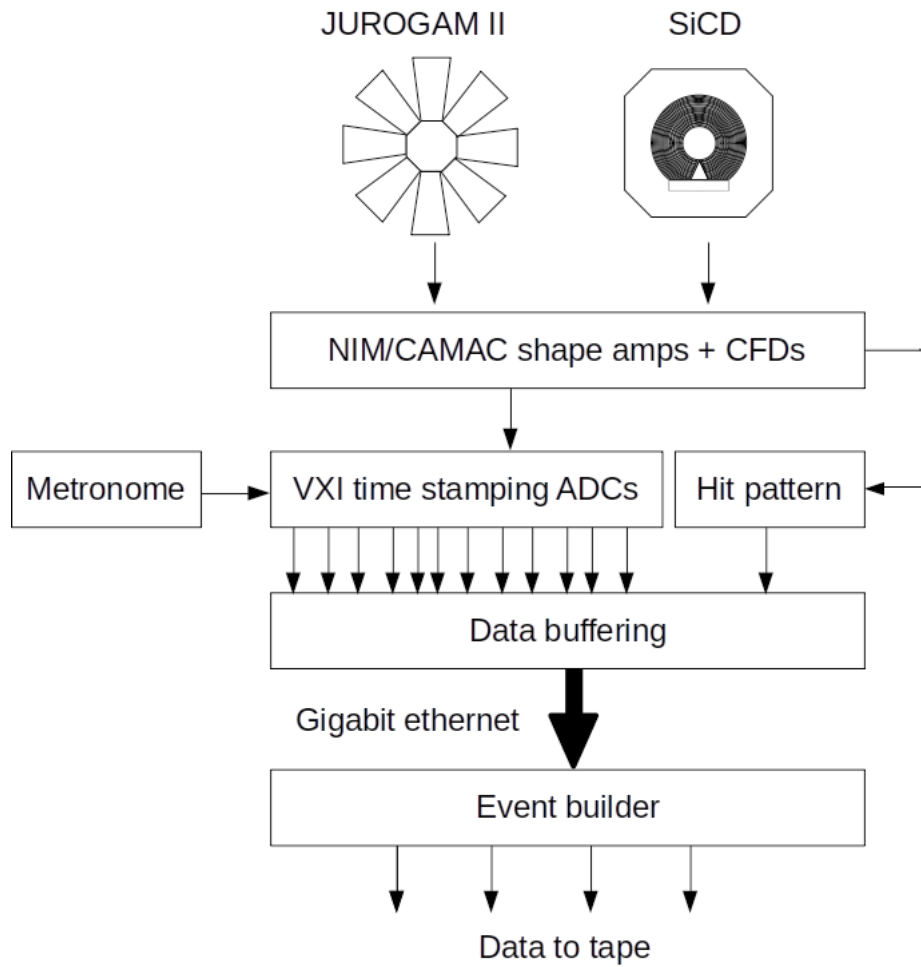


Figure 3.14: Schematic diagram of the DAQ system and electronics (TDR technique), adapted from [Laz01].

Chapter 4

Data Analysis and Results

The following chapter describes the sorting, analysis process and results of the Coulomb excitation experiment of ^{12}C . First, the sorting of the data, Doppler correction, time and particle-energy gates and analysis of the obtained γ -ray spectra will be discussed. The presence of Coulomb-nuclear interference will subsequently be investigated, and finally the GOSIA analysis and results will be presented.

4.1 Sorting of the raw data

The java-based software package GRAIN [Rah08] was used to sort the raw TDR data stream and produce the different histograms that were later analysed with the ROOT data analysis framework [Ant09]. GRAIN can be used to form physically meaningful events from the data stream and its sorting code can be modified to extract physical results through the production of histograms that can be visualised through a simple graphical user interface (GUI).

Despite the TDR data acquisition system being triggerless and all the electronic channels operating individually in free running singles mode, a particle- γ coincidence condition was set in GRAIN in order to extract the desired Coulomb excitation events. For every backward-scattered ^{12}C ion detected by the SiCD detector, the coincident γ rays within a $1\ \mu\text{s}$ time window, ($0.5\ \mu\text{s}$ before and $0.5\ \mu\text{s}$ after each

hit in the SiCD), were grouped as an event. This delayed trigger of $0.5 \mu\text{s}$ is introduced in GRAIN through a configuration file, where additional options regarding the pile-up or BGO Compton suppression can be added for the different channels. Another file was produced containing the parameters obtained for the calibration of JUROGAMII (section 3.2.2) detector modules and the SiCD rings and sectors (section 3.3.1). Consequently, GRAIN will read both of these files producing the desired event structure with correctly calibrated particle and γ -ray energies.

The java-based sortcode can later be modified to include the Doppler corrections, more accurate time gates (prompt and background) and particle-energy gates.

4.1.1 Doppler correction

For every event, the velocity of the backward-scattered ^{12}C and the ^{208}Pb recoiled can be calculated for each scattering angle (each ring) using relativistic scattering kinematics. The calculated velocities for ^{12}C and the recoiled ^{208}Pb nucleus are of $\beta \sim 0.08c$ and $\beta \sim 0.01c$, respectively. At these speeds, a substantial Doppler shift of the measured γ rays takes place. During the sorting of the data, these Doppler-shifted measured γ -ray energies were corrected on an event-by-event basis using the expression

$$E_{\gamma,i} = E_{\text{meas}} \frac{1 - \beta_i \cos \alpha_{\gamma,i}}{\sqrt{1 - \beta_i^2}} \quad (i = \text{C, Pb}), \quad (4.1)$$

where $\beta_i = v_i/c$, and v_i is the speed of the projectile (or target) before emitting the γ ray and,

$$\cos \alpha_{\gamma,i} = \sin \theta_{\gamma}^{\text{JG}} \sin \theta_i^{\text{S2}} \cos (\varphi_{\gamma}^{\text{JG}} - \varphi_i^{\text{S2}}) + \cos \theta_{\gamma}^{\text{JG}} \cos \theta_i^{\text{S2}} \quad (i = \text{C, Pb}), \quad (4.2)$$

where $\alpha_{\gamma,i}$ is the angle between the scattered particle and the γ ray, $\theta_{\gamma}^{\text{JG}}$ and $\varphi_{\gamma}^{\text{JG}}$ correspond to the angles of the JUROGAMII modules which detected the γ ray (table 3.2), and θ_i^{S2} and φ_i^{S2} are the angles that define the position of the scattered ^{12}C or ^{208}Pb which are given by the SiCD detector. Here, ^{12}C is the only detected particle

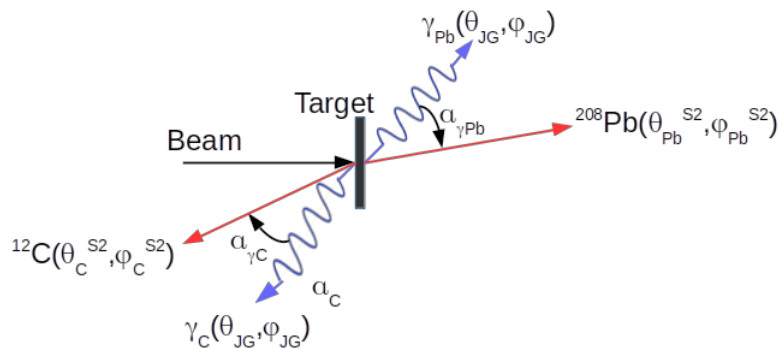


Figure 4.1: Scheme of the inelastic-scattering process where the angle between the emitted γ ray and each nuclei can be expressed as a function of the JURROGAMII and the S2 SiCD detector angles, see Eq. (4.2.)

but the corresponding angle for ^{208}Pb can be calculated via kinematics. A scheme of this is shown in Figure 4.1. For the Doppler correction in the clovers, the total energy deposited by the γ ray in each clover crystal was taken into consideration (add-back mode), however, the angle of the crystal in which more energy was deposited was the one used for the correction.

The β_i values were calculated for each scattering angle θ (each ring) using inelastic-scattering kinematics, providing a set of 48 values for both target and projectile. Due to the difference in mass between projectile and target, the lighter particle will recoil with a much larger β , and therefore the γ ray emitted by the ^{12}C will have a more severe Doppler shift, which makes the Doppler correction highly sensitive to the chosen set of β_i values.

The decay process after the population of the excited states via Coulomb excitation occurs almost instantly (42.2 fs [Kel17] for the 2_1^+ in ^{12}C and 16.7 ps [Mar07] for the 3_1^- in ^{208}Pb) and therefore it takes place inside the ^{208}Pb target. After the decay, the inelastically scattered ^{12}C particles travel through the target material before being detected by the SiCD. The energy loss in the target after the decay was taken into account when calculating the β_i values. Figure 4.2 shows the calculated β_i values for the projectile just after the decay and after passing through the target (the energy loss in the target was calculated using the software SRIM [Zie10]). The

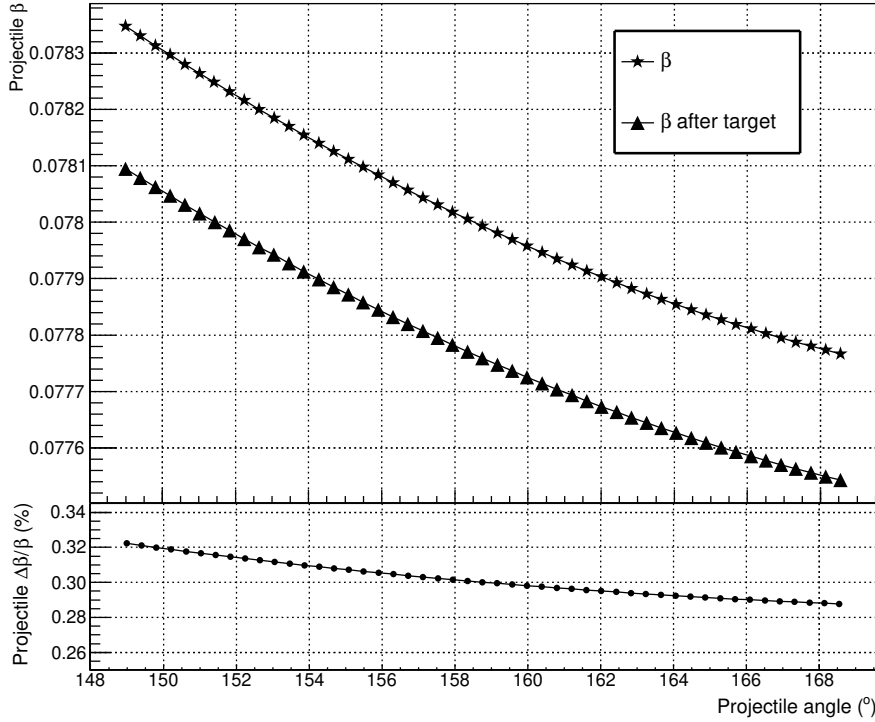


Figure 4.2: Results of the inelastic-scattering calculation of the recoil velocity (β) of the projectile after the decay. The results for before and after passing through the target are shown together with their relative change.

relative change between the beta values before and after ($\Delta\beta/\beta$) going through the target is also included in the plot and is of the order of $\sim 0.3\%$. Despite the Doppler correction for ^{12}C being very sensitive to the values of β_i , such small changes did not show a significant difference in the Doppler-corrected γ -ray spectrum. The same calculations of energy loss in the target were performed for the ^{208}Pb target, but the corrections were negligible since the Doppler shift is much less severe in this case, and the Doppler correction is less sensitive to the chosen β_i values than in the case of ^{12}C . Figure 4.3 shows the effect of the Doppler correction on the 3_1^- decay γ -ray photopeak of ^{208}Pb as an example of the effect of the Doppler corrections in the γ -ray spectra.

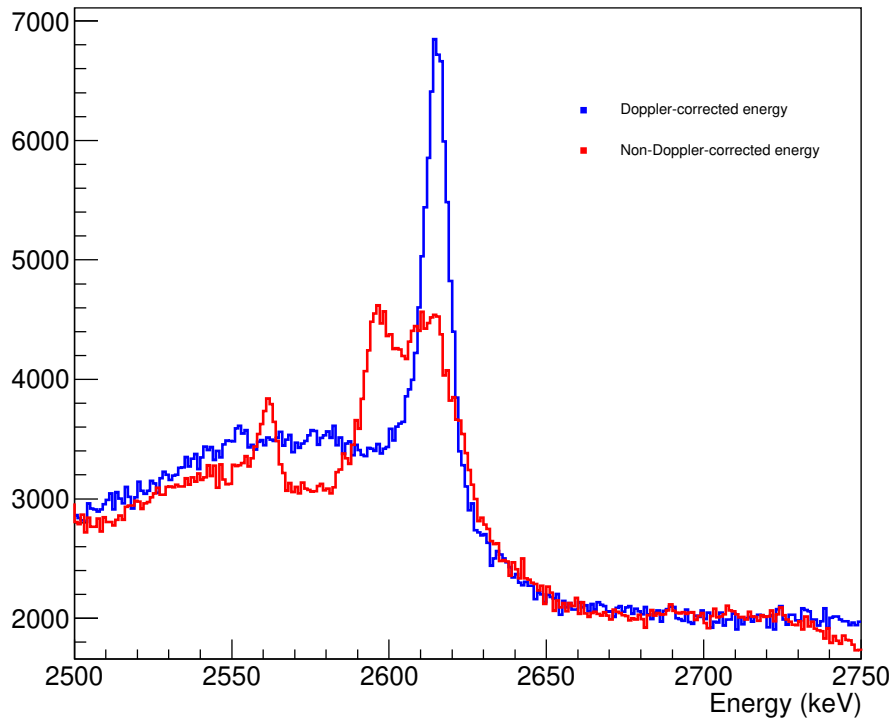


Figure 4.3: Total γ -ray energy measured with JUROGAMII Doppler-corrected and non-Doppler-corrected for the ^{208}Pb (3_1^-) target excitation.

4.1.2 Time gate

Each hit in SiCD detector by the backward-scattered ^{12}C ion is assigned an event time stamp (t_s). The difference between the coincident JUROGAMII γ -ray time (t_{JURO}) and the time stamp (t_s), ΔT , can be plotted versus the JUROGAMII γ -ray energy —Doppler-corrected for the target excitation— in order to set the time gates with the maximum precision possible. High precision in the time gates will result in a cleaner final γ -ray spectra, since uncorrelated background events will be rejected. Figure 4.4 shows a 2D-plot of the JUROGAMII γ -ray energy (Doppler-corrected for the ^{208}Pb excitation) as a function of the above mentioned time difference ΔT . At 2614 keV the peak coming from the 3_1^- state in ^{208}Pb can be observed. Different time gates of different widths were explored until finding the one that maximises the number of counts in the 3_1^- peak and minimises the contribution of the uncorrelated

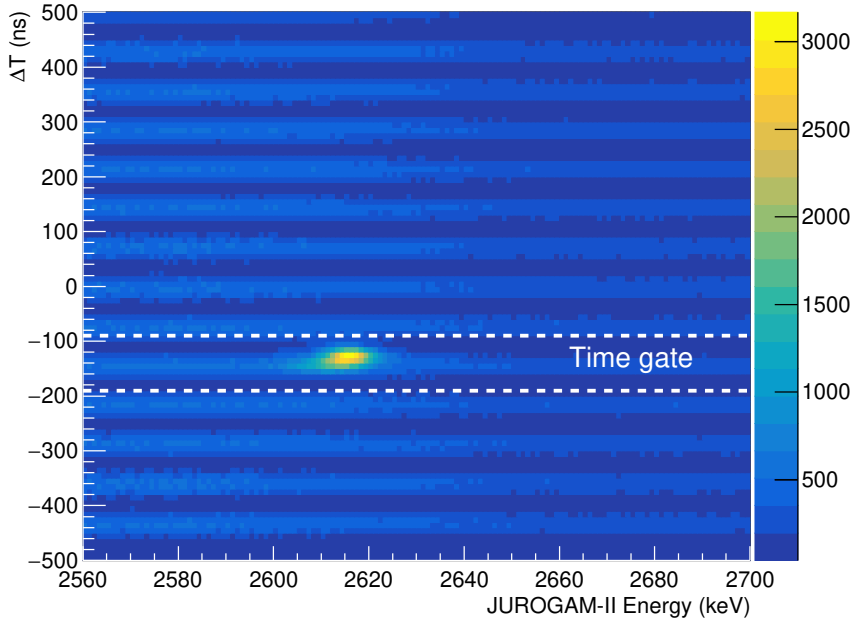


Figure 4.4: Time difference, ΔT , between the coincident JUROGAMII γ -ray time and the time stamp, $\Delta T = t_{Juro} - t_s$, vs. the JUROGAMII energy.

events. Figure 4.4 also shows the final time gate of 90 ns that was set. This time gate was used for the analysis of both the population of the states in ^{208}Pb and in ^{12}C since they occur almost precisely at the same time difference with respect to the ^{12}C ion hit.

In addition to the 90 ns prompt gate, a further background time gate was set including all events before and after the prompt gate. The width of the background time gate was made as large as possible in order to obtain a background γ -ray spectra with the best statistics possible. Figure 4.5 shows the time difference histogram between the coincident JUROGAMII γ -ray time and the time stamp, ΔT . Figure 4.5 also displays the different time gates used to trigger the prompt and background events, as well as the different “bumps” arising from the cyclotron frequency. The highest peak in the figure corresponds to the prompt γ -ray events. Figure 4.6 shows the prompt and background (scaled) γ -ray spectra resulting from the previously described time gates. A detailed discussion of the analysis of the γ -ray spectra including the background subtraction and scaling will be included in section 4.2.

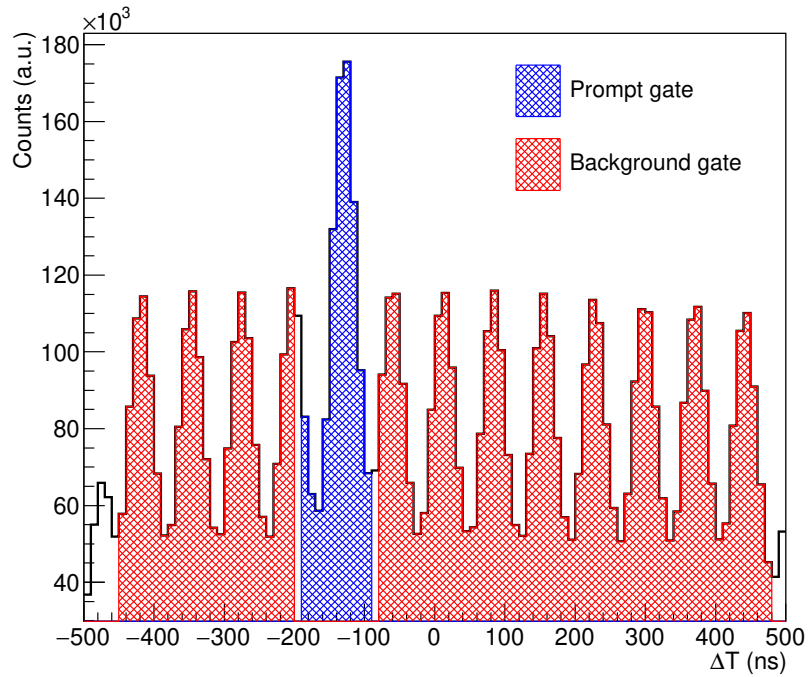


Figure 4.5: Prompt and background time gates for the data sorting, where $\Delta T = t_{\text{Juro}} - t_s$.

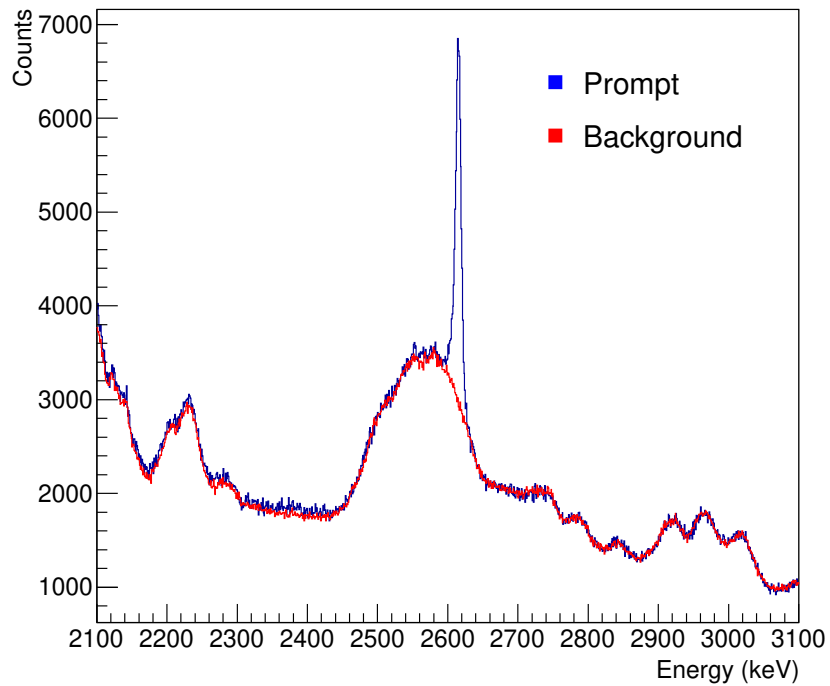


Figure 4.6: Measured JUROGAMII γ -ray Doppler-corrected energy spectrum with a prompt and background (scaled) time gate.

4.1.3 Particle-energy gates

The refined time gates helped improve the peak-to-background ratio of all the experimentally observed γ -ray transitions, namely the $2_1^+ \rightarrow 0_1^+$ in ^{12}C at 4439 keV, and the $3_1^- \rightarrow 0_1^+$ and $2_1^+ \rightarrow 0_1^+$ in ^{208}Pb at 2614 and 4085 keV, respectively. However, the much larger elastic-scattering cross section of ^{12}C in ^{208}Pb (several orders of magnitude larger) produced random γ -ray coincidences. These “random” γ rays (uncorrelated to the inelastic-scattering of the projectile or target) spread as background around the whole γ -ray spectrum, which made the analysis of the measured γ -ray spectra more difficult, particularly for the lowest cross section γ -ray transitions, the $2_1^+ \rightarrow 0_1^+$ in ^{12}C and ^{208}Pb .

Further particle-energy gates were set throughout the sorting process in order to reduce background events in these γ -ray spectra. This was achieved by setting an energy condition (a lower and higher bound) on the particle-energy measured by the rings in the SiCD detector. The energy of the inelastically scattered ^{12}C particles will differ from the elastically scattered ones by the energy of the γ -ray (E_γ), i.e.

$$E_{\text{inelast}} = E_{\text{elast}} - E_\gamma \quad (4.3)$$

as per kinematics, where the inelastic (E_{inelast}) and elastic (E_{elast}) particle energies will differ for each scattering angle (each ring). Despite the elastic and inelastic particle energies being able to be separated, the large tail of the much higher cross section elastic-scattering distribution will sit on top of the inelastic-scattering peak, making it practically unnoticeable. The goal is to find particle-energy gates for each γ -ray transition that preserve the maximum amount of inelastic events whilst also trying to minimise the elastic ones. This was achieved by centering each gate at the inelastic-scattering distribution peak.

In order to be able to set the right gates for each γ -ray transition, an auxiliary gate on the γ -ray spectrum can be set to “unbury” the inelastic-scattering peak from

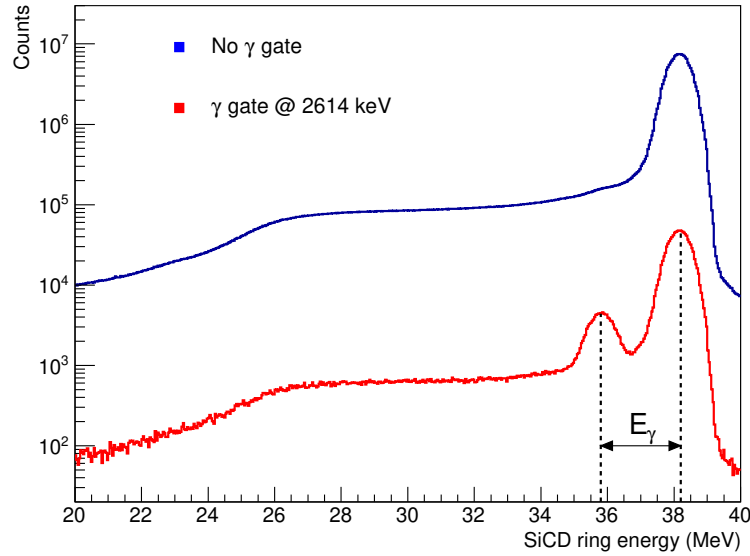


Figure 4.7: SiCD rings particle-energy spectra with and without a γ -ray energy gate around the 2614 keV 3_1^- ^{208}Pb photopeak.

the elastic-scattering background. Figure 4.7 shows how the inelastic-scattering peak for the 3_1^- γ -ray transition of ^{208}Pb can be observed after applying a γ -ray-energy gate around the 2614 keV γ -ray peak. This γ -ray-energy gate is also illustrated in Figure 4.8.

For the purpose of accurately choosing the particle and γ -ray energy gates, several 2D-histograms were produced (Figures 4.8, 4.10 and 4.12) containing the measured JUROGAMII γ -ray energies (Doppler-corrected for either ^{12}C or ^{208}Pb) vs the SiCD total ring energies – the sum of the energies of all the rings. The “cleaning” process of the γ -ray spectra for each transition consisted of:

- setting a γ -ray-energy gate at the energy of the transition of interest wide enough to include the whole photopeak (Figures 4.8 and 4.10),
- producing the γ -ray-energy-gated total ring particle-energy spectra by projecting the 2D-histogram into the X-axis (Figures 4.9 and 4.11),
- fitting the now visible inelastic scattering peak with a Gaussian distribution plus a second order polynomial background, obtaining the Gaussian's centroid

(E_0) and σ (Figures 4.9 and 4.11),

- removing the γ -ray-energy-gate, and
- setting an inelastic particle-energy gate centered at E_0 and wide enough to include the whole inelastic peak (whilst avoiding the elastic peak).

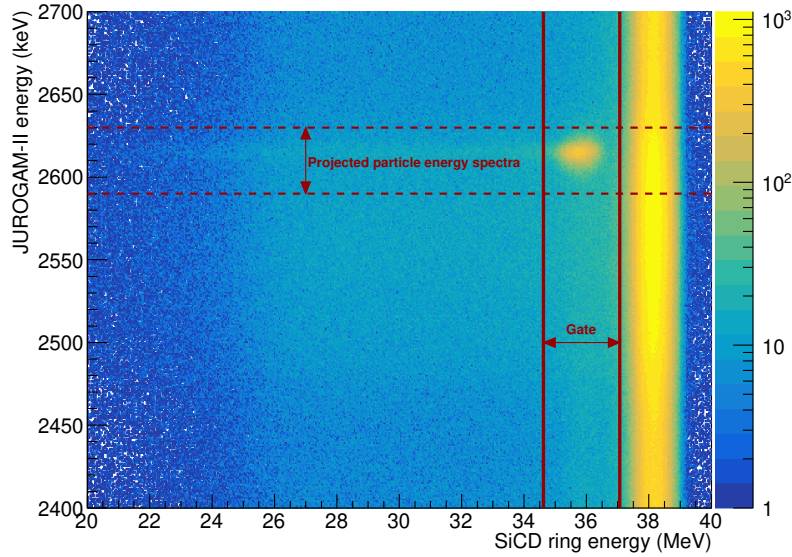


Figure 4.8: JUROGAMII γ -ray energy Doppler-corrected for ^{208}Pb vs the SiCD total ring energy spectrum. The auxiliary γ -ray-energy gate used to produce Figure 4.9 is shown with horizontal dashed lines and the final particle-energy gate for the 3_1^- transition in ^{208}Pb is shown with vertical lines.

The width of the final particle-energy gates was chosen to be of 3.5σ in order to ensure that the whole inelastic-scattering peak is included and the data is not biased. The severe Doppler shift and the low statistics for the case of the 2_1^+ in ^{12}C did not allow the production of a γ -ray-energy-gated ring particle-energy spectra where the inelastic scattering peak was visible. As a result, and in order to maintain consistency, a gate of the same width to the one for the 2_1^+ in ^{208}Pb and centered at

$$E_0^{12\text{C}(2^+)} = E_0^{208\text{Pb}(2^+)} - \left(E_\gamma^{12\text{C}(2^+)} - E_\gamma^{208\text{Pb}(2^+)} \right) = E_0^{208\text{Pb}(2^+)} - 0.35 \quad (\text{MeV}), \quad (4.4)$$

was set. Table 4.1 includes the final particle-energy gates used to produce the final γ -ray spectra.

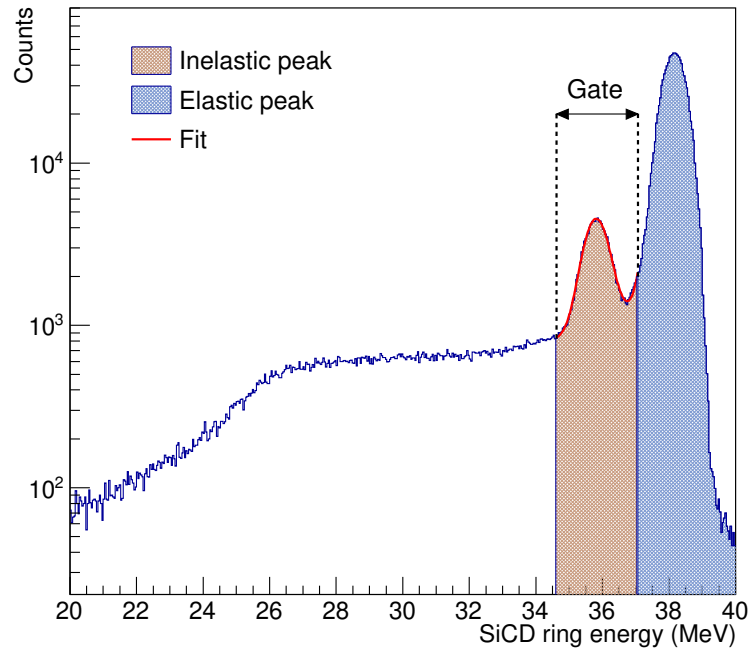


Figure 4.9: SiCD total rings particle-energy spectrum gated at the 3_1^- 2614 keV γ -ray-energy transition in ^{208}Pb .

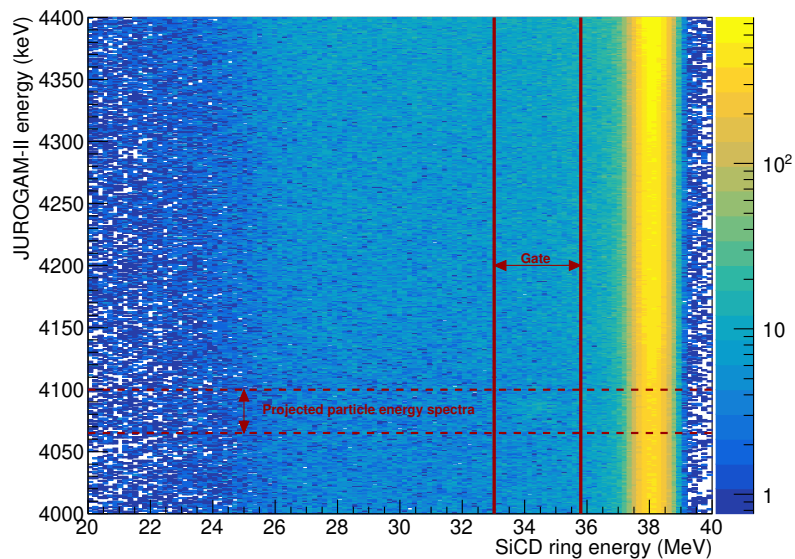


Figure 4.10: JUROGAMII γ -ray energy Doppler-corrected for ^{208}Pb vs the SiCD total ring energy spectrum. The auxiliary γ -ray-energy gate used to produce Figure 4.11 is shown with horizontal dashed lines and the final particle-energy gate for the 2_1^+ transition in ^{208}Pb is shown with vertical lines.

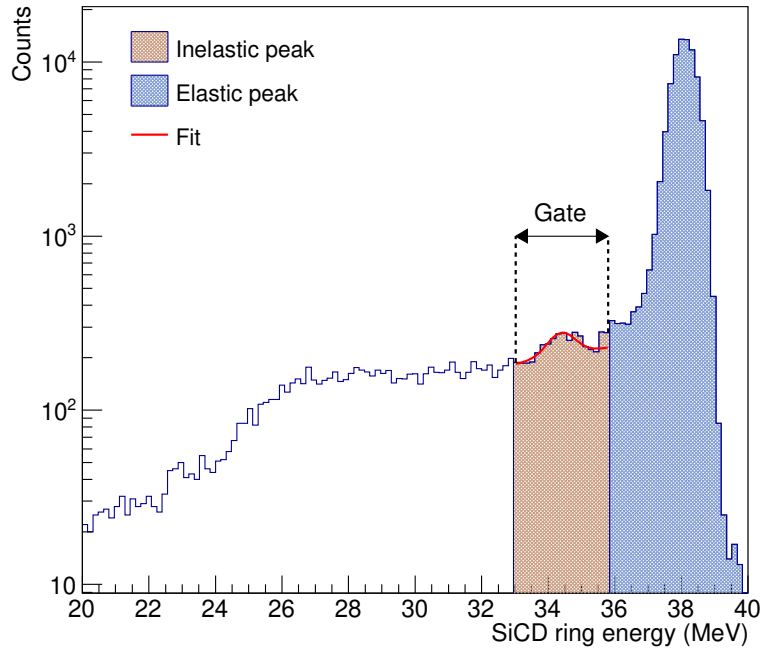


Figure 4.11: SiCD total rings particle-energy spectrum gated at the 2_1^+ 4085 keV γ -ray-energy transition in ^{208}Pb .

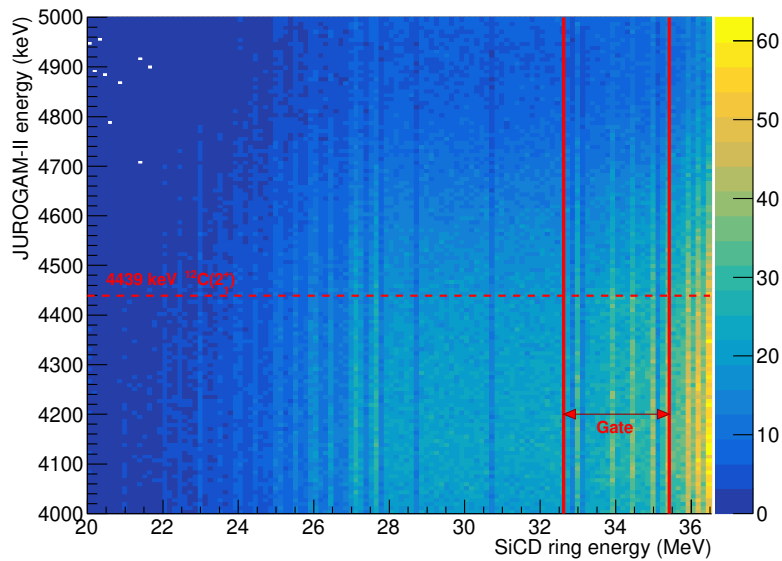


Figure 4.12: JUROGAMII γ -ray energy Doppler-corrected for ^{12}C vs the SiCD total ring energy spectrum. The final particle-energy gate for the 2_1^+ transition in ^{208}Pb is shown with vertical lines.

Table 4.1: Particle-energy gates used to produced the “cleaned” final γ -ray spectra.

Gate	E_{low} (MeV)	E_{high} (MeV)
^{208}Pb (3_1^-)	34.62	37.07
^{208}Pb (2_1^+)	33.02	35.80
^{12}C (2_1^+)	32.67	35.45

4.2 Gamma-ray spectra

Using the inelastic particle-energy gates described in table 4.1, time-gated (prompt and background) and Doppler-corrected γ -ray energy spectra were obtained for 2_1^+ in ^{12}C and the 3_1^- and 2_1^+ in ^{208}Pb .

Figure 4.13 shows the particle-energy-gated prompt γ -ray spectra Doppler corrected for the 2_1^+ in ^{12}C for each of the JUROGAMII rings. As it can be noted, there is a high-energy background which is Doppler-shifted towards higher energies as the JUROGAMII ring number increases, i.e. the detector angle $\theta_\gamma^{\text{JG}}$ decreases. This high-energy background is believed to arise from random coincidences of prompt γ rays from $^{12}\text{C} + ^{12}\text{C}$ reactions of the beam with the backing material in the target. It sits on top of the 4438 keV γ ray of the 2_1^+ in ^{12}C for the case of R3 and R4, causing a substantial decrease in the peak-to-background ratio for this particular transition.

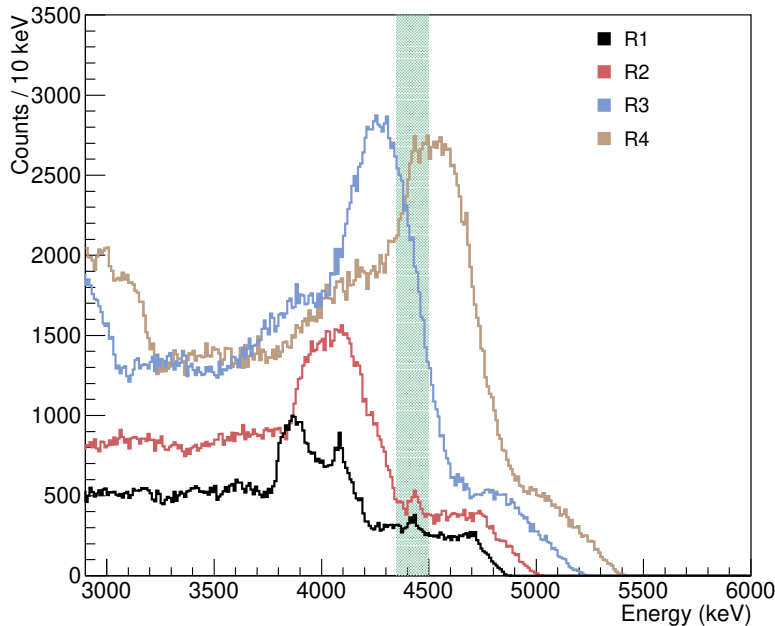


Figure 4.13: Particle-energy-gated prompt γ -ray spectra Doppler corrected for the 2_1^+ in ^{12}C measured with R1, R2, R3 and R4 of the JUROGAMII array. The shaded region shows where the $2_1^+ \rightarrow 0^+$ γ ray in ^{12}C is situated.

As discussed in section 4.1.2, a background time gate was set and a background spectrum was obtained which reproduces very accurately the “random” events of the prompt γ -ray spectrum (Figure 4.6). The scaling and subtraction of this measured background from the prompt spectra followed by the integration of the peaks was the chosen approach in order to obtain the number of counts for all observed γ -ray transitions, namely the 2_1^+ in ^{12}C , and 2_1^+ and 3_1^- peaks in ^{208}Pb . As such, the number of counts in each of the peaks can be obtained by integrating the background-subtracted spectra around the peak region, this is

$$C = P - n \cdot B, \quad (4.5)$$

where C stands for the “clean” (background-subtracted) spectra, and P and B stand for the prompt and background γ -ray spectra respectively.

The normalisation factor n for each photopeak in ^{12}C and ^{208}Pb can be obtained by subtracting the net number of background counts under the peak from the prompt spectra. This is achieved by defining two normalisation regions at the left and right hand sides of the peak ($N1$ and $N2$) and a photopeak region (PK) as illustrated in Figure 4.14. The normalisation regions were chosen to be of the same size and large enough to minimise statistical uncertainty. The effect of prompt Compton events on the regions at the left hand side of the peak is negligible compared to the number of background counts. The background normalisation factor was therefore defined as

$$n = \frac{P_{N1} + P_{N2}}{B_{N1} + B_{N2}}, \quad (4.6)$$

with uncertainty

$$\Delta n = n \cdot \sqrt{\frac{\Delta P_{N1}^2 + \Delta P_{N2}^2}{(P_{N1} + P_{N2})^2} + \frac{\Delta B_{N1}^2 + \Delta B_{N2}^2}{(B_{N1} + B_{N2})^2}}, \quad (4.7)$$

where P_{N1} , P_{N2} , B_{N1} and B_{N2} refer to the number of counts in the regions $N1$

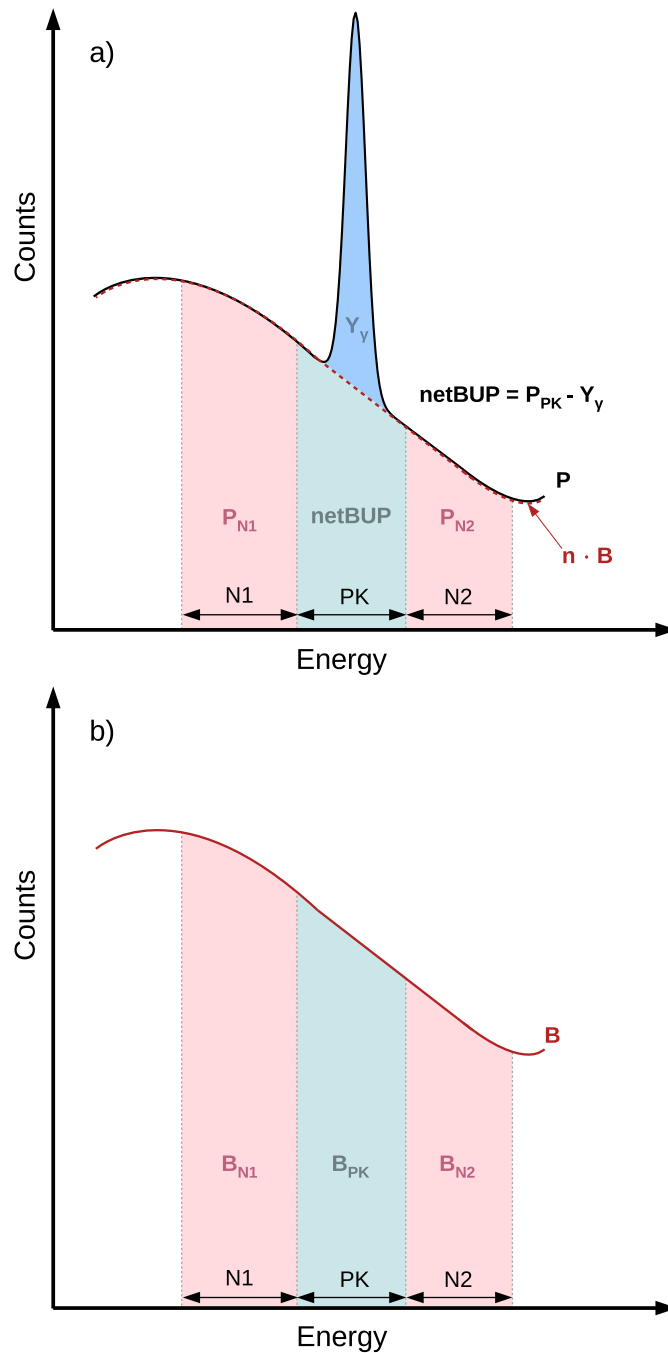


Figure 4.14: a) Sketch of the prompt γ -ray spectra (solid black line) with highlighted normalisation regions $N1$ and $N2$, net background under peak (netBUP) and the number of estimated counts in the photopeak or γ -ray yield ($Y_\gamma = C_{PK}$). The position where the normalised background would sit is also indicated (dashed dark red line). (b) Sketch of the background γ -ray spectra (solid dark red line) with highlighted normalisation regions $N1$, $N2$, and PK . See the text for more details.

and N_2 of the prompt and background spectra respectively. Their uncertainties, which are referred to as ΔP_{N_1} , ΔP_{N_2} , ΔB_{N_1} and ΔB_{N_2} in equation 4.7, are the standard deviations for Poisson distributions, i.e. $\Delta P_{N_1} = \sqrt{P_{N_1}}$, $\Delta P_{N_2} = \sqrt{P_{N_2}}$, $\Delta B_{N_1} = \sqrt{B_{N_1}}$ and $\Delta B_{N_2} = \sqrt{B_{N_2}}$.

For the normalisation factor described by equation 4.6, it is trivial to show that the net background under the peak (netBUP) for the “clean” spectrum (equation 4.5) is equal to zero, being the latter net background given by

$$\text{netBUP} = \frac{\text{PK}}{N_1 + N_2}(C_{N_1} + C_{N_2}) \quad (4.8)$$

where the factor $\text{PK}/(N_1+N_2)$ scales for the sizes of the regions PK, N_1 and N_2 and C_{N_1} and C_{N_2} stand for the number of counts of the background-subtracted spectrum in the regions N_1 and N_2 ,

$$C_{N_1} = P_{N_1} - n \cdot B_{N_1} \quad (4.9)$$

$$C_{N_2} = P_{N_2} - n \cdot B_{N_2}. \quad (4.10)$$

As discussed, the resulting clean spectra will then be given by equation 4.5 with the normalisation factor from 4.6. The number of counts in each photopeak will then be the integral of the clean spectra under the PK region, i.e.

$$C_{\text{PK}} = P_{\text{PK}} - n \cdot B_{\text{PK}}, \quad (4.11)$$

with uncertainty

$$\Delta C_{\text{PK}} = \sqrt{\Delta P_{\text{PK}}^2 + (n \cdot \Delta B_{\text{PK}})^2 + (B_{\text{PK}} \cdot \Delta n)^2}, \quad (4.12)$$

where Δn is given by equation 4.7, and with ΔP_{PK} and ΔB_{PK} being again standard deviations for Poisson distributions. It should be noted that for the background factor given by equation 4.6, the estimated number of counts in the peak C_{PK} cor-

responds to the γ -ray yield (Y_γ) with uncertainty $\Delta Y_\gamma = \Delta C_{\text{PK}}$.

At this point, equations 4.11 and 4.12 give the number of counts (or γ -ray yield Y_γ) and uncertainty for any given photopeak. However, as an alternative method to directly integrate the spectra over the peak region PK (equation 4.11), the resulting “clean”—background-subtracted—spectrum obtained using equation 4.5 can be fitted to a Gaussian with two exponential tails—one on the lower energy side and another one at the higher energy side. The uncertainty in each bin of the histogram can be propagated in an analogous way using equation 4.12 for each bin of the histogram. The number of counts in the peak can be found by performing an integral of the fitted function and the uncertainty can be obtained by propagating the uncertainties in the fitted parameters and the covariance matrix of the fit.

For the 3_1^- , the direct integration of the background-subtracted spectra and the integration of the previously mentioned fitted function gave equivalent results. The integral of the fit with the propagated uncertainty of the parameters was the number adopted as the γ -ray yield for this transition. Figure 4.15 (up) shows the background-subtracted γ -ray energy spectra for the 3_1^- state in ^{208}Pb and the obtained number of counts is recorded in table 4.2.

Similarly, despite the integration and fitting also providing equivalent results for the 2_1^+ in ^{208}Pb , the fit showed to be more unstable and its convergence dependent on the initial parameters used. The low cross section for the population of this excited state required a larger width of the bins used in the histogram (8 keV) in order to adequately visualise the photopeak. In addition, the 2_1^+ in ^{208}Pb still sits at 4085 keV, making it also vulnerable to the high-energy background discussed in Figure 4.13, which further encouraged the use of a larger bin width in order to increase the peak-to-background ratio. As a result, most counts of this photopeak were contained within 3 to 4 bins, making it more difficult for a fitted function to reproduce its shape. Consequently, the result arising from direct integration of the spectra was the adopted value for this γ -ray yield. The background-subtracted

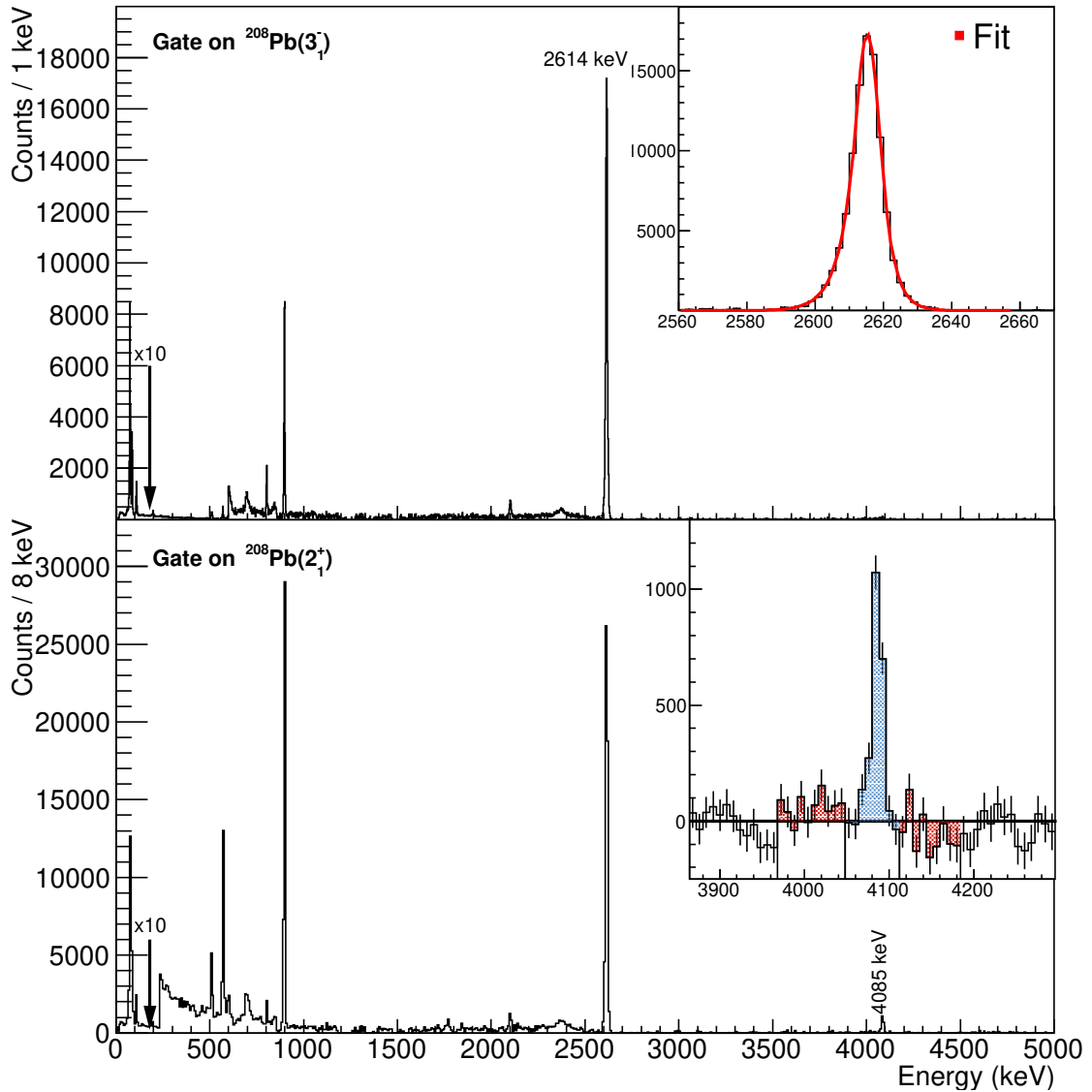


Figure 4.15: Background subtracted and Doppler-corrected γ -ray energy spectra with inelastic particle-energy gates for the 3_1^- (up) and 2_1^+ (down) excitations in ^{208}Pb . The inset in the upper plot shows the results of the fit of the photopeak to a Gaussian with two exponential tails. The inset in the lower plot shows an example of the peak (blue) and normalisation regions (red) at the left and right hand side of the peak are displayed for the 2_1^+ in ^{208}Pb .

γ -ray energy spectra for the 2_1^+ state in ^{208}Pb is shown in Figure 4.15 (down). Different normalisation, N1 and N2, and peak regions, PK, were explored and the number of counts in the peak and its systematic uncertainty were extracted for each combination of regions using equations 4.11 and 4.12. The different obtained γ -ray yields showed a very small standard deviation compared to the quoted statistical uncertainty. As a result, the average number of counts found for these different peak and normalisation regions was the final value used and is recorded in table 4.2 together with its average estimated uncertainty.

With regard to the 2_1^+ in ^{12}C , the extraction of the γ -ray yield was performed in an analogous way to the 2_1^+ in ^{208}Pb . However, the analysis and extraction of the number of counts of this photopeak was particularly challenging and with an increased uncertainty to that which was anticipated prior to the experiment, mainly due to: the relatively low statistics of the γ -ray peak combined with the wide Doppler broadening that it exhibits (due to higher recoil velocity than the target nuclei), and the decreased peak-to-background ratio arising from the unexpected high-energy background previously discussed. Nevertheless, similarly to the 2_1^+ in ^{208}Pb , different background normalisation (N1 and N2) and peak regions (PK) were explored and different number of counts in the photopeak were obtained. The variation of the normalisation regions was performed symmetrically and ranging from 70 keV to 130 keV at both sides of the peak. The standard deviation between the different numbers of counts obtained showed to be small compared to the quoted uncertainty and the final γ -ray yield and its uncertainty was determined to be the average (see table 4.2). Figure 4.16 shows the background-subtracted γ -ray energy spectra Doppler-corrected for 2_1^+ excitation in ^{12}C . The plot also displays an example of the normalisation (left and right of the peak) and peak regions used.

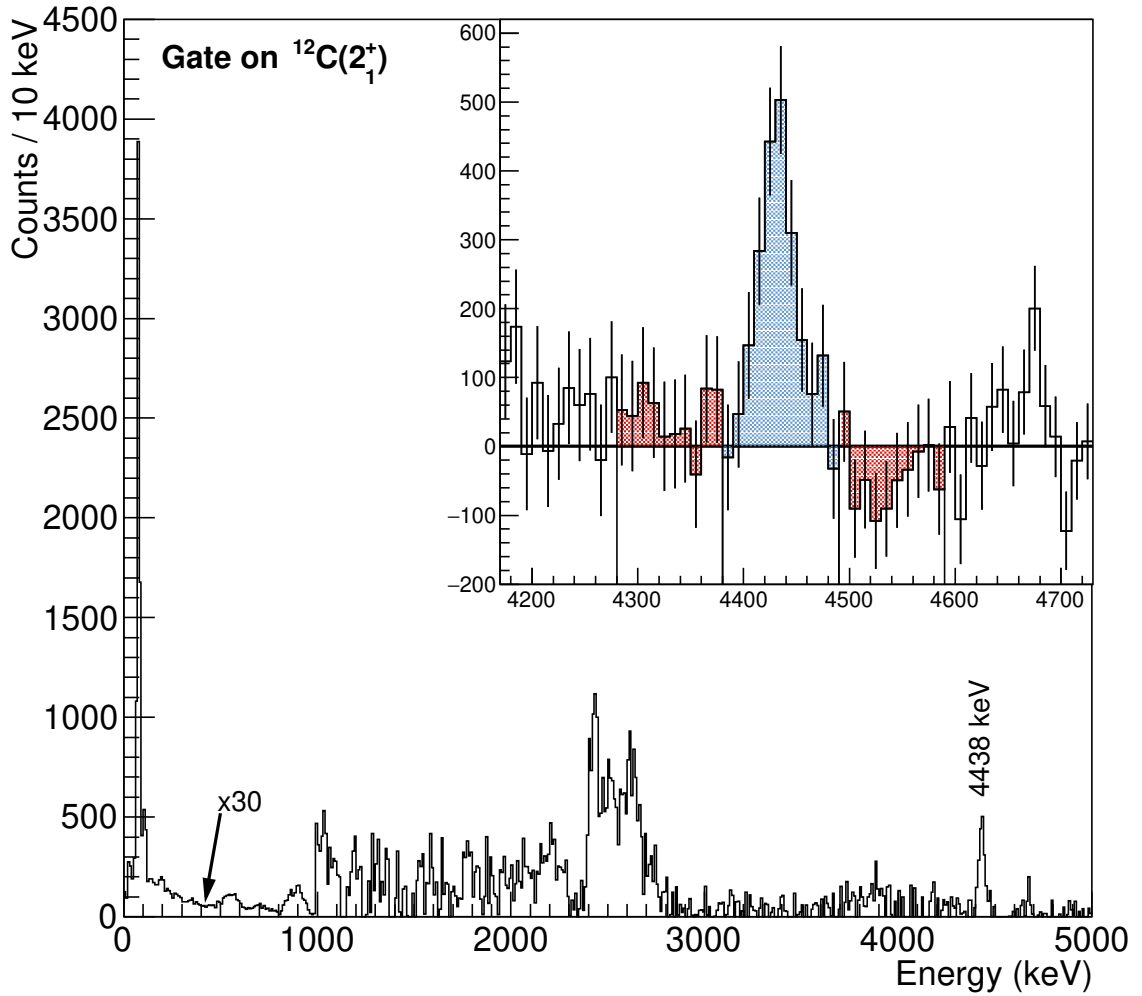


Figure 4.16: Background subtracted and Doppler-corrected γ -ray energy spectra with inelastic particle-energy gates for 2_1^+ excitation in ^{12}C . An example of the peak (blue) and normalisation regions (red) at the left and right hand side of the peak are displayed.

Table 4.2: Final γ -ray yields measured with the JUROGAMII array for the 2_1^+ in ^{12}C and 3_1^- and 2_1^+ in ^{208}Pb .

Photopeak	Energy (keV)	Counts	Error
^{208}Pb ($3_1^- \rightarrow 0^+$)	2614	97962	401
^{208}Pb ($2_1^+ \rightarrow 0^+$)	4085	2115	252
^{12}C ($2_1^+ \rightarrow 0^+$)	4438	2023	255

4.3 Nuclear interference

The main condition for the applicability of the semiclassical theory of Coulomb excitation lies in the assumption that the interaction between the colliding partners is purely electromagnetic. This condition applies when the separation distance between both interacting nuclei is greater than the range of the nuclear force. The effect of the Coulomb-nuclear interference has been studied in the past and it is known that at bombarding energies near the Coulomb barrier, the Coulomb-nuclear interference is destructive if the excitation function for pure Coulomb excitation is approaching or at a maximum [Gui78]. This destructive effect reduces the inelastic-scattering cross section at large scattering angles in a way consistent with the reorientation effect produced by negative quadrupole moment or with a prolate deformation in the laboratory frame. It is therefore of great importance to quantify the contribution of the Coulomb-nuclear interference to the inelastic cross section for an accurate extraction of the quadrupole moment.

4.3.1 Minimum distance between nuclear surfaces

Coulomb excitation cross sections increase with the bombarding energy whilst it is still within the “safe” range. This has given rise to finding a balance between maximising the cross section while minimising the effect of the Coulomb-nuclear interference. As a result, systematic studies have taken place in order to estimate the maximum bombarding energy at which the influence of the nuclear-excitation can be neglected for second-order processes such as the reorientation effect [Cli69, Les72]. The analysis of these experiments led to establishing a “safe” energy criterion for nuclei with $Z \geq 6$ supposed to ensure that nuclear excitation cross sections are $< 0.1\%$ if the distance of closest approach between nuclear surfaces in a head-on collision is

less than 5 fm, i.e.

$$s = D(\theta_{\text{CM}} = 180^\circ) - 1.25 \cdot (A_1^{1/3} + A_2^{1/3}) < 5 \text{ fm}. \quad (4.13)$$

Here the nuclear radii have been expressed as $1.25 \cdot A^{1/3}$ for each colliding nuclei, and the distance of closest approach at a scattering angle θ_{CM} is given by

$$D(\theta_{\text{CM}}) = 0.71998 \frac{Z_1 Z_2}{E_{\text{LAB}}} \left(1 + \frac{A_1}{A_2} \right) \left(1 + \sin\left(\frac{\theta_{\text{CM}}}{2}\right)^{-1} \right), \quad (4.14)$$

where Z_1 , A_1 and Z_2 , A_2 are the projectile and target atomic and mass numbers respectively, E_{LAB} is the energy of the incoming projectile in the laboratory frame in MeV and D is the distance of closest approach in fm. Other authors prescribe a minimum distance between nuclear surfaces no greater than 6.5 fm at the experiment's scattering angle [Spe81].

Alternatively, the nuclear radii can be more accurately expressed in terms of the matter half-density radii of a Fermi distribution [Mye74, Wil80] as,

$$C_i = R_i(1 - R_i^{-2}) \quad (4.15)$$

where R_i is the nuclear radius for an homogeneous mass distribution, which is parameterised as

$$R_i = 1.28A_i^{1/3} - 0.76 + 0.8A_i^{-1/3}. \quad (4.16)$$

The distance of closest approach could then be expressed as $D(\theta_{\text{CM}}) = C_1 + C_2 + s$. However, for the case of lighter nuclei distances larger than $s = 5$ fm may be required in order to ensure the “safety” of the experiment. Figure 4.17 shows experimental results for the minimum distance between nuclear surfaces necessary to neglect Coulomb-nuclear interference effects [Wol92]. In this figure, the two ^{12}C data points relevant to the present work yield a minimum distance of $D = 15.1(7)$ fm and $D = 15.6(8)$ fm. Equations 4.16 and 4.15 yield the value of $C_1 + C_2 = 8.94$ fm

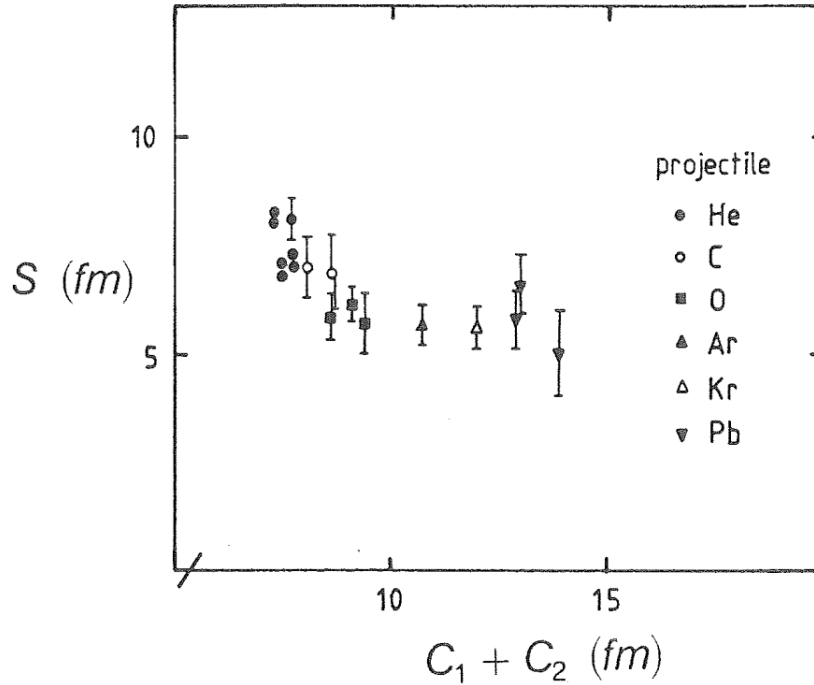


Figure 4.17: Experimental values of the minimum distance between nuclear surfaces s (fm) vs. the sum of the radii of the interacting nuclei, $C_1 + C_2$ (fm), necessary to ensure a pure electromagnetic interaction and therefore a “safe” Coulomb excitation experiment, for different projectile and target combinations [Wol92].

for the case of ^{12}C on ^{208}Pb which, using the most conservative of the two previous experimental values, gives a minimum distance between surfaces of $s = 6.7(8)$ fm necessary for the present work to be completely “safe”.

Figure 4.18 shows the distance between nuclear surfaces s , equation 4.14, as a function of the center-of-mass scattering angle using $1.25 \cdot (A_1^{1/3} + A_2^{1/3})$ and equations 4.16 and 4.15 as the sum of the nuclear radii respectively. From this figure, it can be seen that the present work fulfils the criteria of $s > 5$ fm at $\theta_{\text{CM}} = 180^\circ$ (red line). However, it can also be seen that for the more accurate description of the nuclear radii by using equations 4.16 and 4.15, the minimum distance between surfaces ranges from 6.8 fm to 7.1 fm, which is within or beyond the experimental limits provided by [Wol92] depending on the experimental error bar. A graphical representation of this is presented in Figure 4.19. Here the hyperbolic elastic-scattering trajectory of ^{12}C into ^{208}Pb has been computed in the target frame of reference. In

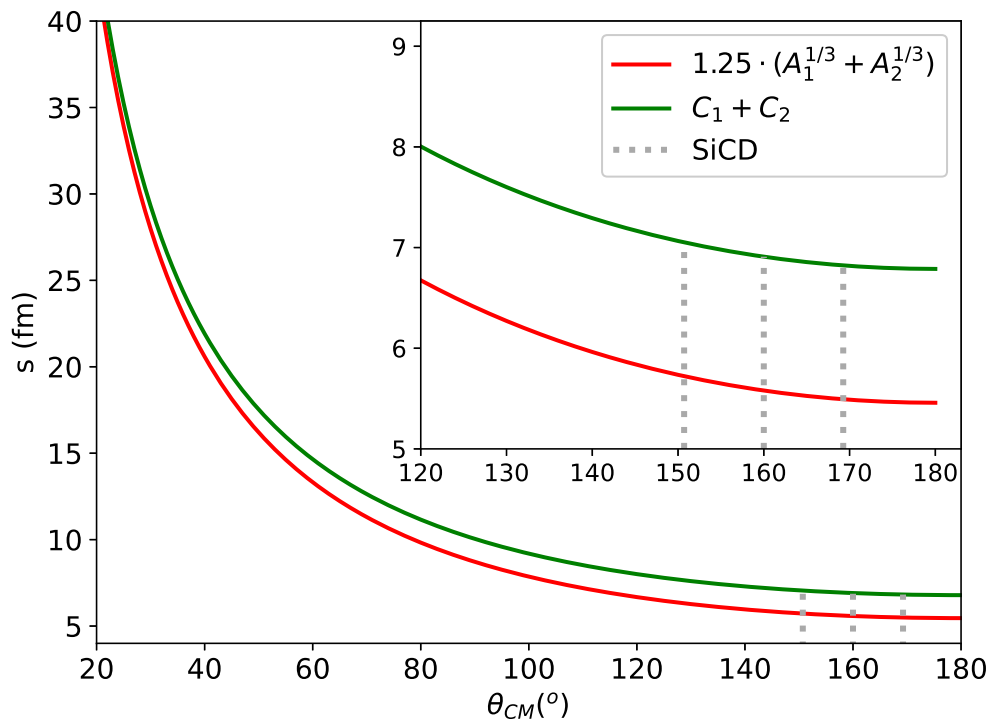


Figure 4.18: Minimum distance between nuclear surfaces as a function of the center-of-mass scattering angle using $1.25 \cdot (A_1^{1/3} + A_2^{1/3})$ (red line) and equations 4.16 and 4.15 (green line) as the sum of the nuclear radii respectively. The center-of-mass angles covered in the present experiment are shown as dotted black lines.

addition, ^{12}C and ^{208}Pb have been represented as circumferences of radii equal to C_i placed at distance of closest approach for a scattering angle of $\theta_{\text{CM}} = 160^\circ$ for ^{12}C , and in the origin for ^{208}Pb . The nuclear interaction limit of $s = 6.7(8)$ fm has been represented as a circumference of radius $C_2 + 6.7(8)$ fm and, as it can be seen the experiment will be “safe” when the projectile circumference does not intersect with the nuclear interaction one.

A Coulomb excitation experiment of ^{12}C by a ^{208}Pb target similar to the one presented in this thesis was carried out by Vermeer and collaborators [Ver83, Spe83, Ver84b]. The authors performed a systematic study of the Coulomb excitation probability as a function of the beam energy for energies ranging from 52 to 58 MeV at a scattering angle of $\theta_{\text{LAB}} = 90^\circ$ ($\theta_{\text{CM}} = 93.33^\circ$). In their published work, it was concluded that Coulomb-nuclear interference effects started to arise

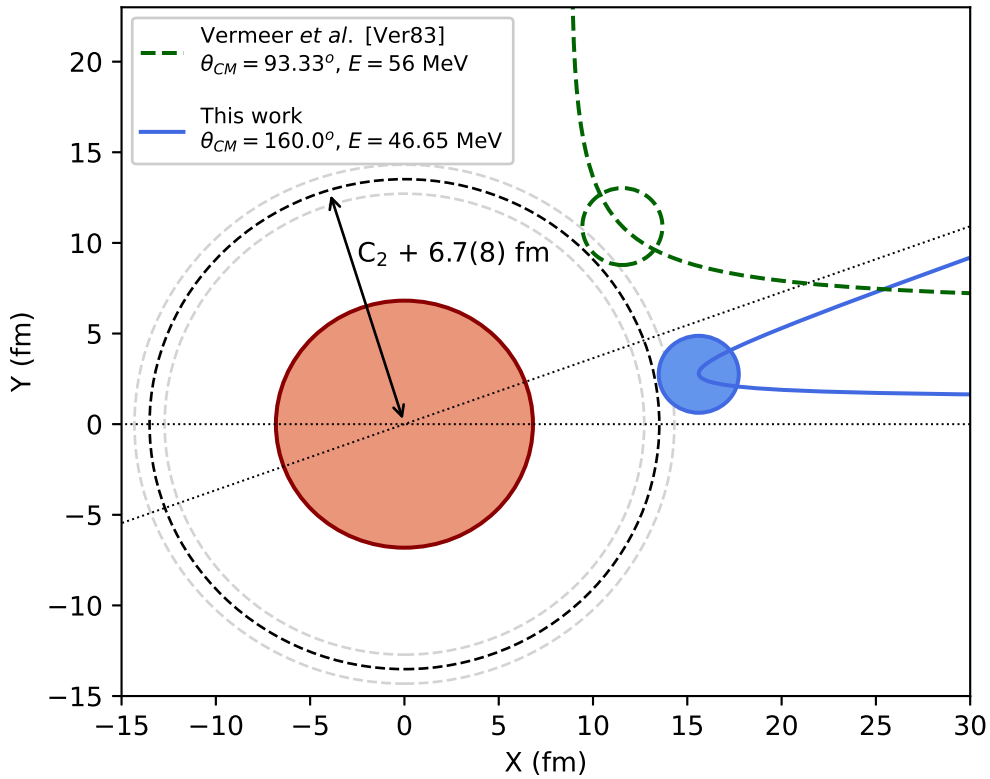


Figure 4.19: Hyperbolic elastic-scattering trajectory of ^{12}C into ^{208}Pb computed in the target frame of reference. The projectile and target nuclei are represented as circumferences of radii equal to C_i placed at distance of closest approach for a scattering angle of $\theta_{CM} = 160^\circ$ for ^{12}C , and in the origin for ^{208}Pb . The nuclear interaction limit of $s = 6.7(8)$ fm shown as a circumference of radius $C_2 + 6.7(8)$ fm.

at 58 MeV ($s = 5.1$ fm) and were therefore not present in their measurement at 56 MeV ($s = 5.6$ fm) for the $^{12}\text{C} + ^{208}\text{Pb}$ system. Figure 4.19 shows the hyperbolic elastic-scattering trajectory of a 56 MeV ^{12}C beam into a ^{208}Pb at a scattering angle of $\theta_{\text{CM}} = 93.33^\circ$ (green dashed line). As shown in Figures 4.19 and 4.18, the distance between nuclear surfaces at the point of closest approach in the present experiment is of the same order to that in Vermeer’s work at 56 MeV (~ 5.6 fm), which strongly suggests that Coulomb-nuclear interference effects are also negligible for the quoted beam energy and scattering angle. Nevertheless, the degree to which experiments may be regarded as free from nuclear effects will depend on factors specific to each experiment, such as the Coulomb and nuclear reaction amplitudes at the specified scattering angle and the sensitivity to nuclear effects of the particular manifestation of the reorientation effect which is being observed [Spe81].

4.3.2 DWBA calculations

It would be highly desirable to determine the maximum safe bombarding energy by measuring the excitation function through the Coulomb barrier region for the particular experimental conditions. However, it can be challenging for low cross section Coulomb excitation experiments, especially those involving the measurement of γ rays.

An alternative approach is to use a fully quantal code, such as PTOLEMY [Mac78] or FRESCO [Tho88], to reliably estimate the Coulomb-nuclear interference effect at near-barrier bombarding energies. For the present work, initial calculations of the inelastic-scattering cross sections were made with both quantal codes leading to the same results, and therefore the final full analysis was performed only with PTOLEMY due to its simplicity of the input files.

In PTOLEMY, the interaction between the two nuclei is represented by the addition of a Coulomb potential plus a nuclear potential. The Coulomb potential is defined by a radial parameter r_{C0} such that its “radius” is $R_{\text{C}} = r_{\text{C0}}A^{1/3}$ and the

reduced transition probability associated with the radiative transition of multipole order $E\lambda$, $B(E\lambda)$. The nuclear potential consists of a real (scattering) and an imaginary (absorptive) part, each of which is a Woods-Saxon function characterised by a well depth V (or W), radius r and surface diffuseness a . The relevant Schrödinger equation for the scattering is solved using the distorted-wave Born approximation (DWBA) for a single reaction channel.

The probability of exciting the 3_1^- state in ^{208}Pb by a ^{12}C projectile at near barrier energies has been studied by Robson and collaborators [Rob93]. In this study, the authors used an optical-potential to reproduce experimental data on the inelastic excitation probability of the 3_1^- in ^{208}Pb by a ^{12}C beam at backward scattering angles ($\theta_{\text{CM}} = 172^\circ$) and bombarding energies ranging from 42 to 62 MeV. In the DWBA calculations, the imaginary part of the optical-potential was assumed to vary linearly with the bombarding energy. The strength of the real part of the optical-potential was calculated using the dispersion relation. The diffusiveness and radius parameters for both the real and imaginary parts of the potential were assumed to be energy independent and were kept fixed to the values obtained by [Fri89] ($r_V = r_W = 1.256$ fm and $a_V = a_W = 0.56$ fm) from a fit to the elastic-scattering cross section of ^{12}C into ^{208}Pb at 96 MeV. The similarity in the experimental conditions of [Rob93] together with the excellent agreement between their DWBA calculations and the measured inelastic cross sections at $\theta_{\text{CM}} = 172^\circ$ encourages, in principle, the use of the above mentioned optical-model parameters for the Coulomb-nuclear interference effect estimations of the present work. Table 4.3 shows the values used for the calculations performed with PTOLEMY.

Figures 4.20 and 4.21 show the Coulomb excitation differential cross section computed with PTOLEMY and the optical-potential parameters from Robson *et al.* (table 4.3) for the 2_1^+ in ^{12}C , and the 2_1^+ and 3_1^- in transitions ^{208}Pb , respectively. As demonstrated, there is some destructive interference for the observed transitions at backward scattering angles, most noticeably for the 2_1^+ in ^{12}C . This destructive

Table 4.3: Optical model parameters from [Rob93] and [San01] used to estimate the Coulomb-nuclear interference effect.

Parameter	Robson <i>et al.</i> [Rob93]	Santra <i>et al.</i> [San01]
V	49.03 MeV	74.13 MeV
r_V	1.256 fm	0.426 fm
a_V	0.56 fm	3.95 fm
W	0 MeV	1.282 MeV
r_W	1.256 fm	1.261 fm
a_W	0.56 fm	0.313 fm

interference can be accounted for by correcting the measured γ -ray yields by an interference factor, INTF, defined as the ratio between the pure Coulomb excitation (dashed line in Figures 4.20 and 4.21) and Coulomb plus nuclear interference (solid line) solid-angle-integrated cross sections.

Nonetheless, the parameters of the optical-potential obtained in the DWBA analysis performed by Robson and collaborators were extracted only from fits to the elastic-scattering cross section at 96 MeV and the inelastic excitation of the 3_1^- in ^{208}Pb at a specific angle ($\theta_{\text{CM}} = 172^\circ$). As a result, the extension of the applicability of these parameters to estimate the interference effects in the 2_1^+ in ^{12}C at all scattering angles is questionable, since the parameters have not been benchmarked against the elastic-scattering cross sections at energies around 47.65 MeV nor the inelastic-scattering cross section of the 2_1^+ in ^{12}C .

Alternatively, Santra and collaborators [San01] performed a systematic study of the elastic-scattering cross section of ^{12}C into ^{208}Pb at energies ranging from 59 MeV up to 118 MeV. In their published work, they performed a phenomenological optical-potential fit to the elastic cross section as a function of the scattering angle for the different energies. Their phenomenological fit of a Woods-Saxon-shaped potential provided a good description of the elastic cross section at energies above the barrier [Gas02]. The parameters from the fit to the elastic-scattering cross section at their lowest incident energy (59 MeV), i.e. as close as possible to the 47.65 MeV beam

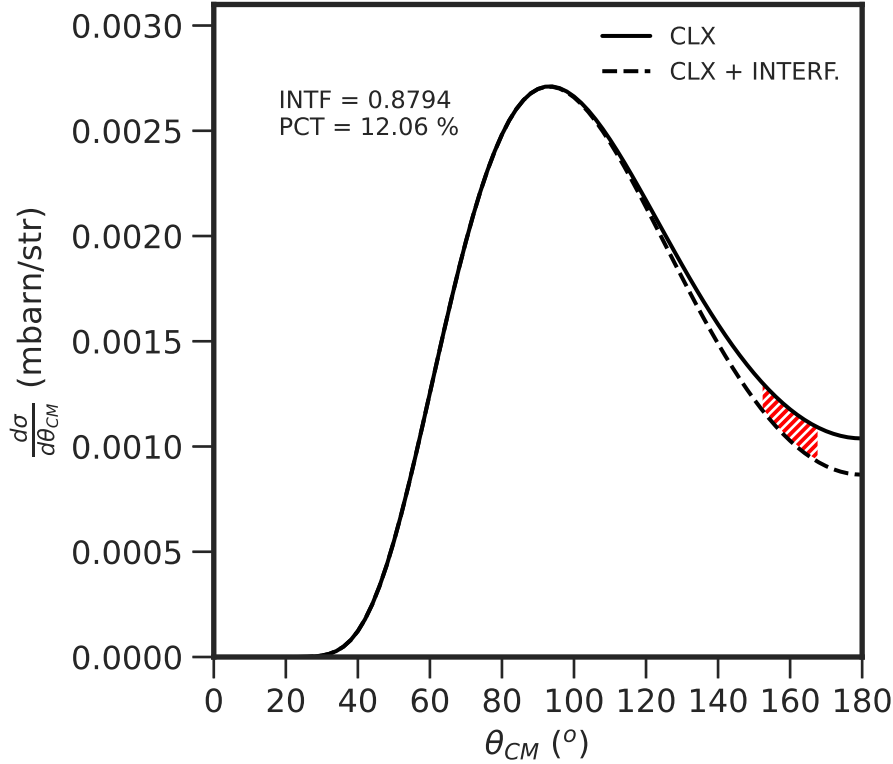


Figure 4.20: Coulomb excitation differential cross section of the 2_1^+ in ^{12}C with (dashed line) and without (solid line) Coulomb-nuclear interference computed with the DWBA code PTOLEMY and the optical-potential parameters from [Rob93]. The angles in the center-of-mass covered by the SiCD detector in the present experiment are indicated by the red shaded area and the obtained interference factor for those angles are displayed in the top left both as a factor and equivalently as a percentage.

energy used in the present work, can also be used to estimate the Coulomb nuclear interference effects in the inelastic-scattering cross section of the different excited states in the projectile and target. Figure 4.22 shows the ratio between the Coulomb excitation plus nuclear interference ($d\sigma_{\text{CN}}/d\theta$) and the pure Coulomb excitation ($d\sigma_{\text{C}}/d\theta$) differential cross sections $d\sigma_{\text{CN}}/d\sigma_{\text{C}}$ at 47.65 MeV using the parameters from the fit to the elastic-scattering cross section at 59 MeV from [San01] (bottom) and the parameters from [Rob93] (top). It can be noted that the optical-potential parameters from Santra and collaborators yields almost no interference in all cross sections ($\sim 1.6\%$ in the worse case), which is consistent with what was discussed in section 4.3.1.

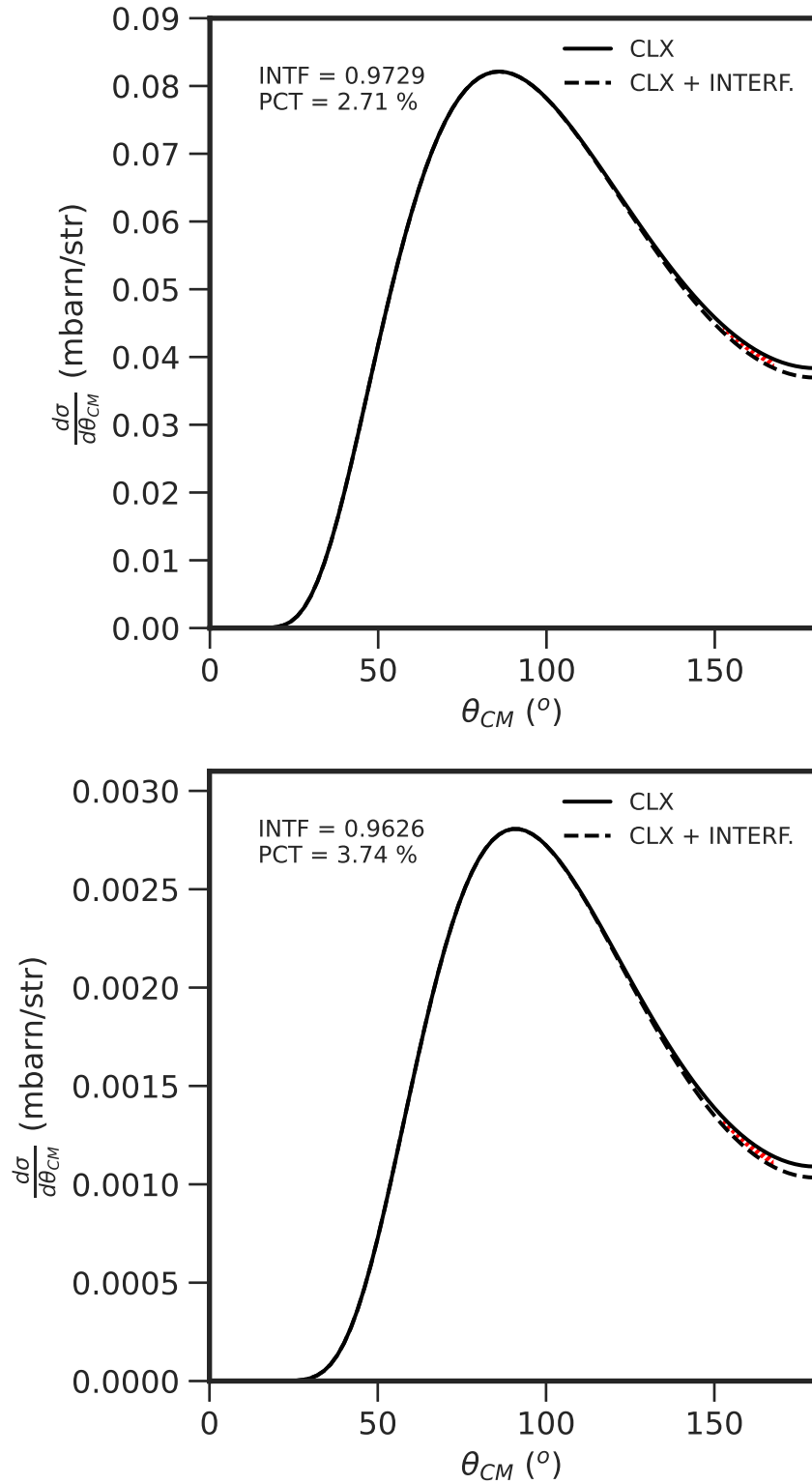


Figure 4.21: Coulomb excitation cross section of the 3_1^- (top) and 2_1^+ (bottom) in ^{208}Pb with (dashed line) and without (solid line) Coulomb-nuclear interference computed with the DWBA code PTOLEMY and the optical-potential parameters from [Rob93]. The angles in the center-of-mass covered by the SiCD detector in the present experiment are indicated by the red shaded area and the obtained interference factor for those angles are displayed in the top left both as a factor and equivalently as a percentage.

In summary, as discussed in section 4.3.1, the present experiment complies with most of the different prescriptions for a “safe” Coulomb excitation experiment. In addition, the distance between nuclear surfaces, s , at the point of closest approach is of the same order to that in the previous experimental work presented by Vermeer and collaborators [Ver83], where the presence of Coulomb-nuclear interference at such distances was discarded by the measurement of the Coulomb excitation probability at different beam energies. Nevertheless, a DWBA analysis of the Coulomb nuclear interference has been performed with the code PTOLEMY and the available optical-potential parameters from [Rob93] and [San01]. The investigations showed that there is a significant dependence on the optical-potential parameters chosen when one tries to estimate these effects using a DWBA code, making it therefore desirable to have more cross section data in the sub-barrier energy range. The optical-potential from [San01] is in agreement with the assumption of no nuclear interference, whilst the one extracted from [Rob93] estimates an interference of up to $\sim 12\%$ for the 2_1^+ in ^{12}C . Since there is substantial experimental evidence from [Ver83] suggesting that there is no nuclear interference effects, as well as the present work complying or being within the limit of most “safe-energy” prescriptions for Coulomb excitation experiments, it will be considered hereafter that this experiment constitutes a “safe” Coulomb excitation experiment. Nevertheless, the impact that a potential destructive Coulomb-nuclear interference would have in the final result will also be presented in section 4.5. For this, the parameters from [Rob93] will be used to correct the measured γ -ray yields and obtain additional values of the $Q(2_1^+)$ in ^{12}C .

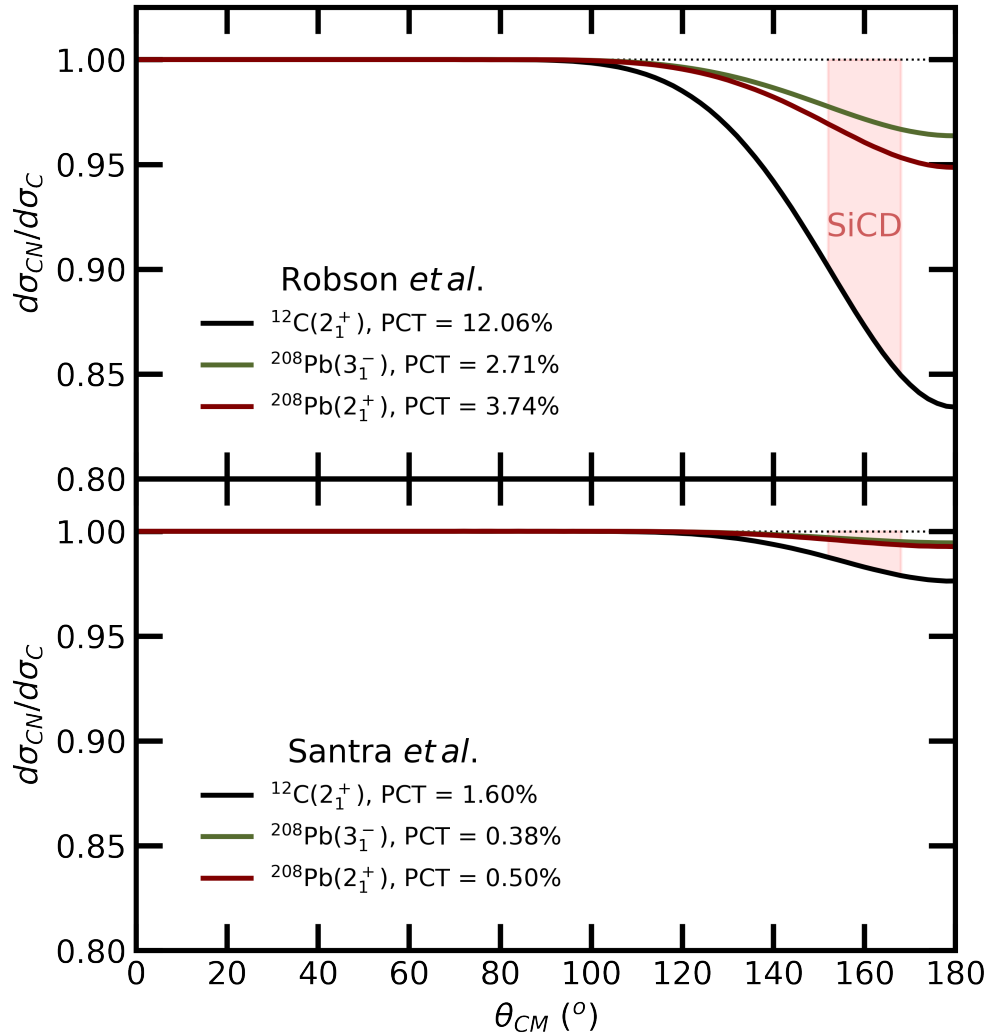


Figure 4.22: Ratio between the Coulomb excitation plus nuclear interference ($d\sigma_{CN}/d\theta$) and the pure Coulomb excitation ($d\sigma_C/d\theta$) differential cross sections $d\sigma_{CN}/d\sigma_C$. The calculations were performed with PTOLEMY using a beam energy of 47.486 MeV (center of the target) and the parameters from [Rob93] (top) and the fit to the elastic-scattering cross section at 59 MeV from [San01] (bottom).

4.4 GOSIA analysis

4.4.1 GOSIA2 input

For the calculation of the excitation cross section and the fitting of the matrix elements, GOSIA2 requires two parallel inputs describing both collision partners. Information regarding the beam and target species, along with beam energy and scattering angle, will be common to both input files, whilst the nuclear-structure information, energy levels and matrix elements will be introduced in separate input files for the projectile and target nuclei respectively.

Additional experimental information, such as the γ -ray detection efficiency, target thickness or the particle detection angular range, is included in both projectile and target input files in GOSIA2. The γ -ray detection efficiency for each of the modules of the JUROGAMII array was implemented by introducing the set of coefficients a_i described in equation 3.4. The target thickness was defined using the incident and exit beam energy, calculated using the SRIM software [Zie10]. The angular integration range in the laboratory frame of reference is given by the recoil detection angles of the SiCD detector, where, since the S2 SiCD detector is not symmetrical in ϕ , the integration limits were introduced by means of a $\theta - \phi$ map as described in [Zie16].

The measured γ -ray yields together with the associated uncertainty for each of the observed transitions (table 4.2) are given in a separate file which is read by the code at run time. A correction factor of 0.9899, calculated following the iterative method described in [Zie16], was introduced to account for the impurities in the 99.0% enriched ^{208}Pb target and multiplied to the ^{12}C γ -ray yield.

The geometry of the JUROGAMII array, i.e. the position and size of each of the detector module crystals, is also introduced in a separate input file read by the code at the start of the run.

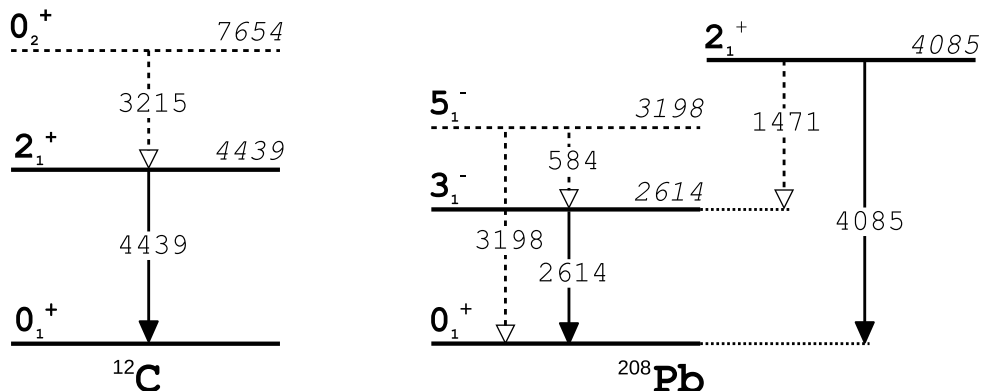


Figure 4.23: Level schemes of ^{12}C and ^{208}Pb as implemented in GOSIA2. The solid lines denote experimentally observed transitions, whilst the dashed lines are “virtual” or unobserved.

Figure 4.23 shows the level schemes of ^{12}C and ^{208}Pb as implemented in GOSIA2. These level schemes include experimentally observed γ -ray transitions, namely the 2_1^+ in ^{12}C and 3_1^- and 2_1^+ in ^{208}Pb , as well as other unobserved states and matrix elements that might contribute to the relevant Coulomb excitation cross sections in the projectile or target. Both projectile and target constitute coupled-channel systems, which makes it highly important to include higher unobserved states in order to avoid the overestimation of the transition amplitudes to a certain level of interest.

Spectroscopic data from previous measurements describing observed and unobserved transitions are included as additional data points and those used for the present analysis are included in table 4.4 together with the appropriate references. The experimental data point for the $Q(2_1^+)$ in ^{208}Pb was not used since, after reviewing the original publication which provides the value of $Q(2_1^+) = -0.7(3)$ eb [Ver84b], it was noted that the former value of the quadrupole moment was obtained using $B(E2; 0_1^+ \rightarrow 2_1^+) = 0.329(16)$ $e^2\text{b}^2$ from (e, e') experiments. The current adopted value for the $B(E2; 0_1^+ \rightarrow 2_1^+) = 0.287(18)e^2\text{b}^2$ [Pri17], which yields $Q(2_1^+) \approx 0$. As a result, the matrix element was left as a free parameter during the fit. Finally,

Table 4.4: Additional spectroscopic data of ^{12}C and ^{208}Pb used in the GOSIA analysis.

Nuclei	Experimental	Datum	GOSIA	Datum	Ref.
^{12}C	$B(E2; 0_1^+ \rightarrow 2_1^+)$	$39.7(2.0) e^2\text{fm}^4$	$\langle 2_1^+ E2 0_1^+ \rangle$	$0.0630(16) \text{ eb}$	[Pri16]
^{12}C	$B(E2; 2_1^+ \rightarrow 0_1^+)^a$	$7.63(19)^a e^2\text{fm}^4$	$\langle 2_1^+ E2 0_1^+ \rangle^a$	$0.06177(77)^a \text{ eb}$	[D'A20]
^{12}C	$B(E2; 0_2^+ \rightarrow 2_1^+)$	$8.25(82) \text{ W.u.}$	$\langle 0_2^+ E2 2_1^+ \rangle$	$0.0367(19) \text{ eb}$	[Kel17]
^{208}Pb	$\text{b.r.}(2_1^+ \rightarrow 3_1^-)$	$0.0046(15)$			[Mar07]
^{208}Pb	$T_{1/2}(5_1^-)$	$294(15) \text{ ps}$	$\tau(5_1^-)$	$424(22) \text{ ps}$	[Mar07]
^{208}Pb	$T_{1/2}(2_1^+)$	$0.80(4) \text{ fs}$	$\tau(2_1^+)$	$0.00115(6) \text{ ps}$	[Mar07]
^{208}Pb	$B(E3; 0_1^+ \rightarrow 3_1^-)$	$0.611(9) e^2\text{b}^3$	$\langle 3_1^- E3 0_1^+ \rangle$	$0.782(6) \text{ eb}^{3/2}$	[Spe89]
^{208}Pb	$Q(3_1^-)$	$-0.34(15) \text{ eb}$	$\langle 3_1^- E2 3_1^- \rangle$	$-0.26(12) \text{ eb}$	[Mar07]
^{208}Pb	$Q(2_1^+)^b$	$-0.7(3)^b \text{ eb}$	$\langle 2_1^+ E2 2_1^+ \rangle^b$	$-0.53(23)^b \text{ eb}$	[Mar07]

^a Very recent high precision measurement. Calculations will be performed with both $B(E2)$.

^b The $Q(2_1^+)$ in ^{208}Pb was left as a free parameter and the experimental data not used.

a new high precision value of the $B(E2; 2_1^+ \rightarrow 0_1^+)$ in ^{12}C was published during the writing of the present dissertation [D'A20]. Results using both the new $B(E2)$ value [D'A20] and the one from the most recent evaluation [Pri16] will be provided in the subsequent stages of the analysis.

4.4.2 Nuclear polarizability

As discussed in section 2.2.5, the virtual excitations via the Giant Dipole Resonance are another second-order effect accompanying the nuclear reorientation that may be measurable and can pose an additional challenge when measuring quadrupole moments, especially in the case of light nuclei. In this sense, a certain excited state can be populated not through a single-step direct excitation, but through a higher-step excitation via the GDR. These types of events must be excluded from the measurement of the cross section, so as not to bias the extracted value of the quadrupole moment.

The probability of a certain state being excited through the GDR is expressed in terms of the (-2) moment of the total photo-absorption cross section (σ_{-2}). This

cross section can be correctly estimated by the hydrodynamic model for the heavier regions of the nuclear chart, however for lighter nuclei, one relies on experimental information, which is very scarce. The most featured compilation of photo-neutron cross section data was evaluated by Dietrich and Berman in 1988 [Die88] and is currently under question. A recent review on nuclear polarizability effects and the present availability of experimental data is found in [Orc20].

The value of σ_{-2} can be introduced in GOSIA2 by means of the polarizability constant k (equation 2.41), and due to the scarce experimental data available in this property, the final extracted $Q(2_1^+)$ in ^{12}C will be expressed as a function of the σ_{-2} (or k) for any later measurements of this cross section taking place in the future. Nevertheless, there is some data on the total photoabsorption cross section for ^{12}C . The compilation by Dietrich and Berman includes only (γ, n) cross section data, which for the case of ^{12}C does not constitute a main contribution to the total cross section. However, Ahrens and collaborators [Ahr75] measured with high precision the total photo-absorption cross section for ^{12}C using thick targets. The main limitation in this type of experiments is that the atomic background for the measurement needs to be calculated also very precisely. In principle this can be achieved in light nuclei, therefore the value of the σ_{-2} cross section measured by [Ahr75] will be used to quote the final results for the $Q(2_1^+)$ for the present work.

In addition, the total photo-absorption cross section measured by Ahrens and collaborators yields a value of the nuclear polarizability constant of $k = 1.435(27)$ ($\sigma_{-2} = 316(5)\mu\text{b}/\text{MeV}$), which is in agreement with $k = 1.5(1)$ obtained by recent NCSM calculations using the chiral NN+3NF350 interaction [Raj18], (using Levinger's formula, equation 2.41). This further supports the use of the above mentioned value of σ_{-2} .

4.4.3 Fitting procedure

The use of GOSIA2 avoids introducing free parameters or normalisation constants that would normally become additional sources of systematic error, e.g. uncertainty in the integrated beam current or in the measured Rutherford-scattering cross section. The code handles the simultaneous analysis of both target and projectile excitation by minimising the χ^2 function (equation 2.47) in parallel for both nuclei — χ_{P}^2 and χ_{T}^2 — whilst sharing some common normalisation constants as parameters across both functions. These normalisation constants are calculated by making use of a “reference” normalisation transition in the target, the 3_1^- in ^{208}Pb , and they vary during the minimisation process. During the stage of fitting of the matrix elements, GOSIA2 switches between the two projectile and target input files resulting in a correlated set of matrix elements that best reproduces the observed γ -ray yields. The solution then will correspond to the global minimum of the χ_{total}^2 function, which is defined as the sum of the χ^2 for the projectile and target as

$$\chi_{\text{total}}^2 = N_{\text{P}} \chi_{\text{P}}^2 + N_{\text{T}} \chi_{\text{T}}^2, \quad (4.17)$$

where N_{P} and N_{T} stand for the number of projectile and target data. This is the sum of the number of γ -ray yields plus the number of spectroscopic data points introduced in GOSIA2.

The fitting of the matrix elements follows a least-squares search which gives the user the possibility of switching between different features during the minimisation. Among these, the user can choose to use the fast approximation method or the full Coulomb excitation formalism (the first speeds up the computation time), the steepest-descent minimisation or a gradient-plus-derivative method, or choose between using absolute or relative changes in the matrix elements to improve the minimum. The details of the different minimisation options and the numerical aspects can be found in the GOSIA manual [Czo83].

4.4.4 χ^2 map

The correlated and uncorrelated uncertainties in the fitted matrix elements can be evaluated by constructing a χ^2 hypersurface with respect to all parameters [Zie16]. In the case of the 2_1^+ in ^{12}C , the excitation process can be described as a function of two parameters: the transitional $\langle 2_1^+ || E2 || 0_1^+ \rangle$ and diagonal $\langle 2_1^+ || E2 || 2_1^+ \rangle$ matrix elements. As a result, the χ^2 hypersurface can be simplified to a 2-dimensional χ^2 surface where the transitional and diagonal matrix elements can be scanned until finding the best solution at χ_{\min}^2 . The uncertainties on the matrix elements can be found by extracting the 1σ contour, which is defined as the region of the surface where $\chi^2 < \chi_{\min}^2 + 1$. The final error bars are obtained by projecting such 1σ contour on the respective axes.

Figure 4.24 shows the total χ^2 surface obtained with GOSIA2 with respect to the diagonal $\langle 2_1^+ || E2 || 2_1^+ \rangle$ and transitional $\langle 2_1^+ || E2 || 0_1^+ \rangle$ matrix elements in ^{12}C and its 1σ contour. At each point of the surface, the corresponding transitional and diagonal matrix elements were kept fixed and the remaining matrix elements in the projectile and target were fitted to find the lowest χ_{total}^2 (equation 4.17) for all other dimensions in the hypersurface at this point. The calculation was performed using the evaluated value for the $B(E2)$ from table 4.4, i.e. $B(E2; 0_1^+ \rightarrow 2_1^+) = 39.7(2.0) e^2\text{fm}^4$, the γ -ray yields from table 4.2 and a nuclear polarizability constant of $k = 1$. The projected 1σ uncertainties yield a value of the diagonal matrix element of $\langle 2_1^+ || E2 || 2_1^+ \rangle = 0.088_{-0.045}^{+0.041} e\text{b}$, which by using equation 1.15, corresponds to a value of the spectroscopic quadrupole moment of $Q(2_1^+) = 6.7_{-3.4}^{+3.1} e\text{fm}^2$. The solid lines in the figure correspond to the 1σ contour of the Coulomb excitation, i.e. the 1σ contour of the equivalent χ^2 that would be obtained without including the contribution of the known $B(E2)$ to the χ^2 . The dashed lines represent the 1σ uncertainty of the $B(E2)$.

Similarly, Figure 4.25 shows the total χ^2 surface generated with the γ -ray yields

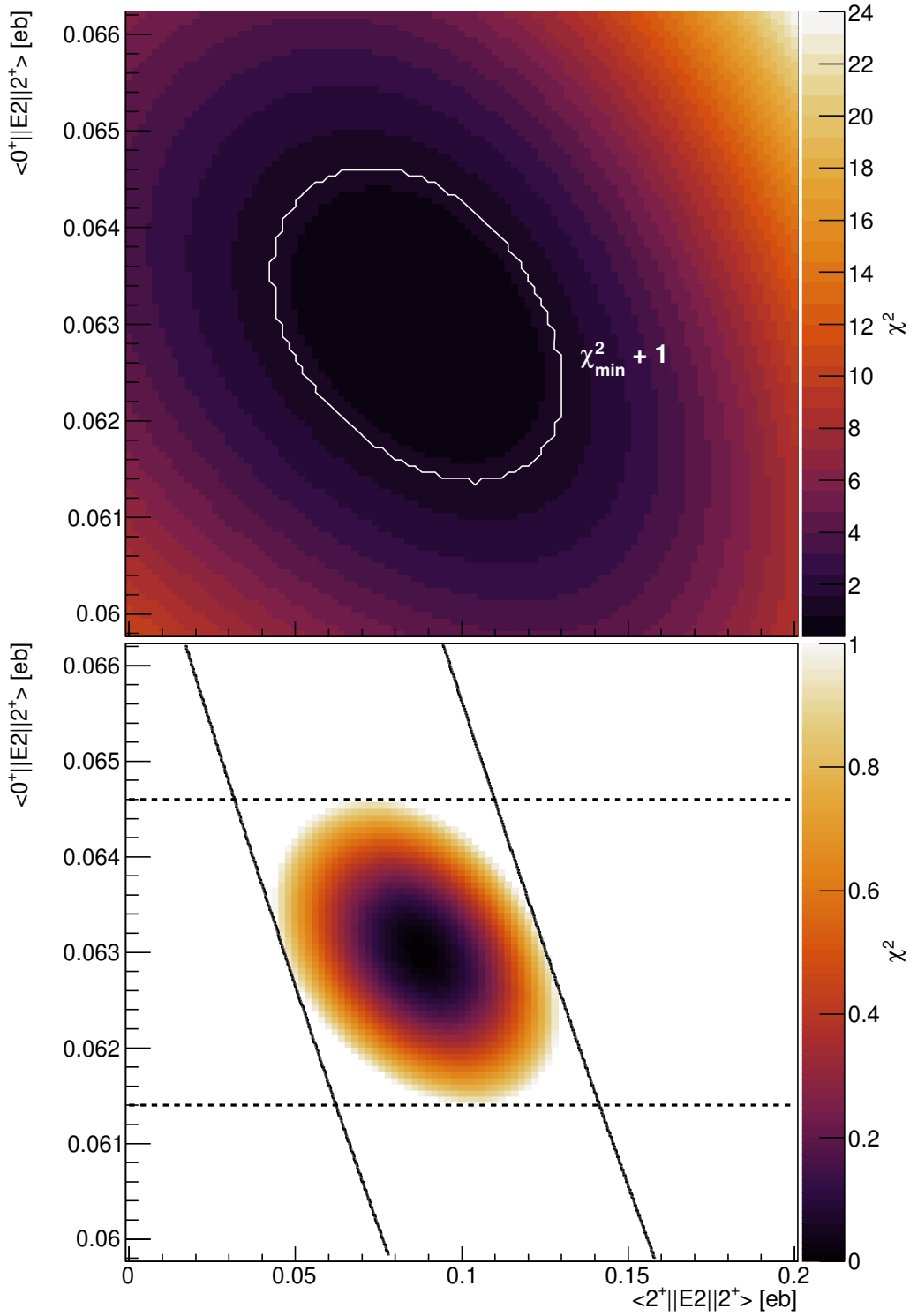


Figure 4.24: Two-dimensional total χ^2 surface obtained with GOSIA2 with respect to the diagonal $\langle 2_1^+ || E2 || 2_1^+ \rangle$ and transitional $\langle 2_1^+ || E2 || 0_1^+ \rangle$ matrix elements in ^{12}C (top) and its 1σ contour (bottom). The solid and dashed lines correspond to the 1σ contours of the Coulomb excitation and lifetime data [Pri16], respectively.

from table 4.2 and a nuclear polarizability constant of $k = 1$, but using the new high-precision $B(E2)$ value from table 4.4 ($B(E2; 2_1^+ \rightarrow 0_1^+) = 7.63(19) e^2 \text{fm}^4$). The χ_{min}^2 with projected 1σ uncertainties yields a value of the diagonal matrix element of $\langle 2_1^+ || E2 || 2_1^+ \rangle = 0.100_{-0.043}^{+0.039} \text{eb}$, which corresponds to a value of the spectroscopic quadrupole moment of $Q(2_1^+) = 7.6_{-3.3}^{+3.0} \text{efm}^2$. This new measurement of the $B(E2)$ has a reduced uncertainty of around a factor 2 compared to the value from the most recent evaluation. However, the uncertainty in the extracted quadrupole moment was only reduced by about 0.1efm^2 . The reason behind this lies in the fact the uncertainty in the number of counts is the main contributing factor to the error in the extracted $Q(2_1^+)$. The high sensitivity to the reorientation effect at backward scattering angles makes the final result highly sensitive to the uncertainty in the γ -ray yields. Unfortunately, due to the unexpected high-energy background discussed in section 4.2, the uncertainty in the extracted γ -ray yield makes the uncertainty in the extracted value of the quadrupole moment proportionately even larger.

The above quoted uncertainties in the $Q(2_1^+)$ moments include the error in all γ -ray yields and all propagated uncertainties from the spectroscopic data included in the χ^2 minimisation. This method accounts for all correlated and uncorrelated uncertainties in the fitting of the matrix elements in the projectile and in the target. The contribution of other parameters or factors such as the nuclear polarizability or the nuclear interference corrections will not change the size of the 1σ contours of Figures 4.24 and 4.25, as their effect is systematic and will only shift the position of the χ_{min}^2 in the $\langle 2_1^+ || E2 || 2_1^+ \rangle$ - $\langle 2_1^+ || E2 || 0_1^+ \rangle$ plane. The remaining potential sources of systematic uncertainty will be discussed in the following section (4.4.5) and the final results will be presented in section 4.5.

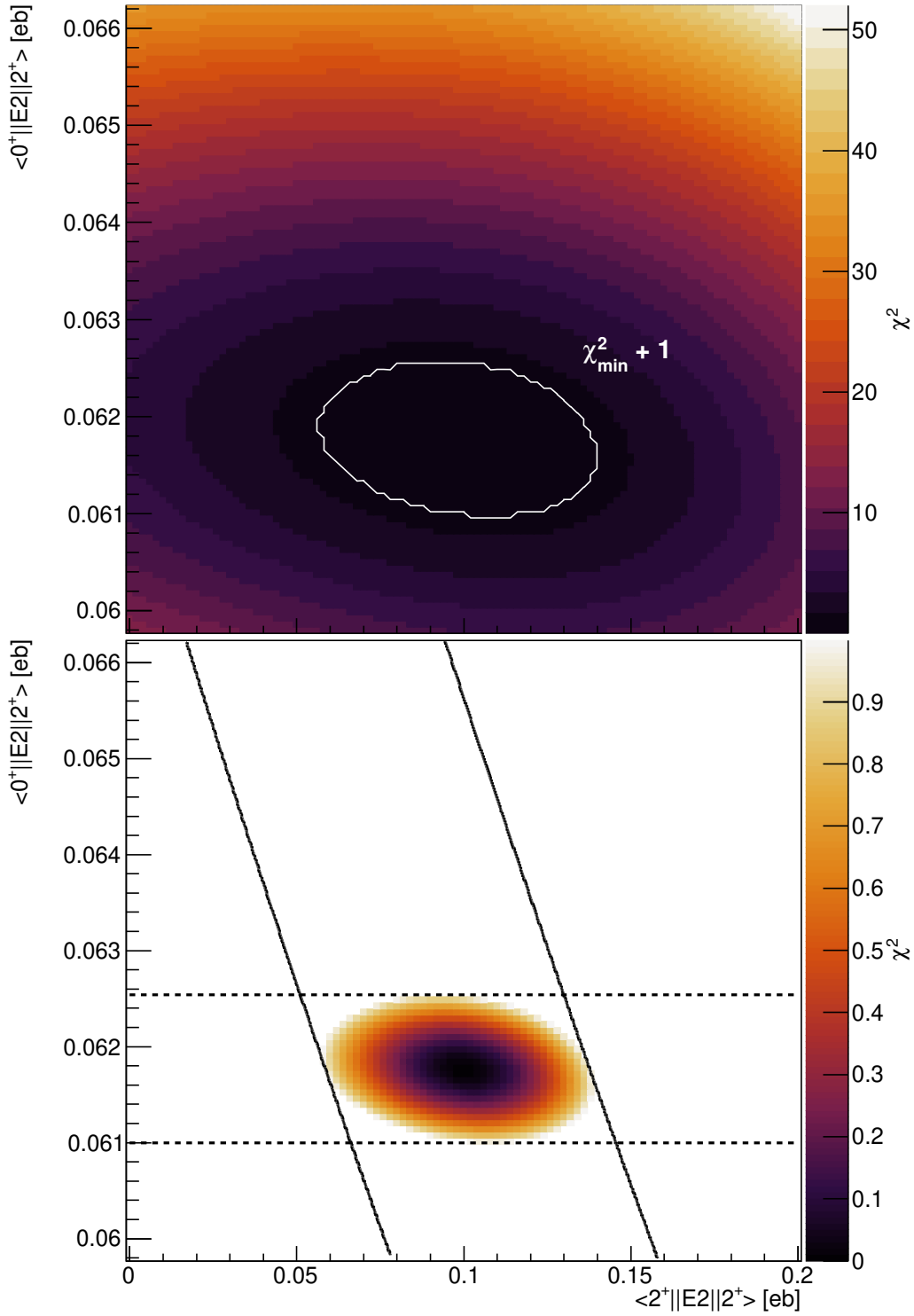


Figure 4.25: Two-dimensional total χ^2 surface obtained with GOSIA2 with respect to the diagonal $\langle 2_1^+ || E2 || 2_1^+ \rangle$ and transitional $\langle 2_1^+ || E2 || 0_1^+ \rangle$ matrix elements in ^{12}C (top) and its 1σ contour (bottom). The solid and dashed lines correspond to the 1σ contours of the Coulomb excitation and lifetime data [D'A20], respectively.

4.4.5 Other systematic uncertainties

In most cases, there is no simple relationship between the measured matrix elements and the experimental factors that can introduce potential sources of systematic uncertainty. Consequently, the effect of such factors in the final result needs to be investigated explicitly by varying the different experimental parameters and observing the changes in the extracted quadrupole moment.

The main source of systematic uncertainty that was found to have an appreciable effect on the final result was that which arose from the uncertainty in the beam energy centroid ($\pm 0.1\%$). In order to make sure that there is no systematic uncertainty unaccounted for, a more conservative value $\pm 0.2\%$ error in the beam energy centroid was considered. Different incoming beam energies were tested varying from 47.555 to 47.745 MeV ($47.65 - 0.2\%$ to $47.65 + 0.2\%$) finding a maximum shift in the extracted $Q(2_1^+)$ of $\pm 0.35 \text{ efm}^2$. A final systematic uncertainty of $\pm 0.4 \text{ efm}^2$ was added to the final result.

Furthermore, the energy loss of the incoming beam in the target is already accounted for by GOSIA through the integration of the Coulomb excitation cross section over the whole energy range. However, different targets were used throughout the experiment with thicknesses ranging from 294 to 314 $\mu\text{g}/\text{cm}^2$. The different energy losses for the different target thicknesses were explored yielding differences in the exit beam energy of $\pm 0.02\%$, which had a negligible impact in the extracted final result. In addition, the effect of the different number of reaction centres arising from the different target thicknesses balances out by the normalisation to the target excitation.

Furthermore, the hyperfine interaction of the excited nuclei recoiling in vacuum, known as the deorientation effect, can perturb the γ -ray angular distribution of the different excited states. However, the latter depends sensitively on the lifetimes of the different excited states. In GOSIA, the deorientation effect is modelled within

the framework of the Brenn and Spehl two-state model of the hyperfine interaction, which has been shown to give reasonable predictions [Czo83]. Due to its longer lifetime, the 3_1^- in ^{208}Pb suffers from some γ -ray angular distribution attenuation, in contrast to the relatively short-lived 2_1^+ states in ^{12}C and ^{208}Pb , which do not experience any.

The γ -ray yield of the 3_1^- state in ^{208}Pb was obtained for each of the JUROGAMII rings. The different values of the g -factor parameter of the two-state model were investigated in order to reproduce the observed γ -ray angular distribution whilst keeping the rest of the parameters fixed at their default values. By default, GOSIA assumes a g -factor of Z/A , however this factor was modified until obtaining the γ -ray angular distribution that better reproduced the experimental yields. The optimal g -factor was found to be $g = 0.36$. Figure 4.26 shows the 3_1^- γ -ray yield for each ring (each θ_γ) and the different relative γ -ray angular distributions obtained with GOSIA in the cases of the default g -factor, optimal g -factor and no deorientation considered. The effect that the different angular distributions had in the extracted $Q(2_1^+)$ was investigated and the extracted quadrupole moments did not change for all cases. Consequently, the impact of the nuclear deorientation on the final result was considered negligible as the large solid-angle coverage of the JUROGAMII array mitigates the effects.

Other investigated sources of systematic error include:

- The kinematic transformation from the laboratory to centre-of-mass frame of reference depends on the Q -value of the inelastic reaction, or equivalently the energy of the excited state. GOSIA can only use a single Q -value for the calculation of the cross sections for each collision partner. In our calculations the values of the 2_1^+ in ^{12}C and the 3_1^- in ^{208}Pb were used. As a result, the scattering angle, and therefore the cross section, corresponding to the 2_1^+ in ^{208}Pb will be calculated incorrectly. The magnitude of the error in the cross section for this state was investigated by performing calculations with GOSIA

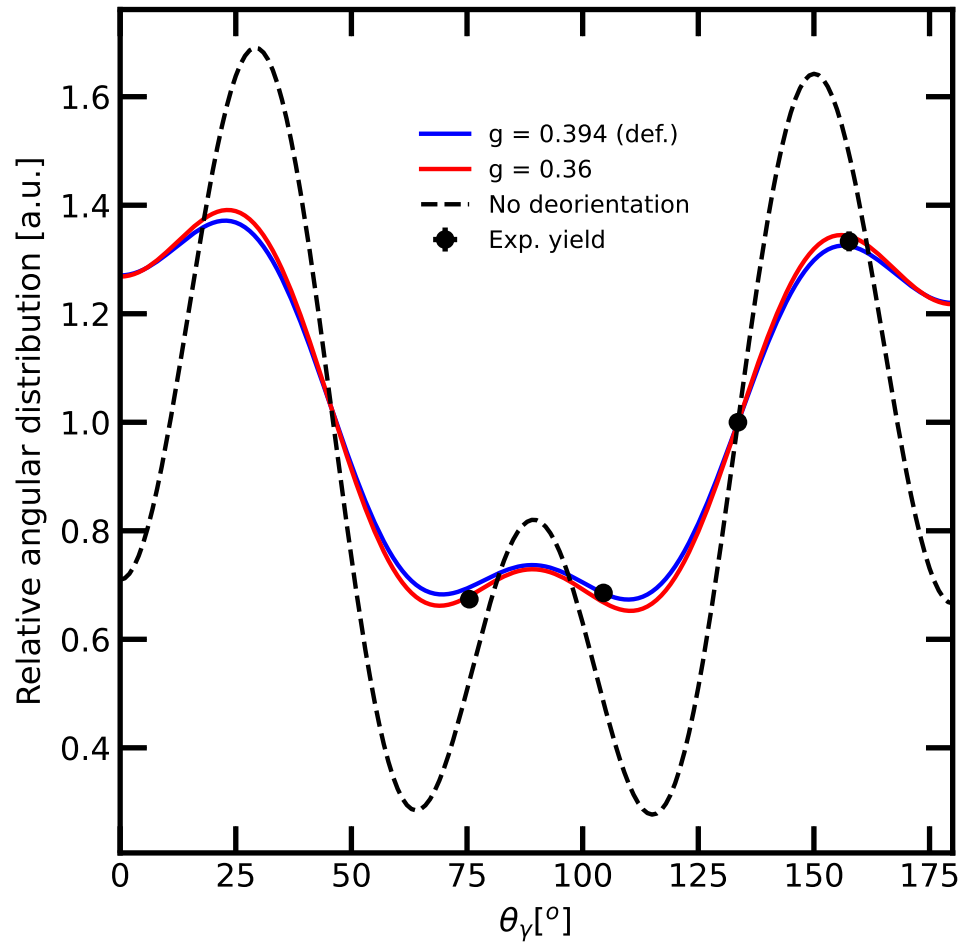


Figure 4.26: Relative γ -ray angular distribution of the 3_1^- state in ^{208}Pb normalised to the yield of the JUROGAMII ring 2 ($\theta = 133.57^\circ$) for different values of the g -factor.

and was found to be 1.5%. Nevertheless, this cross section does not have a severe effect on the final extracted $Q(2_1^+)$ in ^{12}C , and the error inferred by it was found to be negligible. In general, the error in the scattering angle is only significant for cases where there are large differences in excited-state energies of the order of several MeV.

- The effect of higher-lying excited states to the virtual 0_2^+ in ^{12}C , already included in the analysis, as well as the impact of higher-lying excited states in the target were investigated and also found to have no effect in the final extracted result.
- The accuracy of the semi-classical approximation was explored by calculating the pure Coulomb excitation cross section both with GOSIA and comparing it to the fully quantal code PTOLEMY. The ratio between the integrated cross sections was found to differ by $< 0.5\%$, therefore this effect was considered negligible.
- Other factors such as mutual excitations of projectile and target, slight perturbations in the Rutherford trajectory by atomic screening, vacuum polarization and relativistic effects have a minimal effect on the extracted matrix elements [Czo83].
- Uncertainties arising from the lack of cylindrical symmetry of the clover detectors, the positioning and size of the different crystals of the JUROGAMII array and the positioning of the SiCD detector within the target chamber also do not contribute significantly to the final result.

In summary, all potential sources of systematic uncertainty were investigated, and it was found that only the uncertainty in the beam-energy centroid had an effect on the final result for the present experiment ($\pm 0.35 \text{ efm}^2$). Therefore, this uncertainty alone will be added to the final results in section 4.5.

4.5 Results

Figures 4.27 and 4.28 show the final result for the extracted $Q(2_1^+)$ in ^{12}C for the evaluated [Pri16] and most recent [D'A20] $B(E2)$ values respectively (dark green lines). The resulting $Q(2_1^+)$ is displayed as a function of the nuclear polarizability constant k or analogously the total photo-absorption cross section σ_{-2} . The shaded area in the graph corresponds to the final uncertainties, which include not only the 1σ contour projections from χ^2 surface maps, but also the $\pm 0.4 \text{ efm}^2$ systematic error from the uncertainty in the beam energy. The values of the nuclear polarizability constant $k = 1$, which correspond to the σ_{-2} value predicted by the hydrodynamic model, and $k = 1.435(27)$, from the measurement of Ahrens and collaborators [Ahr75], are indicated in the figure as vertical shadowed regions in red and orange respectively. The quadrupole moment corresponding to those values of k can be found as the intersection of the above mentioned regions with the dark green line.

Table 4.5: Obtained result for the $Q(2_1^+)$ in ^{12}C for the different available $B(E2)$ values, nuclear polarizability constants of $k = 1$ and $k = 1.435(27)$, and with and without Coulomb-nuclear interference. The Coulomb-nuclear interference was estimated using the parameters from [Rob93].

$Q(2_1^+)$ [efm^2]	k	σ_{-2} [$\mu\text{b}/\text{MeV}$]	$B(E2) \uparrow$ [$e^2\text{fm}^4$]	CN Interf.
$6.7_{-3.8}^{+3.5}$	1	220	39.7(2.0)	No
$8.4_{-3.9}^{+3.6}$	1.435(27)	316(5)	39.7(2.0)	No
$7.6_{-3.7}^{+3.4}$	1	220	38.15(95)	No
$9.3_{-3.8}^{+3.5}$	1.435(27)	316(5)	38.15(95)	No
$9.3_{-3.8}^{+3.5}$	1	220	39.7(2.0)	Yes
$11.1_{-3.9}^{+3.6}$	1.435(27)	316(5)	39.7(2.0)	Yes
$10.2_{-3.7}^{+3.4}$	1	220	38.15(95)	Yes
$12.0_{-3.8}^{+3.5}$	1.435(27)	316(5)	38.15(95)	Yes

Table 4.5 contains the final results of the $Q(2_1^+)$ in ^{12}C from figures 4.27 and 4.28 for the quoted values of the nuclear polarizability constant. The effect of a correction factor given by the DWBA analysis using the parameters from Robson *et al.* (see figures 4.20, 4.21 and 4.22) is also included in the bottom half of the table. It should be noted that the uncertainty in the $Q(2_1^+)$ for the case of $k = 1.435(27)$ is slightly larger since it accounts for the uncertainty in the measured value of σ_{-2} .

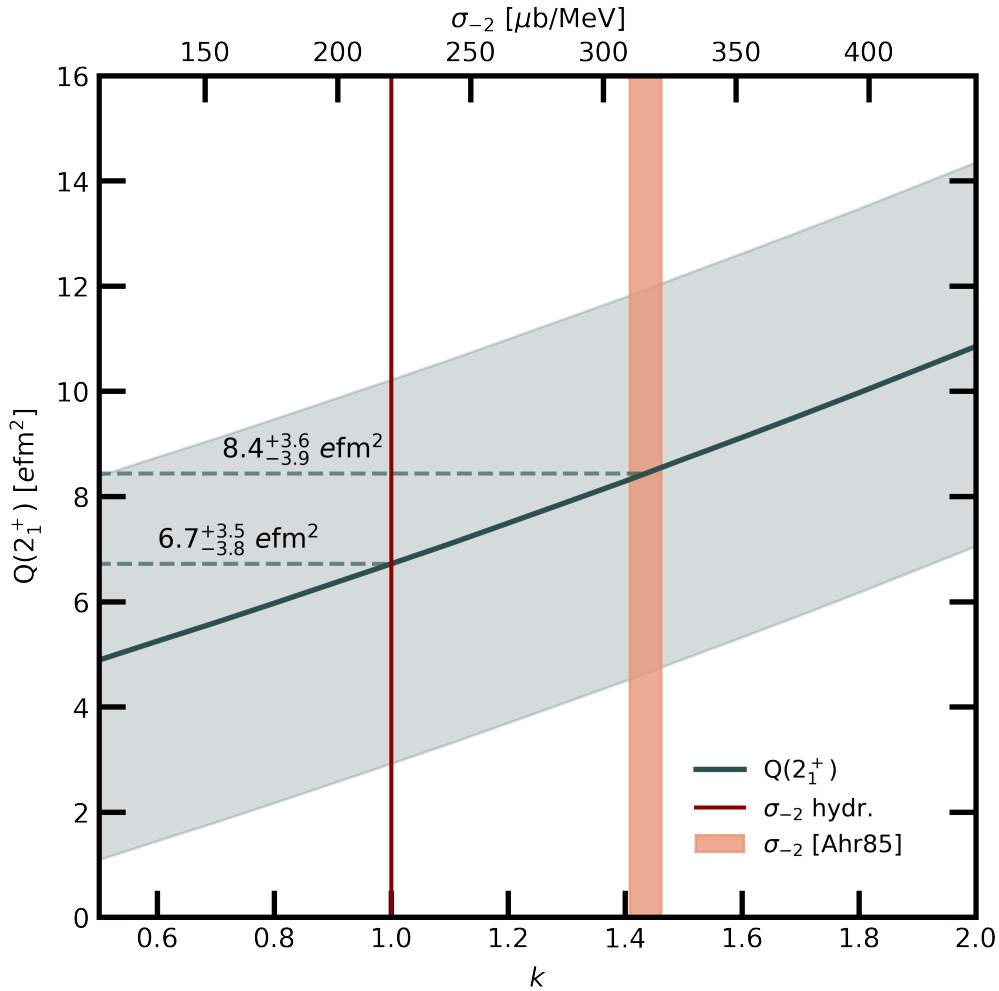


Figure 4.27: Extracted $Q(2_1^+)$ (dark green line) from the GOSIA2 fit to the experimental γ -ray yields from table 4.2 as a function of the nuclear polarizability constant k (total photo-absorption cross section σ_{-2}) using the evaluated value of the $B(E2)$ from [Pri16]. The uncertainties on the final result are represented as the shaded grey area in the figure. The values of the nuclear polarizability constant $k = 1$ and $k = 1.435(27)$ are also indicated.

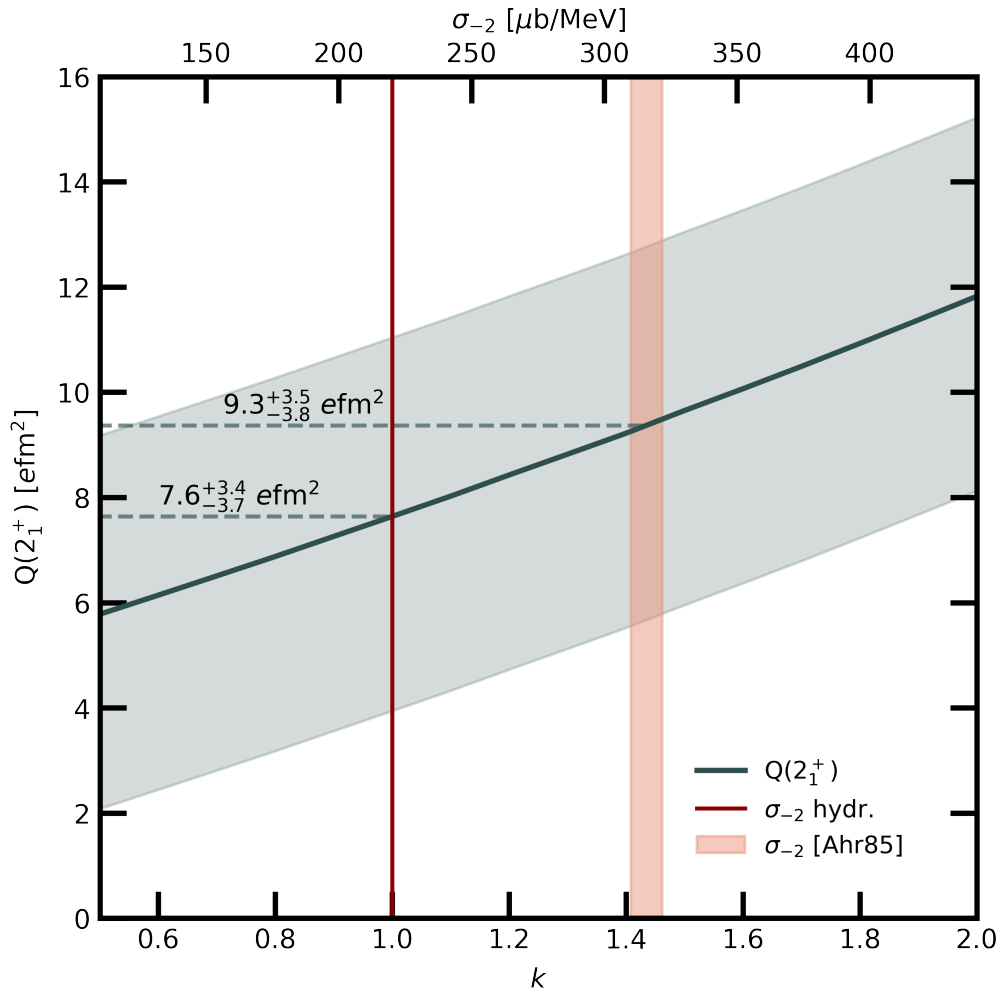


Figure 4.28: Extracted $Q(2_1^+)$ (dark green line) from the GOSIA2 fit to the experimental γ -ray yields from table 4.2 as a function of the nuclear polarizability constant k (total photo-absorption cross section σ_{-2}) using the new high precision value of the $B(E2)$ from [D'A20]. The uncertainties on the final result are represented as the shaded grey area in the figure. The values of the nuclear polarizability constant $k = 1$ and $k = 1.435(27)$ are also indicated.

Chapter 5

Discussion and Conclusions

This chapter will begin with a short revision of the previous measurements of the $Q(2_1^+)$ in ^{12}C , which will include new values of the $Q(2_1^+)$ updated to the most recent $B(E2)$ values and nuclear polarizability constant data. Subsequently, a comparison of the obtained results in this work with the updated values and recent theory calculations will be discussed. Finally, the conclusions will be presented.

5.1 Revision of previous experimental results

The previous experimental measurements of the $Q(2_1^+)$ were briefly presented in section 1.5.3. Nevertheless, a revision of these measurements is essential in order to compare and understand the impact of the experimental results presented in this thesis.

The only two reorientation effect measurements of the 2_1^+ in ^{12}C have been the experiments by Vermeer [Ver83] and Kumar Raju [Raj18] and collaborators. In Vermeer's work, the inelastically scattered ^{12}C ions by a ^{208}Pb target were momentum analyzed using a magnetic spectrometer and detected at the focal plane using a position sensitive multi-wire proportional counter placed at a scattering angle of $\theta = 90^\circ$ in the laboratory frame. Using the adopted value of $B(E2; 0_1^+ \rightarrow 2_1^+) = 38.8(2.2) e^2\text{fm}^4$ at the time and considering a nuclear polarizability constant of $k = 1$ (using

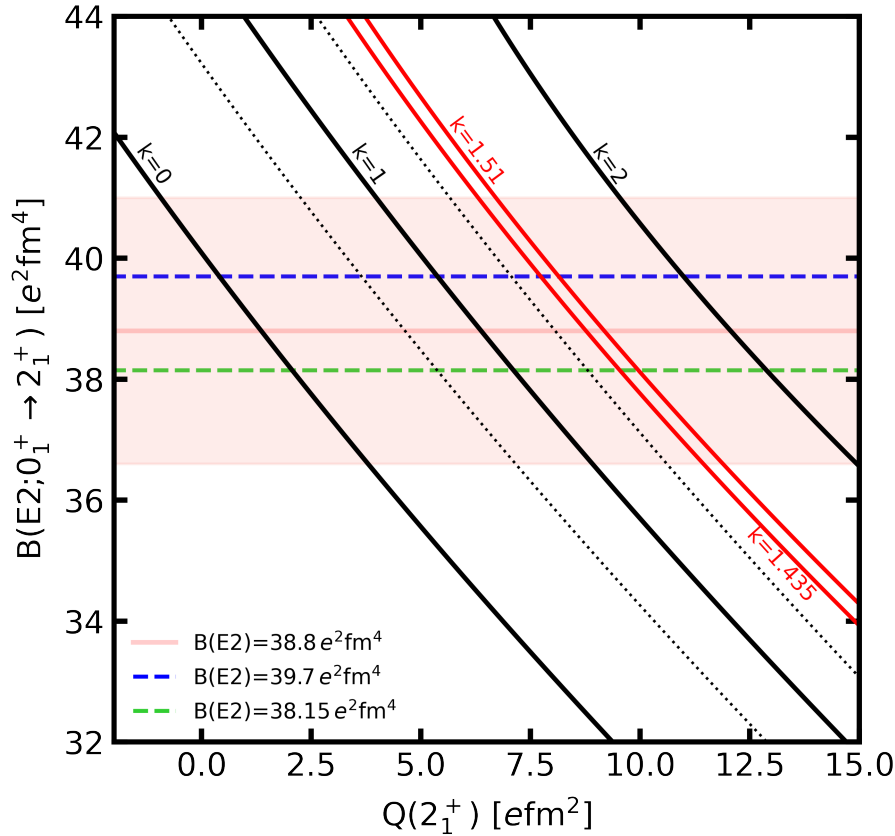


Figure 5.1: Coulomb excitation curves extracted from [Ver83] for different values of the nuclear polarizability constant k (solid black lines) and interpolated for $k = 1.435, 1.51$ (solid red lines). The dashed black lines represent the statistical uncertainty of 1σ obtained for $k = 1$. The $B(E2)$ value used to extract the final result and its uncertainty are displayed as a solid horizontal pink line and shaded pink area. Finally, the currently adopted and most recent higher-precision $B(E2)$ values, [Pri16] and [D'A20] respectively, are displayed as dashed horizontal lines.

Levinger's formula), their experiment yielded a value of the $Q(2_1^+)$ of $6 \pm 3 \text{efm}^2$ (Figure 5.1). The statistical uncertainty of $\pm 1.7 \text{efm}^2$ and the error due to the uncertainty in the value of the $B(E2)$ ($\pm 2.3 \text{efm}^2$) added in quadrature yield their quoted final uncertainty of 3efm^2 .

In contrast, in the Coulomb excitation experiment by Kumar Raju and collaborators, a ^{12}C beam impinging on a ^{194}Pt target was used to Coulomb-excite the 2_1^+ state in ^{12}C and measure the scattered ^{12}C ions at $\theta = 30^\circ - 60^\circ$ in coincidence with the de-exciting γ -rays from both projectile and target. Using the currently adopted

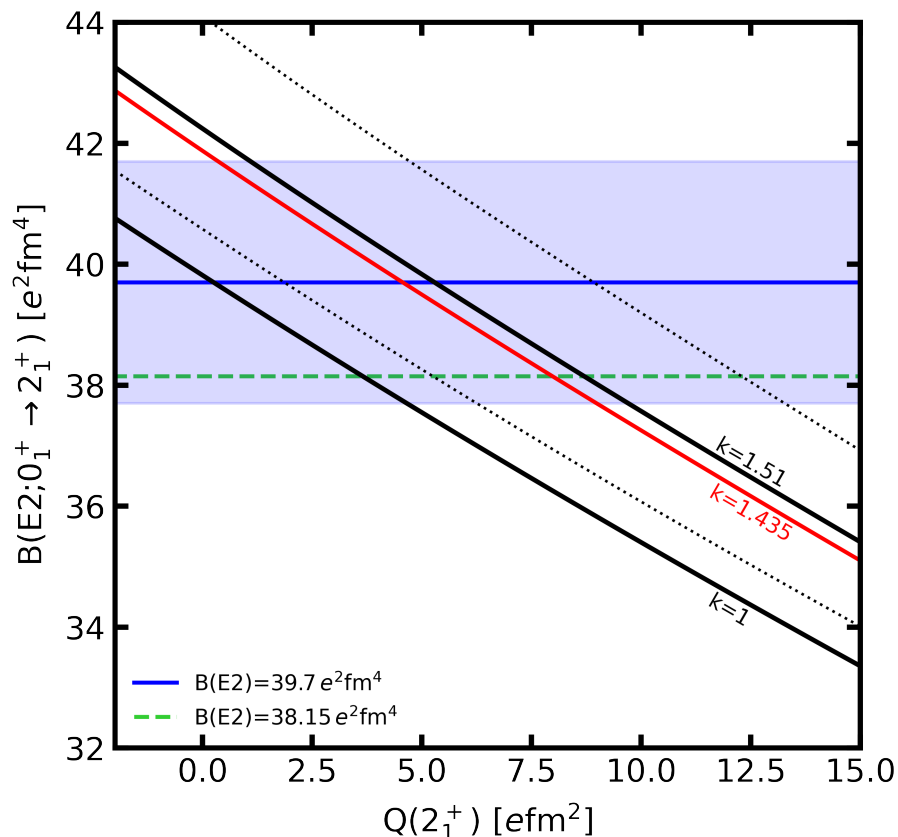


Figure 5.2: Coulomb excitation curves extracted from [Raj18] for different values of the nuclear polarizability constant k (solid black lines) and interpolated for $k = 1.435$ (solid red line). The dashed black lines represent the statistical uncertainty of 1σ obtained for $k = 1.51$. The currently adopted value of the $B(E2)$ [Pri16] used to extract the final result and its uncertainty are displayed as a solid horizontal blue line and shaded blue area. The most recent higher-precision $B(E2)$ value from [D'A20] is also displayed as a dashed horizontal line.

value of the $B(E2) = 39.7(2.0) e^2 \text{fm}^4$, their reorientation effect measurement yielded a value of $Q(2_1^+) = 0.3 \pm 5.4 e \text{fm}^2$ with a nuclear polarizability constant of $k = 1$ (or $k = 1.46$ taking the formula of [Orc15]), or $Q(2_1^+) = 5.4 \pm 4.4 e \text{fm}^2$ with $k = 1.51(14)$ (or $k = 2.2(2)$ taking the formula of [Orc15]) from NCSM calculations using the chiral NN+3NF350 interaction (see Figure 5.2).

In order to compare the results obtained in the present work with these other two experiments, it is necessary to take into account that the measured Coulomb excitation cross section for the 2_1^+ in ^{12}C depends not only on the $Q(2_1^+)$, but also

on the $B(E2)$ and the nuclear polarizability constant. This means that it is only possible to correctly compare with the data from [Ver83] and [Raj18] for results extracted using the same $B(E2)$ value and the same nuclear polarizability constant. Figures 5.1 and 5.2 are an adaptation of the results obtained in the published work from [Ver83] and [Raj18]. In the plots, the resulting Coulomb excitation curves for different values of the nuclear polarizability constant are shown. When the curve for that specific value of k was directly provided in the paper, the line is plotted in black. When that was not the case ($k = 1.435$ and $k = 1.51$ for Vermeer's and $k = 1.435$ for Kumar Raju's data), the line was obtained by interpolating and is displayed in red. The dashed black lines in the figures represent the quoted 1σ statistical uncertainty for the values of $k = 1$ for Vermeer's data (Figure 5.1) and $k = 1.51$ for Kumar Raju's work (Figure 5.2). The solid horizontal lines and shaded areas in pink and blue show the $B(E2)$ used in each experiment to extract the quadrupole moment and its 1σ uncertainty. Finally, additional dashed lines showing the currently adopted value [Pri16] and new precision measurement [D'A20] of the $B(E2)$ are also displayed in the figures. The resulting quadrupole moment for each $B(E2)$ and each value of k will therefore correspond to the intersection of the before mentioned Coulomb excitation curves with the horizontal $B(E2)$ lines. The resulting quadrupole moments for $k = 1, 1.435, 1.51$ and $B(E2) = 39.7(2.0), 38.15(95) e^2\text{fm}^4$ are displayed in table 5.1 together with the results obtained for the present work.

Table 5.1: Obtained result for the $Q(2_1^+)$ in ^{12}C using the data from [Ver83] and [Raj18], and the present work for values of the nuclear polarizability constant of $k = 1, 1.435, 1.51$ and $B(E2) = 39.7(2.0), 38.15(95) e^2\text{fm}^4$.

$Q(2_1^+)$ [efm ²]	k	$B(E2) \uparrow$ [e ² fm ⁴]	Reference
5.4(3.0)	1	39.7(2.0)	[Ver83]
7.8(3.0)	1.435(27)	39.7(2.0)	[Ver83]
8.2(3.0)	1.51(14)	39.7(2.0)	[Ver83]
7.1(2.0)	1	38.15(95)	[Ver83]
9.5(2.0)	1.435(27)	38.15(95)	[Ver83]
9.9(2.0)	1.51(14)	38.15(95)	[Ver83]
0.3(5.4)	1	39.7(2.0)	[Raj18]
4.6(4.4)	1.435(27)	39.7(2.0)	[Raj18]
5.3(4.4)	1.51(14)	39.7(2.0)	[Raj18]
3.6(4.4)	1	38.15(95)	[Raj18]
7.9(4.4)	1.435(27)	38.15(95)	[Raj18]
8.7(4.4)	1.51(14)	38.15(95)	[Raj18]
$6.7_{-3.8}^{+3.5}$	1	39.7(2.0)	This work
$8.4_{-3.9}^{+3.6}$	1.435(27)	39.7(2.0)	This work
$8.7_{-4.0}^{+3.7}$	1.51(14)	39.7(2.0)	This work
$7.6_{-3.7}^{+3.4}$	1	38.15(95)	This work
$9.3_{-3.8}^{+3.5}$	1.435(27)	38.15(95)	This work
$9.6_{-3.9}^{+3.6}$	1.51(14)	38.15(95)	This work

5.2 Comparison with previous experiments

Figure 5.3 shows the obtained result for the $Q(2_1^+)$ in ^{12}C in the present work together with the values obtained from the data from [Ver83] and [Raj18] (table 5.1). As it can be seen there is a substantial agreement between the experimental results from [Ver83] for all values of the nuclear polarizability and $B(E2)$. On the other hand, the experimental result by [Raj18] shows varying levels of agreement with this work depending on the adopted values of the k and $B(E2)$. The only instances where the values were more than 1σ apart were in the cases of $k = 1$ and $B(E2) = 39.7(2.0) e^2\text{fm}^4$. Conversely, for the case of higher k and smallest $B(E2)$, all three experiments show a remarkable agreement.

At this point, it is also important to appreciate the sensitivity of the Coulomb excitation cross section to the scattering angle. The three different experimental results displayed in Figure 5.3 were performed at scattering angles of $\theta_{\text{LAB}} = 30^\circ - 60^\circ$ [Raj18], $\theta_{\text{LAB}} = 90^\circ$ [Ver83] and $\theta_{\text{LAB}} = 158.8^\circ$ (this work). Section 2.2.4 discussed the ways in which the sensitivity to the reorientation effect is maximised at backward scattering angles. An enhanced sensitivity of the reorientation effect translates into a higher relative contribution of such effect to the Coulomb excitation cross section. Consequently, a reduced sensitivity to the reorientation will result in the extracted value of the $Q(2_1^+)$ exhibiting a higher sensitivity to the other observables controlling the other excitation paths of the 2_1^+ , namely the $B(E2)$ (one-step excitation) and, to a lesser extent, the nuclear polarizability constant (two-step excitation). As a result, assuming the same statistical uncertainty, the error bars in the extracted $Q(2_1^+)$ will be larger as the scattering angle decreases.

The picture described above can be observed in Figure 5.3, where the $Q(2_1^+)$ from [Raj18] shows the highest sensitivity to the $B(E2)$ and polarizability constant values used. The result by [Ver83] varies less significantly with the $B(E2)$, however the most stable result is the one presented in this work. Quantitatively, the sensitivity of

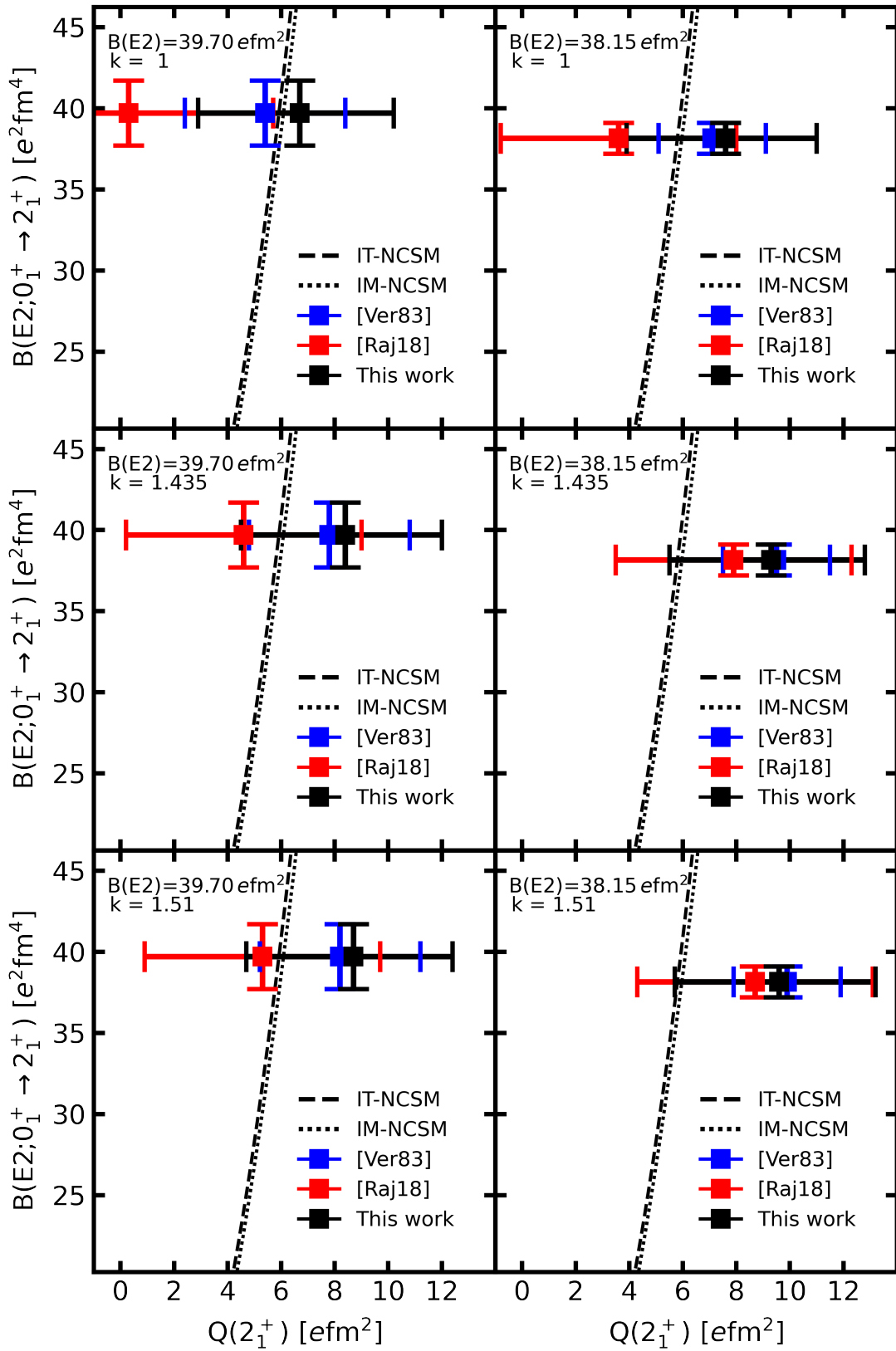


Figure 5.3: Comparison of the obtained $Q(2_1^+)$ in ^{12}C in this work together with the previous measurements of [Ver83] and [Raj18] for different values of the $B(E2; 0_1^+ \rightarrow 2_1^+)$ and nuclear polarizability constant k (table 5.1). The dashed and dotted curves represent the IT-NCSM and IM-NCSM correlation lines from Figures 1.4 and 1.5, respectively.

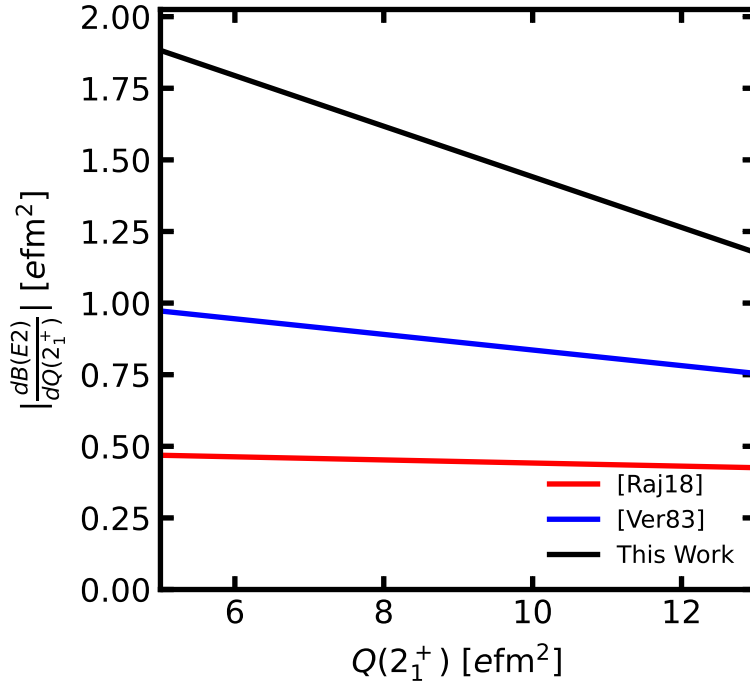


Figure 5.4: Absolute value of the derivative of the $B(E2)$ with respect to the $Q(2_1^+)$ for the different experiments by [Ver83] and [Raj18], and this work in the range of 5 to 13 efm^2 .

an experiment to the reorientation effect can be expressed in terms of the derivative of the $B(E2)$ with respect to the $Q(2_1^+)$. Figure 5.4 shows the absolute value of the derivative of the $B(E2)$ with respect to the $Q(2_1^+)$ for the different experiments in the range of 5 to 13 efm^2 . Once more, it can be seen how the present experiment is considerably more sensitive to the reorientation effect than the others — around 3 times more sensitive compared to the case of [Raj18] and around a factor of 2 in comparison with [Ver83]. Graphically, this can be interpreted in terms of the slopes of the Coulomb excitation curves in Figures 5.1 and 5.2, or alternatively, in terms of the x -component of the gradient — or “steepness” of the minimum — of the two-dimensional χ^2 surfaces computed in the more sophisticated analysis shown in this work in Figures 4.24 and 4.25. In general, this encourages the realisation of reorientation effect experiments at backward scattering angles.

5.3 Comparison with theory

In Figure 5.3, the correlation between quadrupole observables arising from the IT-NCSM and IM-NCSM calculations are also displayed. Thus far, three values of the nuclear polarizability constant have been considered, i.e. $k = 1, 1.435$ and 1.51 . However, the experiment from Ahrens *et al*, yielding $k = 1.435(27)$ [Ahr75], supported by recent NCSM calculations, $k = 1.51(14)$ [Raj18], encourages the use of this k as a reliable value of the nuclear polarizability constant. Therefore, the results for $k = 1.435(27)$, and $B(E2) = 39.7(2.0)$ and $38.15(95) e^2\text{fm}^4$ will be the ones to be compared with the latest *ab initio* calculations hereafter.

For the above mentioned values of the $B(E2)$ and k ($B(E2) = 39.7(2.0)$ and $38.15(95) e^2\text{fm}^4$, and $k = 1.435(27)$) all three experiments agree with each other within their 1σ uncertainty error bars. However, the result by [Raj18] has a large error arising from the low sensitivity to the reorientation effect at small scattering angles. This can be seen in the gradient of the Coulomb excitation curve presented in Figure 5.4. Consequently, since the experiment from [Ver83] constitutes the currently adopted value [Kel17], we will use this to compare with theory and yield our final result.

From Figure 5.3, $B(E2) = 39.7(2.0) e^2\text{fm}^4$ and $k = 1.435$, it can be observed that the *ab initio* correlation curves agree within error with this work's experimental result and the data extrapolated from [Ver83]. However, the central values of these two experimental data points consistently suggest a more pronounced oblate shape of the 2_1^+ in ^{12}C than that predicted by the theory, i.e. a larger spectroscopic quadrupole moment. In addition, the larger values of $Q(2_1^+)$ — and thus the disagreement with the NCSM calculations — become even more noticeable for the new value of the $B(E2) = 38.15(95) e^2\text{fm}^4$, where the reduced uncertainty in the $B(E2)$ systematically reduces the error bar from [Ver83] and leaves the data point considerably over 1σ apart from the theory predictions.

If we now consider the $Q(2_1^+)$ by Vermeer together with the data from the experiment presented in this dissertation, for $k = 1.435(27)$, the weighted average yields $Q(2_1^+) = 8.1(2.3) \text{ efm}^2$ for $B(E2) = 39.7(2.0) \text{ e}^2\text{fm}^4$ and $Q(2_1^+) = 9.5(1.8) \text{ efm}^2$ for the latest measurement of the $B(E2) = 38.15(95) \text{ e}^2\text{fm}^4$. Figure 5.5 shows these two results together with the IT-NCSM and IM-NCSM calculations of the $B(E2)$ and $Q(2_1^+)$ and the correlation curves (Figures 1.4 and 1.5 from section 1.5.2 combined). The predicted values of the $Q(2_1^+)$ by the different NCSM calculations, $Q(2_1^+) = 5.91(15) \text{ efm}^2$ for the IT-NCSM and $Q(2_1^+) = 5.97(30) \text{ efm}^2$ for the IM-NCSM, are only just within the error bars of this new experimental value of the $Q(2_1^+)$ using the adopted $B(E2)$ and almost 2σ apart for the result using the new $B(E2)$.

It can also be seen from Figure 5.5 that regardless of the interaction or many-body method used (IT or IM), the NCSM calculations can only reproduce values of the $Q(2_1^+) \lesssim 6.5 \text{ efm}^2$. In addition, Figure 5.6 shows a comparison between the obtained $Q(2_1^+)$ moments and different theoretical calculations of the same observable. As shown, it is only the calculation performed using Nuclear Lattice EFT at LO [Epe12] that can reproduce such larger values of the spectroscopic quadrupole moment.

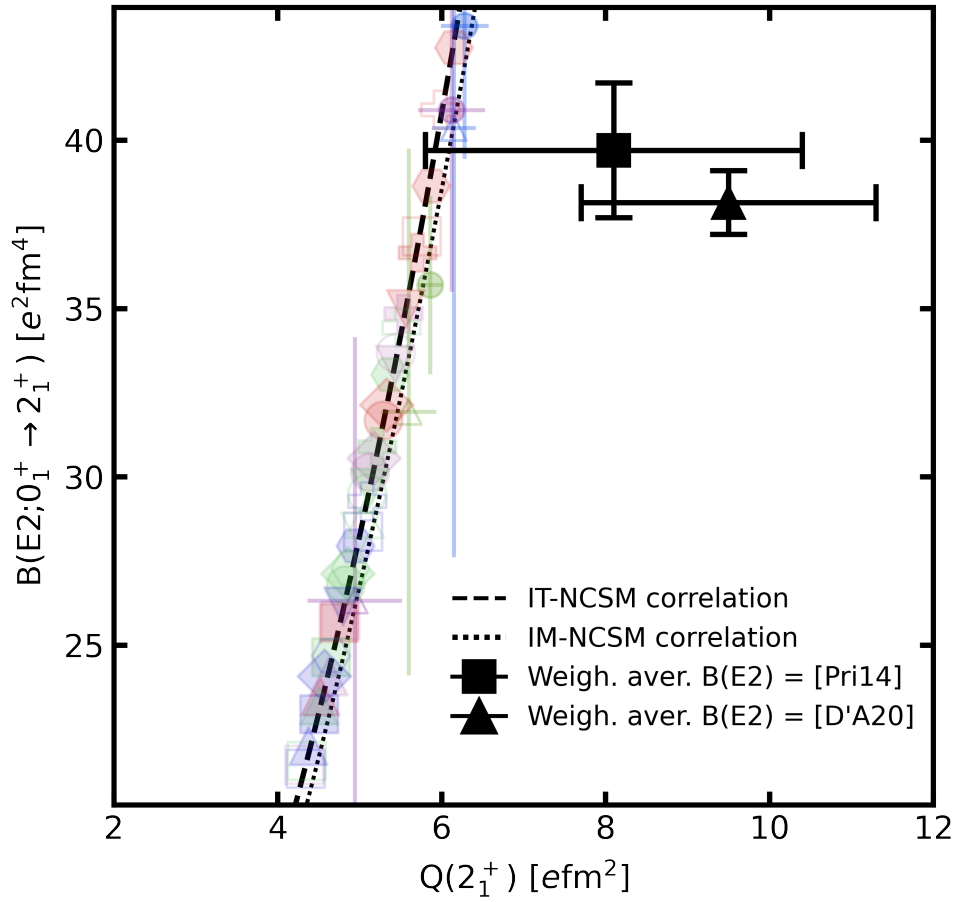


Figure 5.5: Weighted average of the $Q(2_1^+)$ measured by [Ver83] with the result extracted from this work for the two different available $B(E2)$ values. The ab initio IT-NCSM and IM-NCSM predictions for both quadrupole observables (Figures 1.4 and 1.5) are also shown.

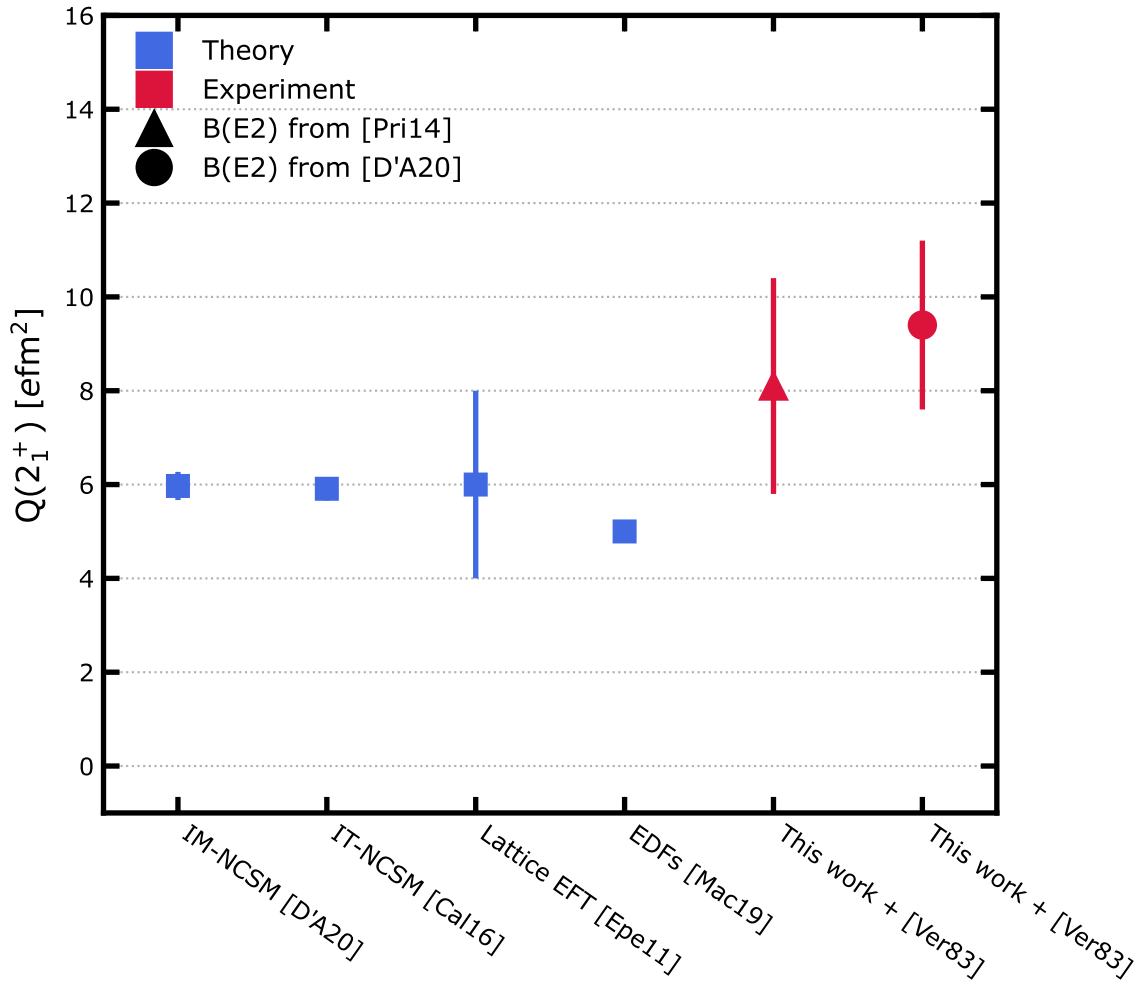


Figure 5.6: Different theoretical values (blue squares) for the $Q(2_1^+)$ in ^{12}C . From left to right: IM-NCSM and IT-NCSM using chiral NN+3N interactions [D'A20, Cal16], Nuclear Lattice EFT at LO [Epe12] and Global EDFs [Mac19]. The experimental results of this work averaged with the measurement from [Ver83] are also displayed (red symbols) for the evaluated value of the $B(E2)$ (triangle) and most recent measurement of the $B(E2)$ (circle).

5.4 Conclusion

This thesis presents the measurement of the quadrupole moment of the 2_1^+ in ^{12}C as a way of testing state-of-the-art nuclear structure theories. The measurement of the $Q(2_1^+)$ was successfully performed and the collected data was analysed. The aim of the experiment was to extract a value of this electromagnetic property with a reduced uncertainty to which it had been measured previously ($\pm 3 \text{ efm}^2$) by means of using the high sensitivity of the reorientation effect at backward scattering angles. The GOSIA analysis using a nuclear polarizability constant of $k = 1.435(27)$ from [Ahr75] yielded a final value of the $Q(2_1^+) = 8.4_{-3.9}^{+3.6} \text{ efm}^2$ for the currently evaluated value of the $B(E2) = 39.7(2.0) \text{ e}^2\text{fm}^4$ [Pri16] or $Q(2_1^+) = 9.3_{-3.8}^{+3.5} \text{ efm}^2$ using a more recent measurement of the $B(E2) = 38.15(95) \text{ e}^2\text{fm}^4$ [D'A20]. The main contribution to the final quoted error arose from the statistical uncertainty caused by an unexpected high-energy background in the measured γ -ray spectrum coming from $^{12}\text{C}+^{12}\text{C}$ reactions of the beam with the backing material in the target.

The currently adopted value for the $Q(2_1^+)$ — which uses an outdated value of the nuclear polarizability constant $k = 1$ and $B(E2)$ — was interpolated for $k = 1.435(27)$ and $B(E2)$ s from [Pri16] and [D'A20] using the data from Ref. [Ver83]. The extracted quadrupole moments were of $Q(2_1^+) = 7.8(3.0) \text{ efm}^2$ and $Q(2_1^+) = 9.5(2.0) \text{ efm}^2$ for the different $B(E2)$ values, respectively. The results from the present work are in excellent agreement with these two values. In addition, despite the final quoted uncertainty not being as small as expected, the weighted average of our experimental result with the interpolated data from Ref. [Ver83] yielded $Q(2_1^+) = 8.1(2.3) \text{ efm}^2$ and $Q(2_1^+) = 9.5(1.8) \text{ efm}^2$ for the $B(E2)$ s from [Pri16] and [D'A20] respectively. These two new values now have a significantly reduced uncertainty and provide benchmarks for *ab initio* calculations using chiral interactions.

IT-NCSM [Mar14] and IM-NCSM [D'A20] calculations of the reduced quadrupole transition strength $B(E2; 0_1^+ \rightarrow 2_1^+)$ and quadrupole moment for the 2_1^+ in ^{12}C using

chiral NN and NN+3N interactions have shown a strong and robust correlation between both E2 observables and a dependence on the underlying interaction and truncation of the model space. The lower end of the error bar of the value of $Q(2_1^+) = 8.1(2.3) \text{ efm}^2$ only just includes the NCSM calculations for the quadrupole moment whilst the result of $Q(2_1^+) = 9.5(1.8) \text{ efm}^2$ is almost 2σ apart from the theory predictions.

Other theoretical calculations predict values of the $Q(2_1^+)$ of the same order to those obtained by the NCSM. Of these, the calculation performed using Nuclear Lattice EFT at LO [Epe12] is the only one which can reproduce such large values of the quadrupole moment ($6(2) \text{ efm}^2$) similar to the experimental results described in this dissertation.

The possibility of the presence of Coulomb-nuclear interference has been investigated using DWBA calculations with different sets of optical potential parameters. Previous experimental work from [Ver83] suggests that there are not any Coulomb-nuclear interference effects in the present experiment. However, some DWBA calculations [Rob93] suggest an interference of around $\sim 12\%$ for the excitation cross section of the 2_1^+ in ^{12}C . The obtained quadrupole moments assuming such interference are $Q(2_1^+) = 11.1_{-3.9}^{+3.6} \text{ efm}^2$ and $Q(2_1^+) = 12.0_{-3.8}^{+3.5} \text{ efm}^2$ for the currently evaluated value and newest measurement of the $B(E2)$ respectively. These results point towards an even more pronounced oblate shape of ^{12}C on its 2_1^+ and therefore a more substantial disagreement with the different theoretical calculations.

In summary, the presented experimental results strongly suggest larger values of $Q(2_1^+)$ than those predicted by most *ab initio* methods and calls for additional and more accurate measurements of this electromagnetic property as well as a thorough revision of the underlying theory which aims to compute these observables.

5.5 Future work

Despite the improved precision obtained for the $Q(2_1^+)$ in ^{12}C through the weighted average of the measurement presented in this work and that of [Ver83], an increased accuracy in the determination of this electromagnetic property would be highly desirable. As previously discussed, the high sensitivity to the reorientation effect at backward scattering angles allows the measurement of such property with high precision. However, the high energy γ -ray background coming from $^{12}\text{C}+^{12}\text{C}$ reactions of the beam with the target backing material decreased the peak-to-background ratio in the observed photopeak, leading to an increased statistical uncertainty in the extracted γ -ray yield.

As a result, a new Coulomb excitation experiment [Pet20] has been proposed and accepted at the ATLAS facility in Argonne National Laboratory. In the experiment, a ^{208}Pb beam will impinge on a self-supporting ^{12}C target producing the Coulomb excitation of both projectile and target nuclei. A Si detector will be placed at center-of-mass angles $\sim 137^\circ - 165^\circ$ (laboratory angles: $7^\circ - 21^\circ$) to measure the recoiling target ions in coincidence with the de-exciting γ -rays, which will be measured with GREYINA. This new experiment will deliver for the first time a precise experimental value for the $Q(2_1^+)$ of ^{12}C ($\pm 1 \text{ efm}^2$) by taking advantage of:

- the superior γ -ray efficiency of GREYINA; 4.7% for 4.4 MeV γ -rays from GREYINA vs 1% of the JUROGAMII array,
- the high-precision measurement of the beam energy at ATLAS,
- and the measurement in inverse kinematics with a self-supporting ^{12}C target alleviating the background issue that was faced in the JYFL experiment.

The new measured value of the $Q(2_1^+)$ in ^{12}C will hopefully be able to critically test theory and confirm the higher values obtained in the experiment presented in this work.

Bibliography

- [AC96] A. Artna-Cohen. Nucl. Data Sheets 79, 1 (1996).
- [Ahr75] J. Ahrens *et al.* Nucl. Phys., A 251 (1975) 479.
- [Ald69] K. Alder and H. K. A. Pauli. Nucl. Phys. A 128 (1969) 193.
- [Ald72] K. Alder, F. Frösel and R. Morf. Nucl. Phys. A 186 (1972) 449.
- [Ald75] K. Alder and A. Winther. *Electromagnetic excitation : theory of Coulomb excitation with heavy ions*. North-Holland, Amsterdam, 2nd edition (1975).
- [Ant09] I. Antcheva *et al.* Comput. Phys. Commun. 180, 12 (2009) 2499.
- [Bag02] C. Baglin *et al.* Nucl. Instrum. Meth. A 481, 1 (2002) 365.
- [Bar01] N. Barnea, W. Leidemann and G. Orlandini. Nucl. Phys. A 693, 3 (2001) 565 .
- [Bar13] B. R. Barrett, P. Navrtil and J. P. Vary. Prog. Part. Nucl. Phys. 69 (2013) 131 .
- [Bea92] C. Beausang *et al.* Nucl. Instrum. Meth. A 313, 1 (1992) 37.
- [Ben03] M. Bender, P.-H. Heenen and P.-G. Reinhard. Rev. Mod. Phys. 75 (2003) 121.
- [Ber09] C. A. Bertulani. *Theory and Applications of Coulomb Excitation* (2009).
- [Bog07] S. K. Bogner, R. J. Furnstahl and R. J. Perry. Phys. Rev. C 75 (2007) 061001.
- [Boh69] A. Bohr and B. Mottelson. *Nuclear Structure*. Benjamin, New York (1969).
- [Bre55] G. Breit and J. P. Lazarus. Phys. Rev. 100 (1955) 942.

- [Bre77] R. Brenn *et al.* Z. Phys. A 281 (1977) 219.
- [Cal16] A. Calci and R. Roth. Phys. Rev. C 94, 1 (2016) 014322.
- [Cas90] R. F. Casten. *Nuclear Structure from a Simple Perspective*. Oxford University Press, New York (1990).
- [Cau02] E. Caurier *et al.* Phys. Rev. C 66 (2002) 024314.
- [Cli69] D. Cline *et al.* Nucl. Phys. A 133, 2 (1969) 445 .
- [Cli86] D. Cline. Annu. Rev. Nucl. Part. S. 36, 1 (1986) 683.
- [Com23] A. H. Compton. Phys. Rev. 21 (1923) 483.
- [Czo83] T. Czosnyka, D. Cline and C. Wu. Bull. Am. Phys. Soc. 28 (1983) 745.
- [D'A20] A. D'Alessio *et al.* Phys. Rev. C 102 (2020) 011302.
- [Die88] S. S. Dietrich and B. L. Berman. Atom. Data Nucl. Data 38, 2 (1988) 199 .
- [Duc99] G. Duchne *et al.* Nucl. Instrum. Meth. A 432, 1 (1999) 90.
- [Ent03] D. R. Entem and R. Machleidt. Phys. Rev. C 68 (2003) 041001.
- [Epe04] E. Epelbaum, W. Glöckle and U. Meißner. Eur. Phys. J. A 19 (2004) 401412.
- [Epe09] E. Epelbaum, H.-W. Hammer and U.-G. Meißner. Rev. Mod. Phys. 81 (2009) 1773.
- [Epe12] E. Epelbaum *et al.* Phys. Rev. Lett. 109 (2012) 252501.
- [Few78] M. Fewell. *Reorientation-effect measurements on ^{18}O , ^{24}Mg and ^{198}Hg* . Ph.D. thesis, Australian National University (1978).
- [For13] C. Forssén, R. Roth and P. Navrátil. J. Phys. G: Nucl. Part. Phys. 40, 5 (2013) 055105.
- [Fri89] S. Fricke *et al.* Nucl. Phys. A 500, 2 (1989) 399 .
- [Fri93] J. Friar *et al.* Phys. Lett. B 311, 1 (1993) 4 .
- [Gas02] L. R. Gasques *et al.* Phys. Rev. C 65 (2002) 044314.
- [Geb17] E. Gebrerufael *et al.* Phys. Rev. Lett. 118 (2017) 152503.
- [Gui78] M. W. Guidry *et al.* Phys. Rev. Lett. 40 (1978) 1016.

BIBLIOGRAPHY

- [Hax49] O. Haxel, J. H. D. Jensen and H. E. Suess. Phys. Rev. 75 (1949) 1766.
- [Hei01] P. Heikkinen and E. Liukkonen, editors. *Cyclotron development program at Jyväskylä*, volume 600. AIP Conference Proceedings (2001).
- [Her16a] H. Hergert. Phys. Scr. 92, 2 (2016) 023002.
- [Her16b] H. Hergert *et al.* Phys. Rep. 621 (2016) 165 . Memorial Volume in Honor of Gerald E. Brown.
- [Hut19] T. Huther *et al.* Family of Chiral Two- plus Three-Nucleon Interactions for Accurate Nuclear Structure Studies (2019).
- [Kam01] H. Kamada *et al.* Phys. Rev. C 64 (2001) 044001.
- [Kav89] A. Kavka. *Coulomb excitation: analytical methods and experimental results on even selenium nuclei*. Ph.D. thesis, Uppsala University (1989).
- [Kav95] A. Kavka *et al.* Nucl. Phys. A 593, 2 (1995) 177 .
- [Kel17] J. Kelley, J. Purcell and C. Sheu. Nucl. Phys. A 968 (2017) 71.
- [Kle29] O. Klein and Y. Nishina. Z. Phys. 52 (1929) 853.
- [KN11] N. Kalantar-Nayestanaki *et al.* Rep. Prog. Phys. 75, 1 (2011) 016301.
- [Kno89] G. F. Knoll. *Radiation Detection and Measurement*. Wiley, New York, 2nd edition (1989).
- [Laz01] I. Lazarus *et al.* IEEE Transactions on Nuclear Science 48, 3 (2001) 567.
- [Lea88] G. A. Leander and Y. S. Chen. Phys. Rev. C 37 (1988) 2744.
- [Les72] P. Lesser *et al.* Nucl. Phys. A 190, 3 (1972) 597 .
- [Lev57] J. S. Levinger. Phys. Rev. 107 (1957) 554.
- [Liu89] E. Liukkonen, editor. *The Jyväskylä K130 cyclotron project*. 2th Int. Conf. Cyclotrons and Their Applications, Berlin (West), Germany (1989).
- [Mac78] M. Macfarlane and S. Pieper. *Ptolemy: a program for heavy-ion direct-reaction calculations*. ANL-76-11(Rev1), United States (1978).
- [Mac01] R. Machleidt. Phys. Rev. C 63 (2001) 024001.

- [Mac11] R. Machleidt and D. Entem. *Phys. Rep.* 503, 1 (2011) 1 .
- [Mac19] P. Marević *et al.* *Phys. Rev. C* 99 (2019) 034317.
- [Mar07] M. Martin. *Nucl. Data Sheets* 108, 8 (2007) 1583.
- [Mar14] P. Maris *et al.* *Phys. Rev. C* 90 (2014) 014314.
- [May49] M. G. Mayer. *Phys. Rev.* 75 (1949) 1969.
- [Mig44] A. B. Migdal. *J. Phys.* 8 (1944) 331.
- [Mye74] W. Myers and W. Swiatecki. *Ann. Phys.* 84, 1 (1974) 186 .
- [Nav02] P. Navrátil and W. E. Ormand. *Phys. Rev. Lett.* 88 (2002) 152502.
- [Nav16] P. Navrátil *et al.* *Phys. Scr.* 91, 5 (2016) 053002.
- [Nog97] A. Nogga *et al.* *Phys. Lett. B* 409, 1 (1997) 19 .
- [Nol94] P. J. Nolan *et al.* *Annu. Rev. Nucl. Part. S.* 44, 1 (1994) 561.
- [Orc15] J. N. Orce. *Phys. Rev. C* 91 (2015) 064602.
- [Orc20] J. N. Orce. *Int. J. Mod. Phys. E* 29, 03 (2020) 2030002.
- [Pak05] J. Pakarinen. *Probing non-grast structures of ^{186}Pb in RDT measurement employing the JUROGAM array.* Ph.D. thesis, University of Jyväskylä (2005).
- [Pak20] J. Pakarinen *et al.* *Eur. Phys. J. A* 56 (2020).
- [Pet20] M. Petri, I.-Y. Lee *et al.* Letter of Intent for ANL (2020).
- [Pie02] S. C. Pieper, K. Varga and R. B. Wiringa. *Phys. Rev. C* 66 (2002) 044310.
- [Pri16] B. Pritychenko *et al.* *Atom. Data Nucl. Data* 107 (2016) 1 .
- [Pri17] B. Pritychenko, M. Birch and B. Singh. *Nucl. Phys. A* 962 (2017) 73 .
- [Rab95] S. Rab. *Nucl. Data Sheets* 75, 491 (1995).
- [Rah08] P. Rahkila. *Nucl. Instrum. Meth. A* 595, 3 (2008) 637.
- [Raj18] M. K. Raju *et al.* *Phys. Lett. B* 777 (2018) 250.
- [Rob93] B. Robson *et al.* *Nucl. Phys. A* 554, 2 (1993) 322 .
- [Rot09] R. Roth. *Phys. Rev. C* 79 (2009) 064324.

BIBLIOGRAPHY

- [San01] S. Santra *et al.* Phys. Rev. C 64 (2001) 024602.
- [Sic13] M. Siciliano. *Shape coexistence in the neutron-deficient nucleus ^{194}Po : Gamma-ray and electron spectroscopic study employing the SAGE spectrometer.* Ph.D. thesis (2013).
- [Spe81] R. Spear. Phys. Rep. 73, 5 (1981) 369 .
- [Spe83] R. Spear *et al.* Phys. Lett. B 128, 1 (1983) 29 .
- [Spe89] R. Spear. Atom. Data Nucl. Data 42, 1 (1989) 55 .
- [Tho88] I. J. Thompson. Computer Physics Reports 7, 4 (1988) 167 .
- [Tsu11] K. Tsukiyama, S. K. Bogner and A. Schwenk. Phys. Rev. Lett. 106 (2011) 222502.
- [Ver83] W. Vermeer *et al.* Phys. Lett. B 122, 1 (1983) 23.
- [Ver84a] W. Vermeer. *Coulomb excitation of the Nuclei ^7Li , ^{10}B , ^{17}O , ^{32}S , ^{12}C and ^{208}Pb .* Ph.D. thesis, Australian National University (1984).
- [Ver84b] W. Vermeer *et al.* Aust. J. Phys. 37, 2 (1984) 123 .
- [Wei35] C. F. v. Weizsäcker. Zeitschrift für Physik 96 (1935) 431.
- [Wil80] W. Wilcke *et al.* Atom. Data Nucl. Data 25, 5 (1980) 389 .
- [Win66] A. Winther and J. de Boer. Perspectives in Physics 91 (1966) 303374.
- [Wir95] R. B. Wiringa, V. G. J. Stoks and R. Schiavilla. Phys. Rev. C 51 (1995) 38.
- [Wol92] H. J. Wollersheim. *Kernstruktur schnell rotierender Atomkerne.* Ph.D. thesis, Goethe University Frankfurt (1992).
- [Woo54] R. D. Woods and D. S. Saxon. Phys. Rev. 95 (1954) 577.
- [Yuk55] H. Yukawa. Prog. Theor. Phys. 1 (1955) 1.
- [Zie10] J. F. Ziegler, M. D. Ziegler and J. P. Biersack. Nucl. Instrum. Meth. B 268, 11-12 (2010) 1818.
- [Zie16] M. Zieliska *et al.* Eur. Phys. J. A 52, 99 (2016).